

**Magnetic Resonance Imaging Approaches to Gel
Dosimetry for Validation of Conformal Radiotherapy
Treatment Plans**

by

Kenneth Nkongchu

M.Sc. (Carleton University) 2001

A thesis submitted to the
Faculty of Graduate Studies and Research
in partial fulfillment of the requirements
for the degree of
DOCTOR OF PHILOSOPHY

(Physics)

Ottawa-Carleton Institute for Physics

Department of Physics

Carleton University

August 2, 2006

© 2006, Kenneth Nkongchu



Library and
Archives Canada

Bibliothèque et
Archives Canada

Published Heritage
Branch

Direction du
Patrimoine de l'édition

395 Wellington Street
Ottawa ON K1A 0N4
Canada

395, rue Wellington
Ottawa ON K1A 0N4
Canada

Your file *Votre référence*
ISBN: 978-0-494-23298-9
Our file *Notre référence*
ISBN: 978-0-494-23298-9

NOTICE:

The author has granted a non-exclusive license allowing Library and Archives Canada to reproduce, publish, archive, preserve, conserve, communicate to the public by telecommunication or on the Internet, loan, distribute and sell theses worldwide, for commercial or non-commercial purposes, in microform, paper, electronic and/or any other formats.

The author retains copyright ownership and moral rights in this thesis. Neither the thesis nor substantial extracts from it may be printed or otherwise reproduced without the author's permission.

AVIS:

L'auteur a accordé une licence non exclusive permettant à la Bibliothèque et Archives Canada de reproduire, publier, archiver, sauvegarder, conserver, transmettre au public par télécommunication ou par l'Internet, prêter, distribuer et vendre des thèses partout dans le monde, à des fins commerciales ou autres, sur support microforme, papier, électronique et/ou autres formats.

L'auteur conserve la propriété du droit d'auteur et des droits moraux qui protègent cette thèse. Ni la thèse ni des extraits substantiels de celle-ci ne doivent être imprimés ou autrement reproduits sans son autorisation.

In compliance with the Canadian Privacy Act some supporting forms may have been removed from this thesis.

Conformément à la loi canadienne sur la protection de la vie privée, quelques formulaires secondaires ont été enlevés de cette thèse.

While these forms may be included in the document page count, their removal does not represent any loss of content from the thesis.

Bien que ces formulaires aient inclus dans la pagination, il n'y aura aucun contenu manquant.


Canada

Abstract

Gel dosimeters are suitable for the purpose of 3-D dose verification using imaging methods such as magnetic resonance (MR) imaging, which can provide a spatial resolution of ~1 mm or better. The two main kinds of gels investigated to date (Fricke and polymer-based gel dosimeters) face various problems which have impeded their full clinical use. The Fricke-based gel dosimeters suffer the problem of spatial information loss with time due to diffusion of radiation-induced ferric ions. Polymer-based gels are quite toxic (carcinogens, teratogens etc) and can't be prepared in normoxic conditions. Possible solutions to these problems are the use of fast imaging methods to limit diffusion for Fricke gels and development of less or non toxic gels for the case of polymer gels.

In this thesis, the ability of the MR imaging Look-Locker method to act as a dose verification tool for Fricke gel dosimeters due to its speed is studied. This is done through the modification of the conventional Look-Locker method to accommodate larger tip angles thereby improving on its precision and accuracy. The optimum method of acquiring the image data in Fourier or k-space so as to limit the effect of image blurring due to a time point spread function inherent of this imaging method is proposed.

Also studied is the prospect of using two new polymer-based gel dosimeters with reduced toxicity as a dose verification tool. This is demonstrated by verifying a treatment planned dose distribution using these gel dosimeters and MR imaging. A multiple spin-echo MR imaging sequence is used as the imaging tool, with possible problems which can affect the accuracy of the measured dose distribution such as B_1 field inhomogeneity and geometrical distortions due to non-linear gradient magnetic fields mapped out and corrected for.

Acknowledgements

I would like to thank my supervisor Dr. Giles Santyr for his advice, guidance and encouragement during the past 5 years and for not letting me give in to my poor health at the beginning of this program. I would also like to thank Dr. John Schreiner for his invaluable assistance, advice and providing me with the materials needed to complete this work through the Kingston Regional Cancer Centre (KRCC), Ontario.

I would also like to acknowledge the support of the KRCC Medical Physics group (Paul De Jean, Myron Rogers, Chris Peters, Rob Senden) especially my friend Paul De Jean for the gel preparations and provision of the optically scanned gel data. Thanks to my cousin Zishu Ndongko, for doing some of the analysis on the generation of gradient non-linearity maps.

It was a great pleasure working with all the members of the Carleton Magnetic Resonance Facility: Albert Cross, Julia Wallace, Greg Cron, Mihai Gherase, Steve White, Nishard Abdeen, Claire Footit, Juan Parra Robles. Special mention goes to Albert Cross who gave me my preliminary experience on sequence programming and Steve White for providing me a place to stay during my trips to Kingston.

I particularly want to thank my family for their unconditional support and for not letting me give in to my poor health at the start of the program. I will also like to acknowledge my uncle, Rev. Fr. Charles Leke, for all his support, especially for providing me with the text books I needed to write up this work. Special thanks go to all my friends in Ottawa, Amanda Cherpak, Dave Waller, Mihai Gherase (my roommate for 4 years), Mike Donkers, Sorina Truica, Jose Martinez, Khalil Boudjemline and J.P. Archambault for providing a conducive environment both at work and away from work.

Table of Contents

| | |
|-------------------------------------------------------------------------------|------|
| Abstract | ii |
| Acknowledgements | iii |
| Table of Contents | iv |
| List of Tables | ix |
| List of Figures | x |
| List of Abbreviations | xiii |
| | |
| 1. Introduction | 1 |
| 1.1 Motivations for Gel Dosimetry | 1 |
| 1.2 Gel Dosimeter Requirements | 3 |
| 1.3 Development of Gel Dosimeter | 7 |
| 1.4 MR Imaging of Gel Dosimeters | 11 |
| 1.5 Importance of Concept of Accuracy and Precision in Gel Dosimetry | 13 |
| 1.6 Disadvantages of Polymer Gel Dosimetry | 14 |
| 1.7 Applications of Polymer Gel Dosimeters | 17 |
| 1.8 Thesis Overview | 21 |
| | |
| 2. Physics of MR Imaging For Gel Dosimetry | 23 |
| 2.1 Introduction | 23 |

| | | |
|-----------|----------------------------------------------------------------------------------|-----------|
| 2.2 | Basic NMR Physics. | 24 |
| 2.2.1 | Excitation and Relaxation in a Magnetic Field. | 26 |
| 2.2.2 | MR Signal Detection | 29 |
| 2.3 | MR Encoding or Imaging Process | 30 |
| 2.3.1 | Selective Excitation | 33 |
| 2.3.2 | Frequency Encoding | 33 |
| 2.3.3 | Phase Encoding | 34 |
| 2.4 | Basic MR Imaging Pulse Sequences | 35 |
| 2.4.1 | Gradient Echo Sequence | 35 |
| 2.4.2 | Spin Echo Sequence | 38 |
| 2.4.3 | Inversion Recovery Sequence | 40 |
| 2.5 | Polymer Gel Dosimetry | 42 |
| 2.5.1 | Transverse and Longitudinal Relaxations | 42 |
| 2.5.2 | Chemical Mechanisms of Polymer Gel dosimeters | 45 |
| 2.5.3 | NMR Response of Polymer Gel Dosimeters | 47 |
| 3. | 3D Look-Locker Imaging for T_1 Parameter Estimation. | 49 |
| 3.1 | Introduction. | 49 |
| 3.2 | Theory. | 50 |
| 3.3 | Methods. | 55 |
| 3.4 | Results and Discussion. | 56 |
| 3.5 | Conclusions. | 64 |

| | | |
|-----------|-------------------------------------------------------------------------------------------|-----|
| 4. | 3-D Look-Locker Imaging for T_1 Gel Dosimetry: Effect of k-space | |
| | Data Acquisition | 66 |
| 4.1 | Introduction | 66 |
| 4.2 | Theory | 67 |
| 4.3 | Method and Simulation | 70 |
| 4.4 | Results and Discussion | 77 |
| 4.5 | Conclusion | 93 |
| | | |
| 5. | T_2 Imaging and B_1-field Inhomogeneity Correction | 94 |
| 5.1 | Introduction | 94 |
| 5.2 | Theory and Method | 96 |
| 5.2.1 | B_1 -field Mapping | 96 |
| 5.2.2 | Multiple Spin Echo Imaging Schemes | 100 |
| 5.2.3 | Correction of Effects of B_1 -z and B_1 -xy Inhomogeneities .. | 103 |
| 5.3 | Results and Discussion | 104 |
| 5.4 | Conclusion | 111 |
| | | |
| 6. | Non-Linear Gradient Field Mapping and Correction | 112 |
| 6.1 | Introduction | 112 |
| 6.2 | Theory and Method | 114 |
| 6.2.1 | Theory | 114 |
| 6.2.2 | Method | 116 |
| 6.2.2.1 | Mapping of Spatial Distortions | 116 |

| | | |
|----------|------------------------------------------------------------------------------------------------------------------|------------|
| 6.2.2.2 | Correction of Spatial Distortions | 119 |
| 6.2.2.3 | Estimation of Change in Gradient Fields | 120 |
| 6.3 | Results and Discussion | 121 |
| 6.4 | Conclusion | 126 |
| 7 | Dose Verification Using Two New Polymer Gel Dosimeters With Reduced Toxicity and MR Imaging | 128 |
| 7.1 | Introduction | 128 |
| 7.2 | Methods and Materials | 129 |
| 7.2.1 | Gel Preparation | 129 |
| 7.2.2 | Treatment Planning and Irradiation | 130 |
| 7.2.3 | MR imaging and Optical CT Scanning | 131 |
| 7.2.4 | Data Analysis | 132 |
| 7.3 | Results and Discussion | 135 |
| 7.4 | Conclusion | 143 |
| 8 | Summary and Future Work | 145 |
| 8.1 | Summary | 145 |
| 8.1.1 | 3-D Look-Locker Imaging Method | 147 |
| 8.1.2 | B ₁ Inhomogeneity Field Mapping and Correction | 148 |
| 8.1.3 | Non-Linear Gradient Field Mapping and Correction | 149 |
| 8.1.4 | Dose Verification using Polymer Gels with reduced Toxicity | 150 |

| | |
|--------------------------|-----|
| 8.2 Future Work | 151 |
| References. | 154 |
| Appendix A. | 172 |

List of Tables

| | | |
|------|--------------------------------------------------------------------------------------------------------------------------------------------------------------|----|
| 3.1. | Mean Accuracy of T_1 estimates using different τ_r , β and M values. | 57 |
| 3.2. | Relative SNR values for sequence images acquired at approximately the same “effective” inversion time for $\beta = 5^\circ$ and $\beta = 10^\circ$ | 58 |
| 4.2 | Estimated T_1 values in (ms) from data acquired using k-space trajectories order 1 and order 4 | 89 |

List of Figures

| | | |
|------|--------------------------------------------------------------------------------------------------------------------------------------------------------------------------------------------------------------------------------------------------|----|
| 2.1. | Rotating frame behaviour of magnetization \vec{B}_1 | 26 |
| 2.2. | Magnetic field in the laboratory and rotating frames after B_1 application | 28 |
| 2.3. | Time behaviour of transverse and longitudinal magnetization relaxations | 29 |
| 2.4. | The k -space coverage for a 2D image | 32 |
| 2.5. | A gradient-echo imaging pulse sequence timing diagram. | 37 |
| 2.6. | A spin-echo imaging pulse sequence timing diagram. | 38 |
| 2.7. | Magnetization behaviour during a spin echo pulse sequence. | 39 |
| 2.8. | A simple inversion recovery imaging sequence diagram. | 41 |
| 3.1. | The modified 3-D Look-Locker pulse sequence | 51 |
| 3.2. | Sample data plots showing the magnetization recovery for $\beta = 10^\circ$ with $\tau_r = 10$ ms being driven faster to steady state compared to the case of τ_r $= 120$ ms, where the plot shows a less perturbed recovery. | 58 |
| 3.3 | The effect on T_1 estimation of increasing the number of “effective” TI images | 59 |
| 3.4. | T_1 precision and accuracy as a function of recovery time variable, τ_r | 61 |
| 3.5. | Modified 3-D LL T_1 values versus inversion recovery T_1 values. | 62 |
| 3.6. | Sample conventional versus modified 3-D Look-Locker T_1 maps | 63 |
| 4.1. | Different k -space acquisition trajectory orders for a value of $P = 16$ | 71 |
| 4.2. | Flow chart of simulation scheme used. | 72 |
| 4.3. | Simulated PSFs for different k -space trajectories for two T_1 values. . . . | 78 |

| | | |
|-------|------------------------------------------------------------------------------------------------------------------------------------------|-----|
| 4.4. | Simulated FWTM of the PSF for four different k-space acquisition orders or trajectories with respect to P for two T_1 values. | 79 |
| 4.5. | FWTM of the PSFs as a function of τ for four different k_y -space acquisition orders. | 80 |
| 4.6. | Simulated FWTM of the PSF for $\beta = 5^\circ$ to 20° for different k_y -space trajectories. | 81 |
| 4.7. | Simulated object signal profile (for 2 and 30-pixel object widths) using four different orders of acquiring k-space data. | 82 |
| 4.8. | Signal as a function of T_1 for a 2 and a 30 pixel object. | 84 |
| 4.9. | Image signal as a function of object width using the 4 acquisition orders. | 86 |
| 4.10. | Experimental image profiles in the phase encode direction. | 87 |
| 4.11. | Expected PVA-Fricke hydrogel dosimeter dose resolution for 52, 68 and 95% confidence levels for measurements taken using 3-D LL. | 92 |
| 5.1. | The imaging sequence diagram used to measure transverse B_1 inhomogeneities. | 99 |
| 5.2. | Schematic of the MEMS (CPMG) imaging sequence. | 102 |
| 5.3. | Slice profiles showing longitudinal B_1 (B_1 -z) inhomogeneity. | 104 |
| 5.4. | The longitudinal B_1 -field (B_1 -z) prior to correction and after correction. | 105 |
| 5.5. | Sample B_1 -xy map or image and 1-D (drawn from B_1 -xy image) profile | 106 |
| 5.6. | R_2 versus flip angle calibration curve B_1 -xy inhomogeneity corrections. | 107 |
| 5.7. | A 1-D R_2 profile uncorrected and corrected for B_1 -xy inhomogeneities | 108 |
| 5.8. | Accuracy of the estimated R_2 values as a function of axial position. | 109 |
| 5.9. | Relative performance of the MEMS and the PHAPS imaging sequence. | 110 |

| | | |
|------|------------------------------------------------------------------------------------------------------------------------------------------|-----|
| 6.1. | Coordinate system used non-linear gradient calculations. | 118 |
| 6.2. | Two spin echo images acquired with a positive and a negative read-out. | 119 |
| 6.3. | Magnet's distortion maps, $\Delta x(x,y,z)$ and $\Delta y(x,y,z)$, for $z = -35$ mm. | 122 |
| 6.4. | Distribution of distortion, $\Delta z(x,y,z)$, from coronal image at $y = -25$ mm. | 122 |
| 6.5. | Distorted and corrected transverse images acquired at $z = -35$ mm. | 123 |
| 6.6. | Distorted and corrected transverse images of a cylindrical phantom. | 124 |
| 6.7 | A map of Jacobian values used to correct "distortions" of transverse images acquired at $z = -35$ mm. | 125 |
| 6.8 | Non-linearity maps of the x,y , and z gradients, and B_0 inhomogeneity map at $z = -35$ mm. | 126 |
| 7.1 | Calibration triangle R_2 image for NIPAM monomer dosimeter and corresponding treatment plan used to irradiate the phantom | 135 |
| 7.2 | NIPAM monomer gel dosimeter R_2 vs dose calibration curve. | 136 |
| 7.3. | MRI dose map of NIPAM monomer gel dosimeter. | 138 |
| 7.4. | γ -index maps from MR vs TPS, and MR vs optical CT dose maps (500 cGy maximum) for NIPAM gel dosimeter | 139 |
| 7.5. | γ -index maps from MR vs TPS, and MR vs optical CT dose maps (200 cGy maximum) for DAAM gel dosimeter | 140 |
| 7.6. | γ -index maps from MR vs TPS, and MR vs optical CT dose maps (500 cGy maximum) for DAAM gel dosimeter | 141 |
| 7.7. | γ -index maps from MRI vs TPS, and MRI vs optical CT dose maps (200 cGy maximum) for DAAM gel dosimeter | 142 |

List of Abbreviations

| | |
|---------------|-----------------------------------------------------------------|
| 3-D (2-D,1-D) | Three (Two, One) Dimensional |
| BPP | Bloembergen-Purcell-Pound |
| CP | Carr-Purcell |
| CPMG | Carr-Purcell-Meiboom-Gill |
| CT | Computed Tomography |
| DAQ | Data Acquisition |
| DAAM | Diacetone acrylamide |
| DTA | Distance-To-Agreement |
| EMF | Electromotive Force |
| FID | Free Induction Decay |
| FOV | Field -of-View |
| FWHM | Full-Width-At-Half-Maximum |
| FWTM | Full-Width-At-Tenth-Maximum |
| FT | Fourier Transform |
| GE | Gradient Echo |
| ICRU | International Commission of Radiation Units and Measurements |
| IMAT | Intensity Modulated Arc Therapy |
| IMRT | Intensity Modulated Radiation Therapy |
| IR | Inversion Recovery |

| | |
|-------|--------------------------------------------------------------|
| KRCC | Kingston Regional Cancer Centre |
| LL | Look-Locker |
| MAA | Methacrylic Acid |
| MAG | Methacrylic Acid Gel dosimeter |
| MAGIC | Methacrylic and Ascorbic Acid in Gelatin Initiated by Copper |
| MEMS | Multi-Echo Multi-Slice Spin-Echo |
| MR | Magnetic Resonance |
| MR | Magnetic Resonance |
| MTF | Modulation Transfer Function |
| NIPAM | N-isopropylacrylamide |
| NMR | Nuclear Magnetic Resonance |
| PAG | Polyacrylamide Gel |
| PHAPS | Phase Alternating Phase Shift |
| PSF | Point Spread Function |
| PVA | Polyvinyl-Alcohol |
| ROI | Region of Interest |
| RF | Radiofrequency |
| SE | Spin-Echo |
| SNR | Signal-to-noise Ratio |
| STE | Stimulated Echo |
| TA | Acquisition Time |
| TE | Echo Time |
| THPC | Tetrakis (Hydroxymethyl) Phosphonium Chloride |

| | |
|-------|----------------------------------|
| TI | Inversion Time |
| TLD | Thermoluminescent Diode |
| TPS | Treatment Planning System |
| TR | Repetition Time |
| VIPAR | <i>N</i> -VinylPyrollidone-Argon |

Chapter 1

Introduction

1.1 Motivation for Gel Dosimetry

The primary objective in radiotherapy is to deliver a prescribed dose of radiation to the tumour as precisely as possible while minimizing the dose to the surrounding healthy tissues. Conformal radiotherapy, a technique for delivery of radiation dose in which the high dose regions of the dose distribution corresponds closely to the tumour volume was developed with this idea in mind. In external beam therapy (a method for delivering a beam of high energy x-rays generated outside the patient to the location of the patients tumours), imaging and computational advances have enabled the development of powerful three-dimensional (3-D) treatment planning software systems with visualization capabilities to enable beam management. This dose conformation is achieved in external beam therapy by the precise management of the radiation beams and their geometry during treatment. In brachytherapy (radiation therapy with the radioactive materials placed in direct contact with the tumours), conformation is achieved by using remote afterloaders which provide complex dose distributions by using variable source position and dwell times.

The clinical implementation of external beam conformal therapy has been limited by difficulties in verifying both the complex dose distributions calculated by the treatment planning system, and the movements of the machines as in intensity modulated radiation

therapy (IMRT) [1]. The International commission of Radiation Units and Measurements (ICRU) [2] recommends a 5% accuracy in delivery of dose for successful conformal radiotherapy. To ensure this accuracy, there is a need for 3-D dosimeters for dose verification with high accuracy.

The verification of dose distributions in conformal therapy is complicated principally by two aspects [3]. Firstly, high dose spatial gradients arise in the target volume in an attempt to conform the dose distribution to the tumour (which is inherently 3-D). Secondly, the treatment modes used are typically dynamic with the movement of the radiation source or patient or both. Thus the total dose at a given location is the integration of the dose contributions over time. Therefore, for dosimetric techniques to be practical, they must be able to integrate the dose distributions over time and have the ability to measure the 3-D distribution with good spatial resolution. Acquisition of dose in a 3-D volume during a dynamic set up is difficult using traditional dosimetric techniques (for example ion chambers) since it is difficult to conform these dosimeters to the volume of interest. Intensive labour is required for 3-D dosimetry using traditional methods such as ion chambers and thermoluminescent dosimeters (TLDs) even when the dose distributions have to be monitored at a few points using simple beam arrangements [4]. Gel dosimeters come closest to fulfilling these requirements (dose integration, 3-D dose acquisition etc), since they can be moulded to desired 3-D shapes and the eventual spatial dose distribution after irradiation can be probed by imaging methods such as magnetic resonance (MR) imaging and computed tomography (CT) – optical or x-ray.

A gel dosimeter is a 3-D matrix mostly made up of cross-linked polymer molecules into which are incorporated chemical substances which are sensitive to radiation.

Currently, the most popular dosimeters are: (i) the Fricke-based [5] gel dosimeters with either agarose, gelatin, sephadex or polyvinyl alcohol (PVA) as the matrix and ferrous ammonium sulphate as the radiation sensitive chemical; (ii) polymer-based gel dosimeters, the most popular of which is the polyacrylamide-gelatin (PAG) with gelatin as the matrix and acrylamide and bisacrylamide as the radiation sensitive chemicals. For these gel dosimeters to be accepted as a clinical dose verification tool there are several requirements that need to be fulfilled (given below) and most of the proposed gels do fulfill many of these.

1.2 Gel Dosimeter Requirements

The main requirements or desired properties for a 3-D dosimeter which happen to correspond to some advantages of gel dosimeters compared with conventional dosimeters are (i) radiation tissue equivalence, (ii) dose integration, (iii) tissue inhomogeneities introduction and (iv) dose rate independence [6,7].

1.2.1 Radiation Tissue Equivalence

A tissue-equivalent material is either a liquid or solid with absorbing and scattering properties for a given radiation closely simulating those of a given biological material such as fat, bone or muscle [8]. For muscle or tissue, water is usually the best tissue equivalent material and since a hydrogel is mostly water it should, therefore, be tissue equivalent. The tissue (or water) equivalence of dosimeters can be verified using different methods which use the mass and electron density, mass absorption coefficient μ_{en}/ρ and the mass stopping power L/ρ calculated at various energies making use of the sum of

elemental values of u_{en}/ρ and L/ρ for different materials weighted by the atomic weight fractions. These values are then compared to the corresponding values of water. Tissue equivalence can also be measured in terms of Hounsfield units or CT numbers which compare the linear attenuation of x -rays through the material to that through water and Monte Carlo simulation to calculate the photon and electron dose distributions in the phantom. A problem faced by dosimetric techniques such as film (radiography), diode detectors and TLDs is their high effective atomic numbers compared to tissue. This may cause a high dose response (or sensitivity) at low photon energies due to the Z -dependence of the photoelectric effect. Also the response of the film may vary with photon energy [9], requiring further corrections if the photon spectrum changes in the phantom. Most of the gel dosimeters currently in use are highly tissue equivalent [10-16].

1.2.2 Dose integration

To obtain dose conformation to a tumour, complex dose distributions are usually obtained using dynamic treatment schemes with dose delivery done over the treatment time. Therefore, measurement requires that the dose be integrated over this period by a dosimeter. Gel dosimeters have an advantage over conventional methods such as ion chambers or TLDs in that these conventional methods cannot be used to probe the 3-D distribution effectively during radiation treatment verification while simultaneously performing the dose integration.

1.2.3 Tissue inhomogeneities

Gel dosimeters can easily be used in the design of anthropomorphic phantoms by inserting materials which mimick the variations in absorbed dose arising due to body shape and tissue inhomogeneities. Of particular interest is the possibility of introducing inhomogeneities such as bones and air spaces (lungs) having density and effective atomic number different from soft tissue into the gel dosimeter. In clinics, the applications of standard isodose charts and depth dose tables assume homogeneous unit density media, whereas in a patient the beam may traverse layers of fat, bone, muscle, lung and tissue. The presence of these inhomogeneities will distort the dose distribution, depending on the amount and type of material present as well as the quality of radiation [17,18]. Thus the effect of these inhomogeneities can be measured using gel dosimeters.

1.2.4 Spatial Resolution in 3-D

To measure high dose spatial gradients associated with conformal therapy, the ability to measure the dose distribution with high spatial resolution becomes important. Dosimetric techniques (methods) such as TLDs and ion chambers are limited by their size and also by the difficulty in mapping the radiation distribution in 3-D. Film possessing a very high spatial resolution in 2-D ($\sim 1\mu\text{m}$) is limited by the fact that these films are not tissue equivalent thus cannot be used in large quantities to make 3-D measurements. Gel dosimeters can be used to detect integrated dose in 3-D with high spatial resolution ($\sim 1\text{ mm}$) in all 3 dimensions using imaging modalities such as nuclear magnetic resonance (NMR) or computed tomography-CT (optical or x-ray). The ability to detect and/or evaluate 3-D dose information using imaging modalities such as

magnetic resonance (MR) imaging and CT permits gel dosimeters to act as both phantom and detector, since there is no need to insert probes such as ion chambers to obtain the desired dose information.

1.2.5 Independence of dose rate, energy and radiation direction

Treatment modalities such as IMRT, where the radiation intensity distribution for each beam is controlled, require that the dosimeter response be independent of dose rate. Also, this response has to be independent of the radiation direction since the gantry (and/or patient) might have to be rotated to deliver the radiation dose to the tumour. Dosimeters such as ion chambers can have the problem of changing response with orientation of the dosimeter. Fricke-based gel dosimeters have been demonstrated to have little or no dose-response dependence on the dose rate of the radiation being delivered within certain dose rate ranges [18-25]. Despite this, the dose rate at which gel dosimeters are irradiated may have a significant influence on the dose response. For most of the polymer-based gel dosimeters being currently investigated there is very little dependence on the dose rate of the dose response. Some of these gels have been found to exhibit higher sensitivity (of dose response) to dose rate compared to others, for example the MAG (methacrylic acid gel) gel has a higher sensitivity compared to the PAG gel [21]. Thus, polymer gel dosimeters with too high a dose rate dependence should not be used as reliable 3-D dosimeters.

The property of little or no dependence on the dose energy in polymer gel dosimeters arises from the fact that reaction rates of monomers (single molecules usually organic compounds having the ability to combine with identical or similar molecules in a

process known as polymerization) with water and different radiolytic products may differ since the relative fraction of interaction processes depend on the type of radiation. Most polymer gel dosimeters have been shown to have little or no dependence on the quality (or energy) of radiation (at least for certain dose ranges) [21-24]. For example the dose response of the PAG and MAG gel has been shown to have very little dependence on radiation quality (for two different beam qualities 6 MV and 25 MV) [21].

1.3 Development of Gel Dosimetry

It was recognized in 1984 by Gore *et al* [26] that the changes in a Fricke dosimeter [5] solution could be detected and measured via the NMR relaxation parameters of the solutes present in the solution. This change results from mainly the radiation-induced conversion of ferrous (Fe^{2+}) ions to ferric (Fe^{3+}) ions; two iron ions with different paramagnetic spin states and ionic radii [5]. This is based on the theory of the relaxation of paramagnetic doped solutions developed by *Solomon* (1955) [27] which accurately predicts that the NMR relaxation rates of the water protons in the vicinity of these two species are different. This is in agreement with the explanation of changing magnetic relaxation rates resulting from fluctuating local time-dependent fields (Abragam 1961) [28].

Gore and his group [26] realized that the spin-lattice relaxation rate R_1 ($=1/T_1$) could be used to quantify the relative abundance of these ions in solution using MR imaging since these parameters govern contrast in MR images. Since MR imaging provides a 3-D imaging capability, this indicated a possibility for 3-D dosimetry based on

NMR. This initial proposal culminated in the development and extensive investigation of various gel matrices such as agarose, gelatin, sephadex [18,19,29-34] and polyvinyl alcohol (PVA) [15] into which are incorporated ferrous ions. These gel matrices act to “stabilize” (or spatially localize) the chemical change which takes place upon irradiation. In Fricke gels, the gel matrix is aimed at spatially localizing the radiation-induced conversion of Fe^{2+} ions to Fe^{3+} ions. Unfortunately, Fricke-based gel dosimeters suffer from the problem of auto-oxidation. Another more important concern is the diffusion of radiation-induced ferric ions (Fe^{3+}) from the site of chemical change thereby resulting in the loss of the spatial information. This problem of diffusion limits the time between start of irradiation to imaging of the gel to obtain dose information to a couple of hours (typically 2 hours).

These concerns have motivated the search for new gels with improved qualities. *Maryanski et al* [35,36] introduced a different type of gel called BANG gels [22,23] and later the PAG gels [37-40], which are based on radiation-induced polymerization and cross-linking of acrylic or acrylamide monomers infused in the gel matrix containing ~ 90 % water. The extent of formation of these cross-linked polymers is dose dependent and results in increased NMR relaxation rates particularly spin-spin relaxation rates ($R_2 = 1/T_2$) of neighboring water protons having a higher sensitivity (or dose response) than spin-lattice relaxation rates ($R_1 = 1/T_1$). See Chapter 2 for the definition of the NMR relaxation parameters T_1 and T_2 . Radiation makes the gels more rigid reducing the water motion and therefore the spin-spin relaxation time (T_2). The relative dose distribution for these gels can be obtained by making use of spin-spin relaxation rate $1/T_2$. Diffusion is less of a problem compared to Fricke gels as these gels are able to maintain their spatial

distribution of information for a long time (days). Polymer-based gels can also be analyzed using optical methods with image reconstruction in 2 and 3 dimensions since the radiation effect is visible [38,39,41].

Since the development of the first polymer gel dosimeters (PAG with composition of 3% acrylamide, 3% N,N'-methylene-bis-acrylamide, 6% gelatin and 88% water), many other polymer gel dosimeters with different compositions have been proposed and are currently being investigated as potential 3-D dosimeters [21,25,42-48]. The main variation from the PAG gel has been the replacement of the monomer acrylamide with other monomers such as acrylic acid, methacrylic acid, 1-vinyl-2-pyrrolidone amongst others [21,42]. Some of these gels have favourable properties such as a higher dose response ($0.358 \text{ s}^{-1}\text{Gy}^{-1}$, $0.498 \text{ s}^{-1}\text{Gy}^{-1}$, $1.193 \text{ s}^{-1}\text{Gy}^{-1}$ for acrylic acid, methacrylic acid, 2-hydroxyethyl methacrylate respectively as opposed to $0.331 \text{ s}^{-1}\text{Gy}^{-1}$ for the acrylamide PAG gel [21,42]). Some of these gels exhibit a larger dose range (dynamic and/or linear) to radiation, for example the polymer gel dosimeters with the VIPAR gel dosimeter have a linear range of $\sim 40 \text{ Gy}$ (with a dynamic range of $\sim 250 \text{ Gy}$)[21,25] compared to PAG with an approximate linear dose range of 1-10 Gy. One of the main reasons that has spurred on the development of new gel dosimeters has been the problem of oxygen poisoning (see section on disadvantages of polymer gels) faced by the PAG gel dosimeter which requires the gel to be manufactured under strict hypoxic conditions (usually by bubbling with inert gases such as argon). A new generation of gel dosimeters (normoxic gel dosimeters-permit manufacture under normal atmospheric conditions) [16,45,46,49] contain an anti-oxidant that binds to the oxygen in the gel and consequently prevents free radical scavenging by the oxygen. Despite the advantage of being able to make these gels

under normoxic conditions, there have been reports of post irradiation instabilities (both temporal and spatial) due to long-lived polymer radicals and high acidity content as in the case of MAGIC gel dosimeters [16]. A reduction in the dose response (or sensitivity) when compared to the traditional PAG gel dosimeter [16,49] has also been reported.

A reduction in dose response would mean worsening of the dose resolution (defined as the minimal separation between 2 absorbed doses such that they may be distinguished with a given level of confidence), a concept that has been introduced which allows one to obtain an optimal formulation required for a specific range of absorbed doses. This concept also permits the comparison comparisons between gels of different formulations [50]. This dose resolution concept also takes into consideration the ability of the imaging methodology such as magnetic resonance imaging (MRI), optical or x-ray CT to measure the dose distribution to a desired accuracy and precision with the predominant contribution being the standard uncertainty in the determination of T_1 and T_2 for the case of MR imaging [51]. Clinical radiotherapy requires the dose uncertainty to be within 5%, and with dosimetry being a factor in dose delivery, it is necessary to have an uncertainty significantly less than this [51]. In fact, *Baldock et al* [51] suggested that dosimeters (or gel dosimeters) should have dose resolution values of the order of 2% based on the ICRU (ICRU 1987 [52]) recommendations of computer dose calculations being less than 2 %. *Baldock et al* [51], have investigated the dose resolution for PAG gel dosimeters over the 0 – 10 Gy range and found that the 2% ICRU condition couldn't be met even with the confidence level being relaxed to 52%. There have been reports of new gels with improved dose resolution of ~2.3 % compared to 3.8 % for the PAG dosimeter [43]. This desire to improve the dose resolution as well as the overall quality of 3-D

information gleaned from gel dosimeters has led to a lot of research into MR imaging as a 3-D measurement tool to improve dose resolution.

There have been investigations to eliminate systematic problems in the measurement of T_1 and/or T_2 parameters using clinical MR systems. Some of these factors have been found to affect precision and accuracy and various recommendations on limiting or eliminating these problems have been suggested. These have been factors such as RF (radiofrequency) inhomogeneity, RF heating of gel samples, eddy currents due to constant magnetic gradient fields switching, temperature drift, molecular self-diffusion, chemical shifts, susceptibility differences, slice profile errors, stimulated echoes, optimization of imaging sequence parameters or variables amongst others [46,53-61]. The imaging sequences used to estimate these parameters (either T_1 -weighted spin-echo for the case of Fricke-based gels or T_2 -weighted spin-echo for the case of polymer-based gel dosimeters) haven't changed over time, but most of the investigations have been focused on some of the above mentioned problems which can limit the accuracy of MR imaging as a 3-D gel dosimetry tool. These factors have been shown to lead to dose errors of varying magnitudes, and continues to be an area of intense research despite some drawbacks associated with these polymer gel dosimeters.

1.4 MR Imaging of Gel Dosimeters

MR imaging of polymer gel dosimeters usually requires the calculation of R_2 maps from a set of MR images. These relaxation rates (R_2) are measured by applying radiofrequency (RF) pulses to excite the magnetization of the spin system and form spin-

echoes and then sampling the magnetization during the return to equilibrium. This image acquisition is generally done using two main approaches [22,25,37,62-79]: (i) Spin-echo imaging sequences; and (ii) multiple spin-echo based sequences such as multi-echo multi-slice spin-echo (MEMS), MEMS sequences with phase encoding in the slice selection direction or phase alternating phase shift (PHAPS) pulse sequences as described in Chapters 2 and 5. All these sequences introduce an R_2 dependence in the MR signal. The spin-echo sequence uses a 90° RF pulse to excite the magnetization and a 180° pulse to refocus the spins to generate a signal (spin-echo). The multiple spin-echo method acquires a train of spin echoes generated by the repeated application of the 180° pulse, with each echo corresponding to a different echo time. Using the simple spin-echo sequence for R_2 estimation requires the estimation of R_2 from just a pair of MR images and involves the estimation of two unknown parameters, the proton density ρ and R_2 from a pair of images. This has the effect of producing more noisy and less accurate R_2 maps compared to R_2 maps obtained from images acquired using multiple spin echo (MEMS) based images such as MEMS and PHAPS [80]. Concern about errors in measured R_2 values owing to imperfect refocusing with 180° pulses, due to RF inhomogeneities has led to a preference for single echo sequence methods by some authors [35,36,37,40].

As for gels such as the Fricke gel dosimeters which entail the estimation of the dose maps via the T_1 parameter, most of the image acquisition methods to demonstrate the clinical applications of Fricke gels in the literature [81-84] has been through the employment of the inversion recovery sequences described later in Chapter 2. This sequence uses a 90° or 180° pulse to rotate the magnetization off its equilibrium

orientation followed by either another 90° pulse and a magnetic gradient field to create what is called a gradient echo (GE) signal or a spin echo sequence as described above to generate spin echo signals after a given delay time. Image acquisition using this sequence can be prohibitively long (> 1 hour) due to the dead times required between the generation of each GE signal and the next set of signals needed to acquire the images from which the T_1 parameters can be estimated. Given that Fricke gels face a problem of ferric ions diffusion, there is typically image degradation during the acquisition process itself. Faster image acquisition methods may help to mitigate this problem.

1.5 Importance of Concept of Accuracy and Precision in Gel Dosimetry

To be able to generate dose maps from gel dosimeter images acquired using MR or CT imaging optical or x-ray for example, calibration curves relationships between the gel sensitive parameter (affected by chemical changes due to radiation) and the dose delivered have to be generated. This calibration curve is usually done by irradiating a group of gel-filled sample tubes to known doses and then imaged to provide the curve via the sensitive parameter. These curves are used to convert the gel dosimeter images to dose images to validate the treatment plan dose distribution delivered to the phantom. Since a calibration curve is used to obtain the dose images accuracy of the estimated (imaging) parameter becomes of less importance as opposed to its precision which is of most importance. This is because the precision in obtaining the parameter and the dose sensitivity (or change in parameter brought about by a unit radiation dose) of the gel dosimeter via the imaging parameter determine the dose resolution. This dose resolution

is the quality factor which determines the suitability of the gel dosimeter for dose verification. This factor combines the precision in obtaining the dose-enhanced parameter and the dosimeter radiation dose response to determine the minimal separation between two doses which can be distinguished by a given level of confidence [51].

1.6 Disadvantages of Polymer Gel Dosimeters

Despite the promising ability to evaluate 3-D dose distribution brought by the advent of polymer gel dosimetry, there are some drawbacks or problems associated with polymer gel dosimeters. Some of these problems (given below) described by *McAuley* [85] for PAG gels apply to most other polymer gel dosimeters.

1.6.1 Long-lived radicals

In polymer gel dosimeters, there is the formation of immobile cross-linked polymer (a macromolecule consisting of a larger number of repeated units or monomers) molecules and the reduced mobility of polymer radicals leads to slower termination reactions and higher polymerization rates. Due to the difficulty of trapped polymer radicals to diffuse through the solution to react with other radicals, there is an inhibition in the termination rate of the polymerization reactions. Despite this, propagation continues due to the fact that monomer molecules can diffuse through the gel matrix to encounter radicals. This is because the monomers are much smaller and more mobile than the growing polymer radicals or chains. These polymer radicals will continue to grow until the polymerization stops by [85,86]: (i) the radical reacting with a monomer through

what is called a chain transfer producing a new radical that further initiates propagation; (ii) the polymer radical encountering another radical and terminates; (iii) the radical reacting with a polymerization inhibitor such as gelatin (i.e. gelling agent) or an impurity such as oxygen which then produces another radical with insufficient energy to initiate polymerization; and (iv) the complete consumption of monomers in mixture.

1.6.2 Edge Enhancement

In PAG or polymer gel dosimeters [22,23,35-46], there is diffusion of polymer and monomers from regions of higher concentration to those of low concentration, though polymer molecules diffuse at a lower rate compared to monomers [36,86]. This slower polymer diffusion results from its large size and by entanglement with gelatin which severely inhibits its movement. For PAG, it has been suggested that polymer diffusion is driven by reaction diffusion [86], in which the radical end of the polymer chains moves slowly through reaction with the monomer and co-monomers (a monomer which has co-polymerized with another monomer). Reaction diffusion is much slower than the diffusion of monomers by centre-of-mass diffusion [86]. Due to the diffusion of the monomers from the side of the non-irradiated zone to the boundary between the irradiated and the non-irradiated areas and subsequent reaction of the monomers, co-monomers and radicals, there is an edge enhancement effect in these regions. This edge enhancement seems to increase with time following irradiation and can result in calculated dose errors in these areas. It has been suggested that this problem may be reduced by using larger monomers and cross-linkers that will diffuse less through the

matrix as well as employing the suggestions above to reduce the effect of long-lived radicals [85].

1.6.3 Monomer toxicity

Most of the monomers and/or co-monomers currently being used for polymer gel dosimeters are toxic. For example, the acrylamide used in PAG gel dosimeters and its derivatives are well known to be neurotoxins, teratogens and carcinogens. The acrylamide can be easily absorbed through the skin. This has been one of the main reason why it has not been widely accepted as a regular clinical dose verification tool. Once all the monomers and co-monomers (or cross-linkers) have reacted it becomes safe to handle. Unfortunately, total conversion of the monomers to polymers isn't achieved in the clinical tool, since the areas that haven't been irradiated are expected not to polymerize thereby leaving the monomers un-reacted. Some of the less toxic monomers that has been suggested to replace the extremely toxic acrylamide are *N*-vinylpyrrolidine [25] and *N*-vinyl formamide [85,87]. *N*-vinyl formamide is an isomer of acrylamide which is a liquid at room temperature and is only a suspected teratogen but can also be damaging to the eyes [142].

1.6.4 Oxygen poisoning

Oxygen has an inhibiting effect on the free radical polymerization of most polymer dosimeters such as PAG, VIPAR [25] gels amongst others, and requires that these gels be manufactured under oxygen-free conditions. This has led to the development of normoxic polymer gel dosimeters which can be made under normal atmospheric conditions such as PAGAT [16,44], MAG amongst others. PAGAT is a

PAG gel mixed with the anti-oxidant tetrakis (hydroxymethyl) phosphonium chloride (THPC) which scavenges for oxygen in the gel mixture. Another gel that can be made under normoxic conditions and doesn't employ THPC has been the MAGIC gel which consists of methacrylic acid (MAA), gelatine, hydroquinone, copper sulfate, and ascorbic acid [45]. Although normoxic gels such as PAGAT show a lower dose sensitivity, their performance with respect to factors such as spatial integrity, temperature sensitivity and dose rate dependence can make them more reliable than PAG gels as noted in a comparison between the PAG, PAGAT and the normoxic MAG gel dosimeters by *De Deene et al* [16]. The development of these normoxic polymer gel dosimeters have certainly helped to enhance the possibility of a wide adoption of polymer gel dosimeters as a clinical dose verification tool. Some applications of these polymer gel dosimeters both normoxic and anoxic, have been demonstrated and a brief summary of some of these demonstrated applications are given below.

1.7 Applications of Polymer Gel Dosimeters

There have been reports in the literature of polymer gel dosimetry being used in a number of increasingly complex treatment techniques with a variety of radiation modalities for dose verification. Some of these polymer gel dose verifications have been in dose delivery modalities such as brachytherapy, conformal and IMRT, stereotactic radiosurgery, charged particle beams amongst others as summarized in [88].

1.7.1 Brachytherapy

Brachytherapy is a dose delivery modality capable of delivering very high doses with high dose gradients. It is therefore important to be able to accurately verify brachytherapy treatment planned doses. Polymer gel dosimeters have been used to investigate the dosimetry of clinical radiation sources such as ^{192}Ir and ^{137}Cs with considerable success [22,37,62-65]. Good spatial and dosimetric agreement with treatment plans have been demonstrated using these polymer gel dosimeters. One of the gels recently investigated which seems to show promise for high dose and high dose rate brachytherapy is the VIPAR gel dosimeter [25]. This polymer gel dosimeter has a linear dose response up to ~40 Gy. This large linear dose response ensures it can be used not only for brachytherapy but in most applications in radiotherapy. In polymer gel dosimetry for high dose brachytherapy sources, most of the dose error comes at radial distances close to the source. This isn't the case for the brachytherapy study with VIPAR gels as shown by *Kipouros et al* [25] where they only noticed a dose underestimation by ~20 % for radial distances < 2 mm, if the dose exceeded 300 Gy. The good performance observed for this gel for doses up to 200 Gy (down to 2 mm) is mainly due to its large dynamic range (~250 Gy).

1.7.2 Conformal and intensity-modulated radiotherapy

Due to advances in conformal and IMRT, highly complex field shapes with high dose gradients can be planned and delivered to a target volume while sparing healthy surrounding tissue. The ability of polymer gel dosimeters to verify dose distribution delivered by IMRT or IMAT (intensity modulated arc-therapy treatment) has been

demonstrated and used in some clinics [66-70]. For example in the work by *Vergote et al* [66], polymer gel dosimetry was used to assess an IMAT treatment for whole abdominopelvic radiotherapy. In that study, they found the gel measurement of the dose distribution to comply with the predetermined dose-volume constraints. Dose differences of less than 3% were measured outside the high dose gradients and spatial shifts were within 2.5 mm when the abdominal phantom was irradiated with two rectangular fields.

Conformal irradiation of concave targets in the lower neck region have been verified by *De Deene et al* [67], using multiple, static, intensity modulated beams delivered with a multileaf collimator. They measured mean dose differences of less than 8% between gel and film measurements. Dynamic multileaf collimator treatment delivery verification has also been performed using polymer gel dosimeters [71].

1.7.3 Stereotactic radiosurgery

In stereotactic radiosurgery, the targets are small and the irradiated volume contain regions of steep dose gradients thereby requiring dosimetry be performed with high spatial resolution. Polymer gel dosimetry using MR imaging has been employed as a dose verification tool with some good results. For example, in the work by *Karaiskos et al* [72], using the VIPAR polymer gel and MR imaging to assess the overall accuracy associated with gamma knife (a special multi-source cobalt machine which focuses high energy gamma rays on a small area: used as local therapy for brain lesions) clinical applications, good agreement was obtained between the measured and expected (or calculated) distribution. They found experimental uncertainties of the order of the imaging pixels (<1 mm) and this allowed verification of single shot gamma knife

applications in terms of acceptance specifications for precision in beam alignment and accuracy. They observed significant deviations between the measured and expected results only in low dose regions potentially due to VIPAR gel uncertainties, dose resolution and non-linearity of dose response in low dose regions. There have been other measurements performed using polymer gel dosimetry; from the validation of the placement of simple single targets to the validation of complicated dose distributions [73-77].

1.7.4 Charged Particle Beams

Using PAG gel dosimeters, there have been measurements done on the central axis-depth dose measurements by different authors showing agreement with silicon diode measurements within 3 % [22,78]. A background MR imaging evaluation or subtraction of the relaxation rate (R_2) unirradiated gel phantom was required to obtain reliable results [78]. *Heufelder et al* [79], used BANG polymer gel to verify delivery with 68 MeV in eye tumor therapy. They showed that polymer gel dosimetry can be an effective tool in proton radiotherapy but noticed that LET (linear energy transfer) affected the dose- R_2 linear relationship. They were unable to parametrize this relationship. They also found that depth dose curves in this gel dosimeter revealed a quenching of the Bragg maximum due to LET effects which they believed to be due to saturation of the polymerization yield (observed at 3.1 and 4.1 Gy) and/or recombination in the proton tracks (for lower doses). They postulated that at higher proton energies needed for therapy of deep-seated tumours the quenching effects would play a less dominant role due to the increase of the average LET in the Bragg peak region with increasing range straggling [88].

1.8 Thesis Overview

Over the past few years, there has been a systematic shift of interest in gel dosimetry with MR imaging from Fricke (or T_1 -based) gel dosimeters to polymer (T_2 -based) gel dosimeters. This has been due mostly to the problem of diffusion of ferric ions from their site of formation along with a lack of a reliable and fast T_1 imaging sequence to quickly evaluate the dose distribution in T_1 -based gel dosimeters to reduce these effects. One of the fast T_1 mapping techniques which has been suggested as a possible MR imaging tool for to mitigate diffusion is the two-dimensional (2-D) Look-Locker imaging sequence [100]. However, a direct application of this 2-D Look-Locker sequence as a gel dosimetry tool for 3-D imaging would take at least an hour and a half to acquire $256 \times 257 \times 32$ matrix data. The first part of this thesis is aimed at investigating and improving the Look-Locker imaging sequence as a possible imaging tool for Fricke-based gel dosimeters. The second part is geared towards the investigation of T_2 mapping in polymer gel dosimeters with reduced toxicity which are imaged by MR imaging and compared to calculated and optical CT dose maps as a dose verification tool.

Chapter 1 presented an introduction to this thesis, giving the motivation for gel dosimetry and a historical development of gel dosimetry as a clinical dose verification tool. This chapter also discusses some requirements expected of gel dosimeters, and outline drawbacks faced by polymer gel dosimeters. Chapter 2 briefly presents some basic MRI theory including relevant imaging sequences as well as the basic polymerization mechanisms in irradiated polymer gels.

Chapter 3 describes the proposed 3-D Look-Locker imaging sequence with characteristics such as improved signal-to-noise ratio (SNR), accuracy and reduced imaging time so as to be able limit the effect of diffusion of irradiation-induced ferric ions common with Fricke or T_1 -based gel dosimeters. This is followed in Chapter 4, by an investigation of the optimal method of acquiring the data in what is referred to in MR imaging as “k-space” or Fourier space.

In Chapter 5, inhomogeneities in the RF or B_1 magnetic field which could affect the parameters obtained from the acquired MR images are mapped and corrected for. This is followed in Chapter 6 by the presentation of a method of mapping and correcting the effects of non-linear magnetic field gradients on the acquired images. It is demonstrated that these inhomogeneities, if not corrected can result in significant errors in the dose maps derived from MR images for dose distribution verification in radiotherapy.

Chapter 7 presents a demonstrated application of these polymer gel dosimeters with reduced toxicity. This chapter presents the methods used to convert the MR maps to dose maps and demonstrates the accuracy achieved using these gels and their potential to become an important tool not only for dose verification using MR imaging but also its prospective use in optical gel dosimetry. The last chapter summarizes the results presented and also provides directions for possible future work.

Chapter 2

Physics of MR Imaging for Gel Dosimetry

2.1 Introduction

Ever since the discovery of the nuclear magnetic resonance (NMR) phenomenon by Bloch and Purcell in 1946, the popularity of the NMR technique has increased [89,90]. Following this discovery, NMR has been used to analyze the structure of materials, including the study of molecular dynamics of various molecules. Of relevance to this work are NMR relaxation times that can be used to study protons of water and/or those of other dissolved chemical molecules hydrating the solutes produced by radiation in chemical dosimeters such as polymer gel dosimeters. In this chapter, the basic theory underlying NMR imaging and relaxation, a phenomenon which has been extensively studied, is presented with attention focused on the relaxation time constants and the relaxation mechanisms. These are the mechanisms mainly affected by the changes taking place in gel based dosimeters following irradiation, be they Fricke-based or polymer-based gel dosimeters. In section 2.5, a simplified review of the chemical reactions and NMR response (usually induced by radicals created through radiation action) of polymer gel dosimeters is presented. These principles are necessary to understand the work presented in this thesis.

2.2 Basic NMR Physics

The Magnetic Resonance (MR) imaging signal originates from nuclei with an odd number of protons and/or an odd number of neutrons. Of most interest in MR is the hydrogen nuclei (protons). A proton has a property of intrinsic angular momentum referred to as spin \vec{I} , with an associated magnetic moment $\vec{\mu}$:

$$\vec{\mu} = \gamma \vec{J} \quad (2.1)$$

where $\vec{J} = \hbar \vec{I}$ is the total angular momentum and γ is the gyromagnetic ratio, a known constant unique for each type of nucleus. For protons ($I = 1/2$), $\gamma/2\pi = 42.58$ MHz/Tesla. A proton forms the nucleus of hydrogen atoms; the largest source of signal in conventional NMR and MR imaging. In a material containing a collection of hydrogen atoms (or spins) in abundance (e.g. water), a net magnetization (\vec{M}) results from the ensemble average of the individual dipole moments contained therein when placed in a magnetic field. This magnetization will be zero in the absence of a magnetic field. From the quantum mechanical point of view, the applied static magnetic field, \vec{B}_0 , oriented by convention along the z -axis, causes a splitting of the energy levels between those spins aligned with and against the field (Zeeman splitting). The lower energy state corresponds to an orientation along \vec{B}_0 while the higher state corresponds to an orientation against \vec{B}_0 . Specifying the number in the higher and lower energy state by N_- and N_+ respectively, the energy separation ΔE between the levels is given by:

$$\Delta E = \gamma \hbar B_0 \quad (2.2)$$

where \hbar is Planck's constant (divided by 2π). From (2.2) the photon frequency necessary to cause transitions between these levels is known as the Larmor frequency ω_o , where [91]:

$$\bar{\omega}_o = -\gamma\vec{B}_o \quad (2.3)$$

Although the N_+ population is of lower energy and the tendency is to occupy the minimum energy state, thermal energy is sufficient to exceed the energy separation and cause population of the N_- level. Hence the ratio of the two populations is dependent on the Boltzmann distribution [91]:

$$\frac{N_-}{N_+} = \exp(-\Delta E/kT) \quad (2.4)$$

where k is the Boltzmann's constant and T is the absolute temperature. At room temperature and typical field strength (for example 1 T) the ratio $\Delta E/kT$ ($\sim 10^{-6}$) is a very small number, thus it is possible to make a linear approximation of the Boltzmann exponential and thus obtain the magnetization per unit volume [91]:

$$M_o = \left(\frac{N\gamma^2\hbar^2}{4kT} \right) B_o \quad (2.5)$$

where N is the number of nuclear spins per unit volume. Thus the equilibrium magnetization is $M_z = M_o$ and $M_{xy}=0$, where M_z , is the longitudinal magnetization (in direction of the B_o field) and M_{xy} , is the transverse magnetization

2.2.1 Excitation and Relaxation in a Magnetic Field

In a typical MR experiment, the equilibrium magnetization oriented along \vec{B}_0 is perturbed through a resonant radio-frequency (RF) pulse at a frequency ω or near the Larmor frequency, ω_0 . Resonant energy absorption by the spin system occurs with the angular frequency ω_0 and the net magnetization \vec{M} becomes time dependent such that $M_z \neq M_0$ and $M_{xy} \neq 0$. After excitation, the magnetization tends to relax back to its equilibrium state (with $\vec{M} = M_0$).

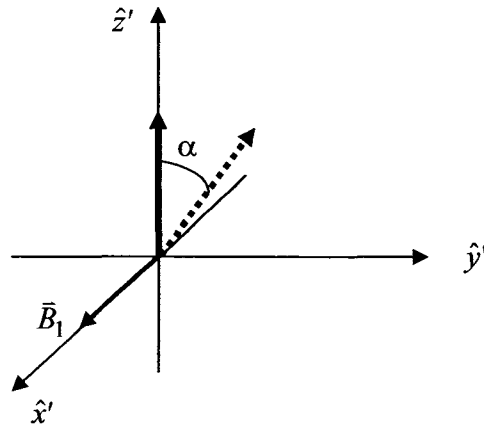


Fig. 2.1: Rotating frame behaviour of magnetization showing rotation towards the transverse plane induced by \vec{B}_1 .

The excitation and relaxation are described by the phenomenological Bloch equations [92] which describe the motion of \vec{M} in a frame (Fig. 2.1) rotating with angular velocity ω with respect to the laboratory frame:

$$\frac{dM_{xy}}{dt} = \gamma (\vec{M} \times \vec{B}_{eff})_{xy} - \frac{M_{xy}}{T_2} \quad (2.6)$$

$$\frac{dM_z}{dt} = \gamma(\vec{M} \times \vec{B}_{eff})_z + \frac{M_0 - M_z}{T_1} \quad (2.7)$$

where T_1 and T_2 are the relaxation time constants which characterize the recovery of the magnetization along the \vec{B}_0 field and its decay perpendicular to the \vec{B}_0 field respectively. In this rotating frame representation, the magnetic field experienced during MR experiments includes both a static (B_0) term as well as an RF term, B_1 provided by an RF coil and can be expressed as:

$$\vec{B} = B_1 \cos(\omega t)i - B_1 \sin(\omega t)j + B_0 k \quad (2.8)$$

where B_1 denotes the magnitude of the magnetic field associated with the RF pulse, conventionally directed along the x-axis and ω is the carrier or rotational frequency of the RF pulse. The magnetization in this rotating frame precesses about an effective field given by [89]:

$$\begin{aligned} \vec{B}_{eff} &= \vec{B} - \frac{\vec{\omega}}{\gamma} \\ &= B_1 i + B' k \end{aligned} \quad (2.9)$$

where $\vec{\omega}$ is the frequency of the rotating frame about the laboratory frame (Fig 2.2), $B' = B_0 - \omega/\gamma$, giving a resonance offset, $\Delta\omega = \gamma B'$ of the RF pulse. For the case where $\omega = \omega_0$ (i.e. on resonance) the last term in Eqn. 2.9 is zero, the magnetization only experiences the effect of the RF terms (i.e. B_1) resulting in the nutation or tipping of \vec{M} away from its equilibrium position. The amount of tipping depends on both the magnitude of the RF pulse B_1 and the RF pulse length or duration t_p such that the angular

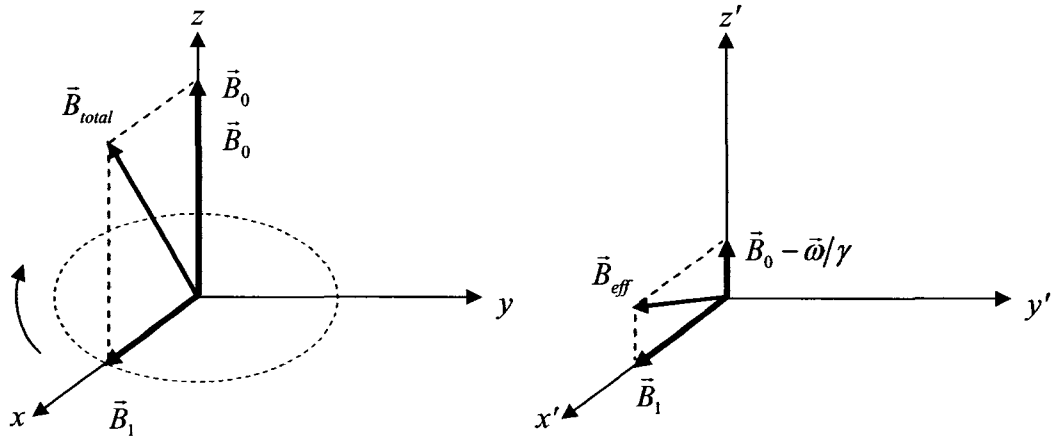


Fig. 2.2. Rotating magnetic field in the (a) laboratory and (b) rotating frames for B_1 field applied along the x -axis.

increment by which \vec{M} is nutated, α is given by:

$$\alpha = \gamma \int_0^{t_p} B_1(t) dt \quad (2.10)$$

Thus, B_1 and/or t_p can be set such that \vec{M} is rotated, for example, completely into the transverse plane (90° pulse) or completely rotated along the negative \hat{z}' axis (180° pulse). Upon removal the RF energy ($B_{\text{eff}} = 0$), the left-most terms of Eqns 2.6 and 2.7 disappear such that only the relaxation terms remain. Solution of these differential equations results in the magnetization relaxing according to:

$$M_{xy} = M_{xy}(0) \exp(-t/T_2) \quad (2.11)$$

$$M_z = M_0(1 - \exp(-t/T_1)) + M_z(0) \exp(-t/T_1) \quad (2.12)$$

The decay and growth of these magnetization terms are illustrated in Fig. 2.3.

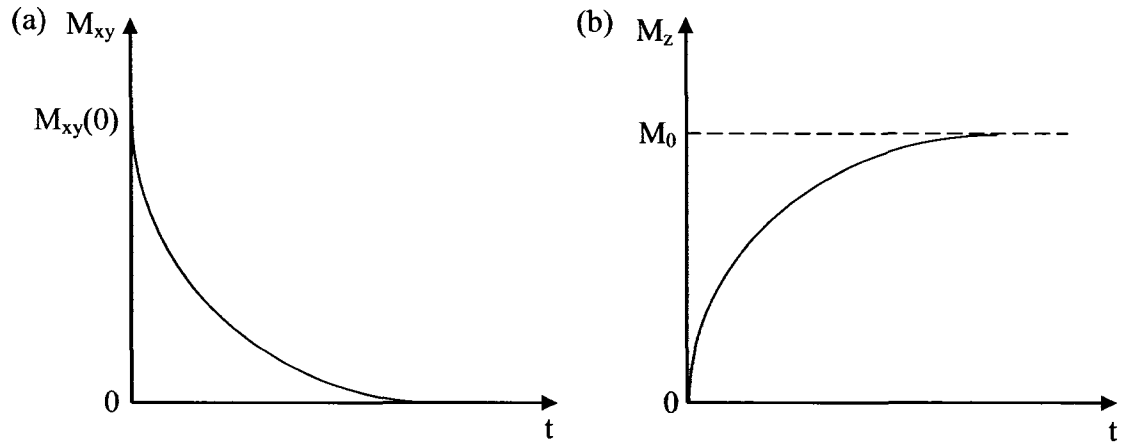


Fig. 2.3. The behaviour of (a) transverse and (b) longitudinal magnetization relaxations as a function of time, t .

2.2.2 MR Signal Detection

MR signal detection is based on the Faraday law of electromagnetic induction. This law states that the time varying magnetic flux through a conducting loop (a receiver coil) will induce an electromotive force (or voltage) in the loop equal to the rate at which the magnetic flux through the coil is changing. Thus, the rotating transverse magnetization M_{xy} induces an electromotive force (EMF) in the RF coil oriented to detect changes of magnetization in the xy plane. The detection sensitivity of the receiver coil is determined through the principle of reciprocity, the sensitivity of the coil is equal to the transverse field produced by a unit current in the coil, $B_{1,xy}$, and the induced voltage can be expressed using Faraday's law of magnetic induction as [91]:

$$V(t) = -\frac{\partial \Phi(t)}{\partial t} = -\frac{\partial}{\partial t} \int_{V_S} B_{1,xy}(\vec{r}) M_{xy}(\vec{r}, t) d^3\vec{r} \quad (2.13)$$

where the integral is calculated over the volume of the sample V_s and $\Phi(t)$ is the magnetic flux crossing the coil at time t . The detected signal, that decays exponentially, is called a Free Induction Decay (FID) and can be written as [93]:

$$S(t) = A \int_{V_s} B_{xy}(\vec{r}) M_{xy}(\vec{r}) e^{-i\Delta\omega t} d^3\vec{r} \quad (2.14)$$

where A is a proportionality constant containing the main field B_0 and RF field B_1 and resonance offset, $\Delta\omega = \omega(\vec{r}) - \omega_0 = \gamma \Delta B_0(\vec{r})$. The field inhomogeneity is both a function of space and time and is due to various sources, including imperfections in the magnet's field and magnetic susceptibility differences inside the sample, as well as any applied magnetic field gradients for spatial encoding as described in the next section. Note that in Eqn 2.14, relaxation effects have been ignored for simplicity. The same RF coil that nutates or excites the magnetization is used to detect the resulting MR signal.

2.3 MR Encoding or Imaging Process

To be able to obtain an MR image from the detected signal, physical hardware is needed to encode the spatial information and a mathematical tool is needed to decode the measured signal. This encoding of spatial information is done through the application of slice selecting, frequency encoding, and phase encoding magnetic field gradients (typically 1 Gauss/cm) described in sections 2.3.1-2.3.3. During the period these gradients are on, the frequencies at which the spins are precessing in a voxel become dependent on their spatial coordinates \vec{r} :

$$\omega(\vec{r}) = \gamma (B_0 + \vec{G} \cdot \vec{r}) \quad (2.15)$$

where \vec{G} is the magnetic field gradient vector. The signal from all voxel magnetizations excited by the RF pulse can be written as:

$$S(t) = \int_V m(\vec{r}) \exp(-i\gamma\vec{G}\cdot\vec{r}) d\vec{r} \quad (2.16)$$

where $d\vec{r}$ represents volume integration and the coefficient $m(\vec{r})$ represents the spin density, $\rho(\vec{r})$, weighted by the longitudinal relaxation time T_1 and the transverse relaxation time T_2 (here the precession due to the B_0 is ignored). To decode the acquired MR signal, an inverse Fourier transform is used. Fortunately, Eqn. 2.16 already has the form of the Fourier transformation, where the notion of a reciprocal vector or “k” vector is useful:

$$\vec{k} = \frac{1}{2\pi} \gamma\vec{G}t \quad (2.17)$$

and Eqn 2.16 can then be written as:

$$S(t) = \int_V m(\vec{r}) \exp(-i2\pi\vec{k}\cdot\vec{r}) d\vec{r} \quad (2.18)$$

with \vec{k} having the units of spatial-frequency, typically cycles/cm. If $S(t)$ is equivalent to the Fourier transform of $m(\vec{r})$, this means that at any given time t , $S(t)$ equals the value of the Fourier transform of $m(\vec{r})$ at some spatial frequency. This Fourier transform space shown for the case of a 2-D image in Fig. 2.4 below is often called “k-space”.

To form an image, the required set of $\{S(t)\}$ should cover a sufficient part of k-space (determined by the Nyquist criterion; signal must be sampled at a rate equal to at least twice the highest frequency component in the signal) to allow reconstruction of $m(\vec{r})$. This Fourier space interpretation greatly facilitates the design and analysis of imaging methods. The total recorded signal, $S(t)$, that maps directly to a trajectory

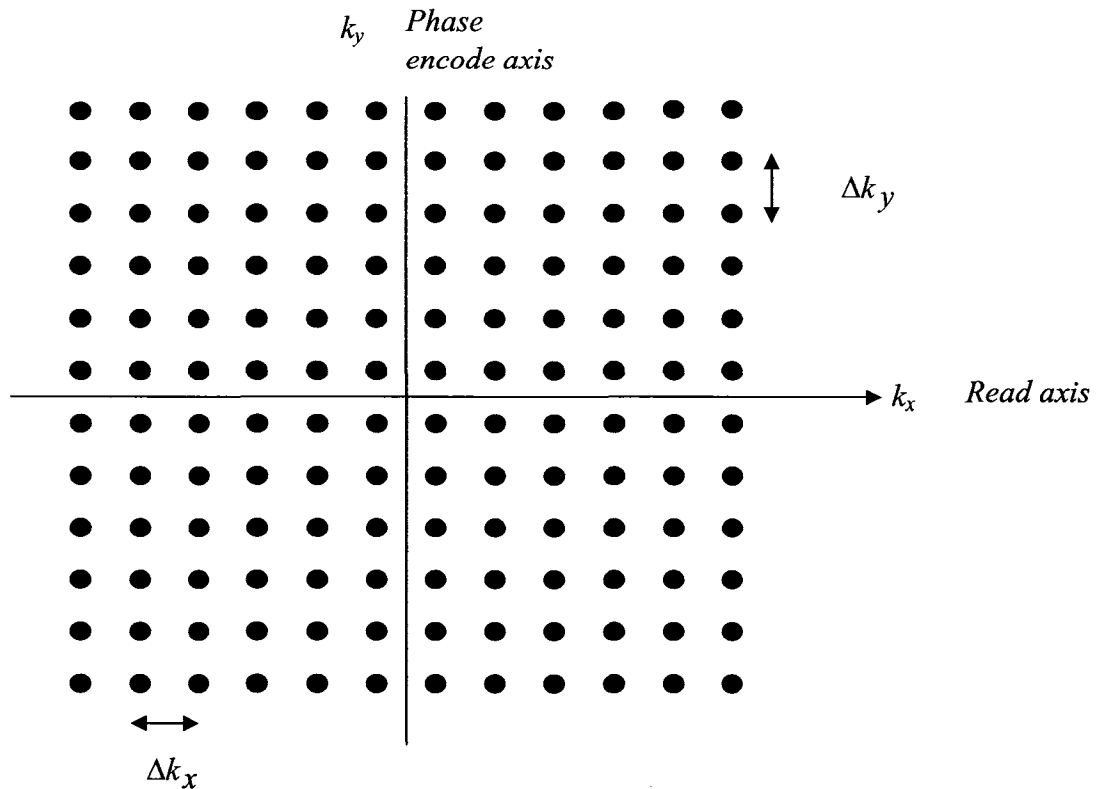


Fig. 2.4: The k -space coverage for a 2-D image. The dots represent discrete samples of k -space. The vertical and the horizontal axis are also known as the phase encode and the read encode axis respectively.

through spatial-frequency (Fourier space) is determined by the time integrals of the orthogonally applied gradient waveforms given by $G_x(t)$, $G_y(t)$, and $G_z(t)$. These magnetic gradient fields are obtained by superposing additional weaker magnetic fields in the same direction as the \vec{B}_0 field but with the amplitude changing linearly with position. For example, an x -gradient has a variation in the x -direction of the z component of the applied field given by:

$$\frac{dB_z}{dx} = G_x \quad (2.19)$$

The actions of these waveforms are described through the following MR imaging encoding processes.

2.3.1 Selective Excitation

The use of a magnetic field in conjunction with limited bandwidth RF can excite MR signals only in a single slice of the imaging volume. This is achieved by applying the B_1 field (RF pulse) in the presence of a linear gradient magnetic field, $G_z(t)$, conventionally in the z -direction. With G_z on, and because B_1 must be tuned to the Larmor frequency for excitation to occur, B_1 is now only effective over a frequency bandwidth that matches the bandwidth of the resonance frequencies of spins in the slice of interest. This gradient is applied on an axis perpendicular to the chosen slice plane. This bandwidth is given by $\gamma G_z \Delta z$ and is centered about ω_0 for excitation of the plane at $z = 0$ where Δz is the slice thickness. The extent by which the magnetization is nutated when an RF pulse of duration τ is applied is given by Eqn. 2.10.

2.3.2 Frequency Encoding

This is a method for obtaining spatial information in one direction, whereby a gradient is on at the same time that the MR signal is being sampled or acquired. Thus, having selected a specific plane using the localization in the z -axis (as described above), the transverse magnetization along the x -axis is resolved using a second gradient G_x (also referred to as the read-out gradient) with all the other orthogonal gradients turned off. The bandwidth of the received signal is given by:

$$\Delta\omega(x) = \gamma G_x FOV_x \quad (2.20)$$

where FOV_x is the field of view in the x -direction and the sampling interval Δt is given by:

$$\Delta t = 2\pi / \Delta\omega (x). \quad (2.21)$$

This is related to the total sampling time by:

$$T_x = N_x \Delta t \quad (2.22)$$

where N_x is the number of samples. The variables G_x and Δt determine the k-space increment in the x-direction given by:

$$\Delta k_x = \gamma G_x \Delta t \quad (2.23)$$

2.3.3 Phase Encoding

The final step required to produce a 2-D image of the excited slice involves application of a positionally-dependent phase change to the transverse magnetization along the third remaining principal y-axis of the image plane. This is achieved by applying a gradient field in the y-direction, G_y , for a duration of time, T_y . This phase change is incremented from view-to-view by changing G_y by the amount ΔG_y for N_y phase-encode steps. G_y and T_y both determine the incremental k-space values in the y-direction $\Delta k_y = \gamma \Delta G_y T_y$. Hence, for each phase encode step, G_y is held constant and the projection along the x-direction is measured. The 2-D MR image acquisition matrix is usually given by $N_x \times N_y$. The scan time T_{aq} (typical scan time of ~5 minutes) is determined by, the number of excitations N_{ex} , N_y and the repetition time TR of the imaging sequence such that:

$$T_{aq} = N_y N_{ex} TR \quad (2.24)$$

To be able to obtain 3-D or volumetric images one has to replace the slice-selective gradient along the z -direction by a second phase encoding in the slice select direction. This can then be repeated N_z times for each value of the other phase gradient (in the y -direction) to complete a 3-D k-space matrix from which a 3-D image can then be obtained by doing a 3-D Fourier transform. This has the advantage of providing a signal-to-noise ratio (SNR) improvement of factor $\sqrt{N_z}$ over 2-D multi-slice imaging since the entire volume contributes signal for each of the $N_y N_z$ excitations. The main disadvantage with 3-D imaging is that the scan time can be prohibitively long (≥ 1 hour) if N_y or N_z are large or TR is long since T_{acq} becomes:

$$T_{acq} = N_y N_z N_{ex} TR \quad (2.25)$$

These encoding processes can be combined with a sequence of RF pulses to generate images of desired contrast through what are called pulse sequences, with the basic or common pulse sequences described in the next section. Of particular interest is the generation of echoes for signal acquisition, where phase shifts are removed momentarily, thereby improving the coherence and strength of the signal. These echoes are of two types: spin echoes (undoing of phase shifts from field inhomogeneities and chemical shifts), gradient echoes (undoing or rephasing of phase shifts from gradient fields).

2.4 Basic MR Imaging Pulse Sequences

In this section a brief description of some of the basic imaging methods and/or sequences to obtain MR images is given. The gradient-echo sequence provides the basis

of the Look-Locker imaging method to be described later in Chapter 3. The multiple spin-echo sequence is used to estimate the T_2 time constant in subsequent chapters.

2.4.1 Gradient Echo Sequence

In a reference frame rotating at the central (Larmor) frequency, ω_0 , phase accrues from off-resonance sources due to magnetic field inhomogeneity, chemical shifts and applied gradient fields. Assuming perfect B_0 homogeneity and no chemical shift, the effect on the signal phase from the gradient field is [91]:

$$\phi(\vec{r}, t) = \gamma \int_0^t \vec{G}(\vec{r}, \tau) \cdot \vec{r} d\tau \quad (2.26)$$

A gradient echo occurs when $\phi(\vec{r}, t) = 0$, that is when two gradient lobes of opposite polarity are sequentially imposed along one gradient axis. To achieve this, a gradient lobe of negative polarity in the read-out direction is turned on for a duration τ_{deph} . This creates a systematic dephasing by warping the spin phases over space, thus the received signal decays faster than the intrinsic T_2 of the material characterized by the relaxation time constant T_2^* defined as [91]:

$$\frac{1}{T_2^*} = \frac{1}{T_2} + \frac{\gamma \Delta B}{2} \quad (2.27)$$

where ΔB is the static magnetic field (B_0) inhomogeneity.

At this point the polarity of the gradient field is reversed and any phase warping (i.e. loss of coherence) accrued from the time period the dephasing gradient field was initiated is then “unwound” or rephased because spins that were precessing at a lower

frequency are now precessing at a corresponding higher frequency. An echo begins to form as the spins gain coherence and at time τ_{deph} , equal to the duration the negative

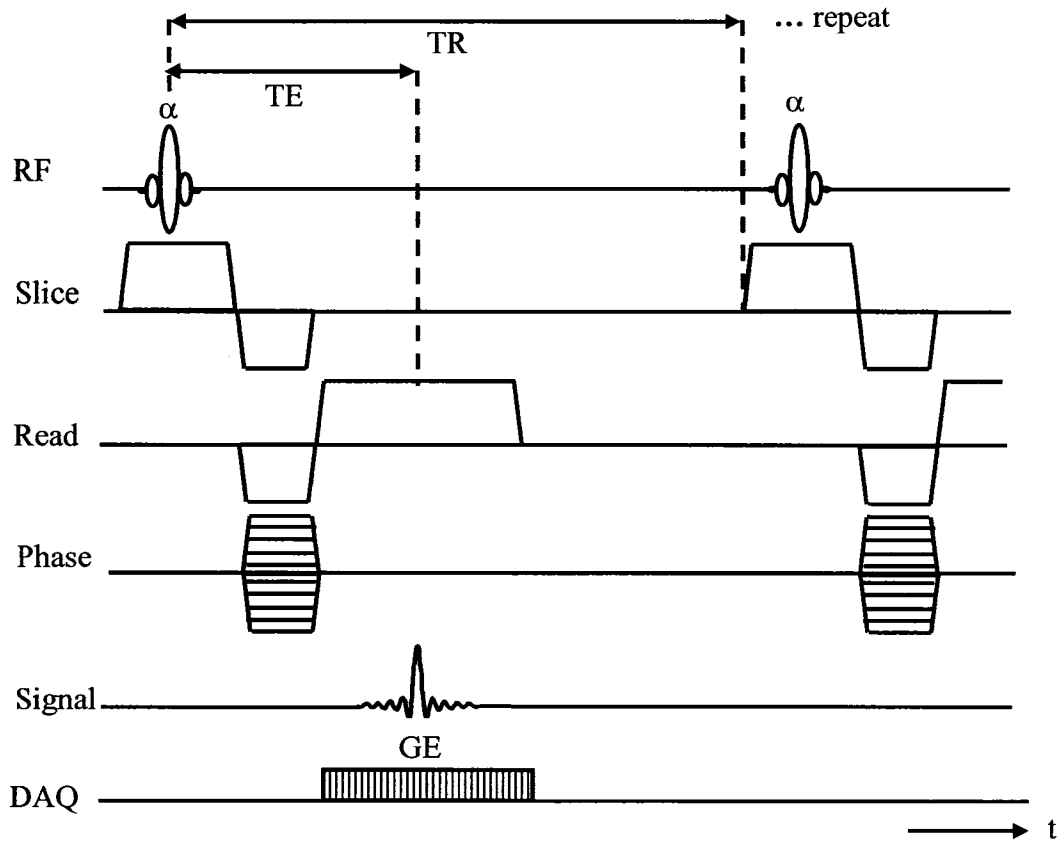


Fig. 2.5: A gradient echo imaging pulse sequence timing diagram. DAQ stands for the data acquisition.

lobe is applied, an echo is formed. Before the application of the frequency-encode gradient, a slice-selective RF pulse is applied in conjunction with a slice-select gradient to nutate the magnetization by an angle between 0 and 90° from the z -axis. A phase-encoding gradient is then applied together with the negative read encoding gradient. Images acquired using a gradient echo sequence usually provide images with high T_2^* contrast and the acquired signal decay is defined by the relation in Eqn. 2.11 except that

T_2 is replaced with T_2^* and t is replaced with the echo time TE. A depiction of a gradient echo imaging sequence is given in Fig. 2.5.

2.4.2 Spin-Echo Sequence

Fig. 2.6 depicts a spin-echo imaging sequence. First a slice selective 90° RF pulse is applied in the presence of a slice select gradient. A phase-encoding gradient is then applied together with a frequency-encode gradient to dephase the spins. The frequency-

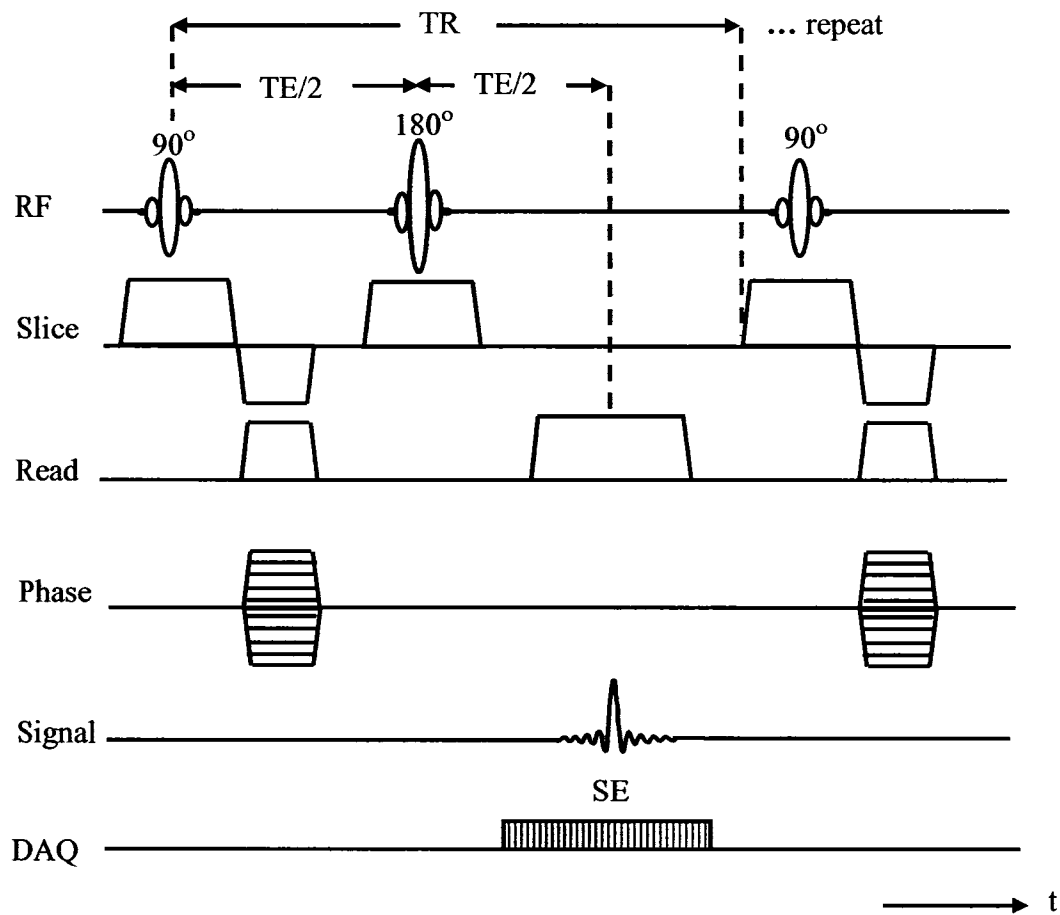


Fig. 2.6: A spin-echo imaging pulse sequence timing diagram.

encode gradient is applied so that spins will rephase at the center of the echo or data acquisition (DAQ). To rephase the spins, a slice selective 180° RF pulse is then applied in the presence of a slice-select gradient, and finally a frequency-encode gradient is applied to encode the echo centered at the DAQ at the echo time, TE. The 180° RF pulse refocuses dephasing from static B_0 inhomogeneities including gradients, chemical shifts, and/or sample susceptibility differences leaving a signal weighted by T_2 . This sequence of RF and gradient pulses is then repeated for different phase-encode gradient amplitudes. Images acquired using a spin-echo sequence usually provide images with high T_2 contrast and can be used to generate T_2 maps from images acquired at different echo times TE. The magnitude of the acquired signal decay is defined by the relation in Eqn.2.11 with $t = TE$. This equation can be used to estimate the spin-spin relaxation time T_2 from data acquired using a pair of spin echoes.

A diagram of the spin system behaviour for a spin-echo sequence is given in Fig.2.7 where Fig. 2.7 (b) shows the spin system after time $TE/2$ following the 90° and just before the 180° RF pulse, (c) is the system just immediately following the application of the 180° pulse, and (d) an echo is formed at time TE following the first 90° pulse.

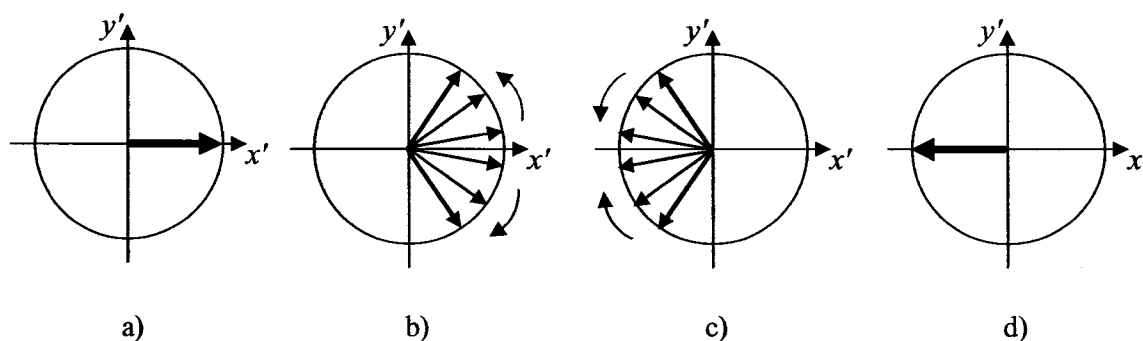


Fig. 2.7. Diagram of the magnetization behaviour during a spin-echo pulse sequence.

Variants of the spin-echo sequence are the Carr-Purcell (CP) and the Carr-Purcell-Meiboom-Gill (CPMG) or multi-slice multiple spin-echo (MEMS) pulse sequences which both use a train of 180 degree pulses applied after a single excitation to generate a series of spin echoes. The CP and the CPMG (or MEMS) pulse sequence can be written using the notation $\{90-x' - 180-x' - 180-x' \dots - 180-x'\}$ and $\{90-x' - 180-y' - 180-y' \dots - 180-y'\}$ respectively. In the CPMG sequence shown in Fig. 2.7, the phase of the refocusing pulses is shifted by $\pi/2$ with respect to the phase of the excitation (90°) pulse. The CPMG (or MEMS) imaging sequence unlike the CP imaging sequence is more conventionally used for estimating the T_2 parameter because it does not lead to accumulation of errors due to imperfect 180° pulses. The use of a series of spin echoes increases the accuracy of the estimated T_2 without significantly lengthening the acquisition time compared to the case of using a pair of single spin echoes. The magnitude of the acquired signal from the various spin echoes can be written as:

$$S(nTE) = S(0)e^{-nTE/T_2} \quad (2.28)$$

where $n = 1, 2, \dots, N$ with N being the total number of spin echo images acquired and $S(0)$ the signal immediately after excitation.

2.4.3 Inversion Recovery Sequence

Another useful sequence is illustrated in Fig. 2.8 is the inversion recovery (IR) sequence which provides images with high T_1 contrast and can be used to generate T_1 maps of samples or tissues. It can employ either the gradient echo or the spin echo for

image formation; the sequence in Fig. 2.8 utilizes a gradient echo. The sequence employs a preparatory 180° RF pulse in the presence of a slice-select gradient followed by a 90° RF read-out pulse after a waiting time of inversion time (TI). The next pair of 180° - 90° RF pulse is applied after a dead time of about $3T_1$ for a different TI to sample the next point in the magnetization recovery curve of the sample being imaged. This is repeated for the desired number of TI points sufficient to characterize the complete recovery curve. But because of the long waiting time required coupled with the number of phase

$$S(TI) = S(0)\left(1 - 2e^{-TI/T_1}\right) \quad (2.29)$$

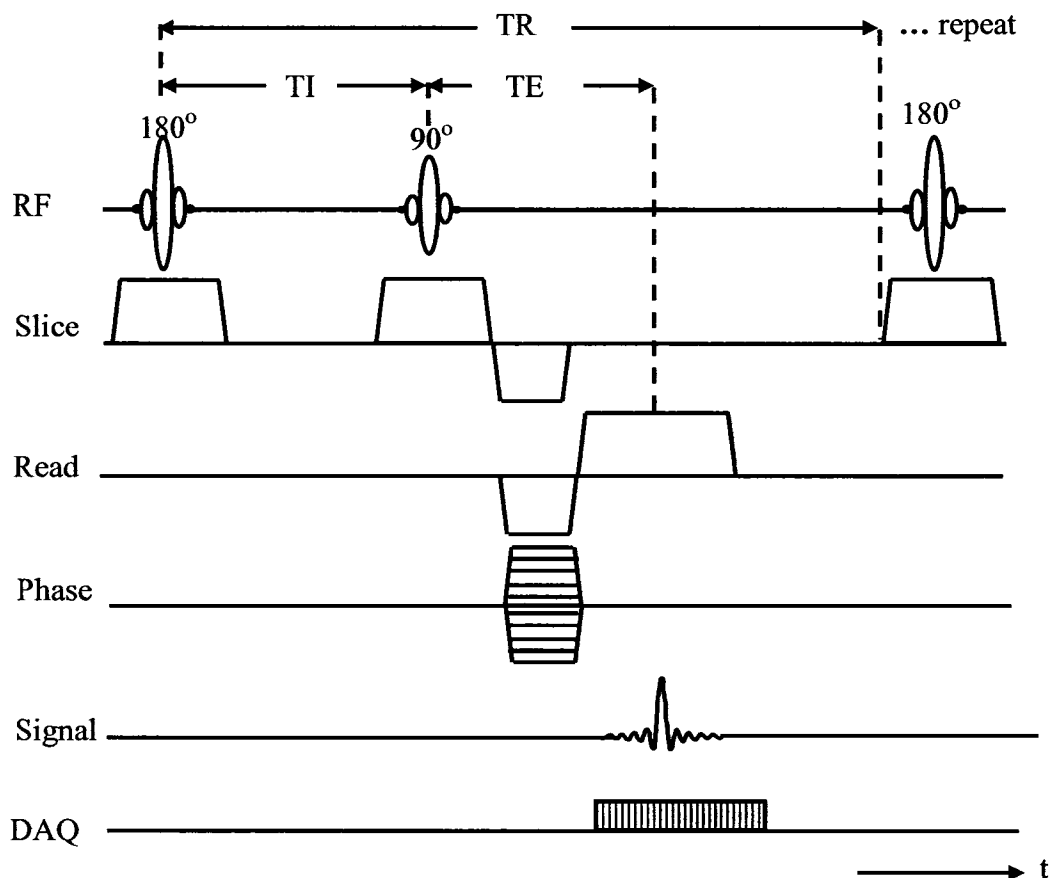


Fig. 2.8: A simple inversion recovery imaging sequence diagram.

encodes required to obtain a workable image (usually ≥ 64) the imaging time using this method can be prohibitively long. The magnitude of the signal from these TI images can be written as:

2.5 Polymer Gel Dosimetry

As described in chapter 1, the ability of MR imaging to probe polymer gel dosimeters is due to radiation-induced alteration of the physical and/or chemical properties of the gel dosimeter and subsequent changes in the inherent relaxation time parameters T_1 and/or T_2 .

2.5.1 Transverse and Longitudinal Relaxation Times

Relaxation occurs because of interactions between spins and other types of magnetic moments such that spins experience time-dependent magnetic or electric fields. These types of interactions could be spin-rotational, anisotropic chemical shift, scalar, quadrupolar. For gel dosimeters used in these studies relaxation is primarily through dipole-dipole interactions, with the interactions taking place between the spins themselves in either the same or different chemical environment. The theory of NMR relaxation phenomena in liquids was formulated shortly after World War II [28,90,94,95] and is also known as the BPP theory named after Bloembergen, Purcell and Pound [8]. The theory which follows considers only spins of value $I = \frac{1}{2}$ (i.e. protons) and follows that given in [28].

For a system of two identical spins \vec{I} and \vec{S} interacting with each other having gyromagnetic ratios, γ_I, γ_S respectively, the equations of motions for the observable quantities $\vec{I}_z + \vec{S}_z$ (longitudinal) and $\vec{I}_x + \vec{S}_x$ or $\vec{I}_y + \vec{S}_y$ (transverse) are given by [28]:

$$\frac{d}{dt}(\vec{I}_z + \vec{S}_z) = -2(W_1 + W_2)(\vec{I}_z + \vec{S}_z - I_0 - S_0) \quad (2.29)$$

$$\frac{d}{dt}(\vec{I}_x + \vec{S}_x) = -2(U_1 + U_2)(\vec{I}_x + \vec{S}_x) \quad (2.30)$$

where I_0 , and S_0 are the equilibrium values of the magnetic moments of spins \vec{I} and \vec{S} , and \vec{I}_z and \vec{S}_z denote the average values of the longitudinal component of the magnetic moment. W_1 , and W_2 , are the transitional probabilities per unit time for the longitudinal components between two eigenstates $|m_i\rangle$, $|m_j\rangle$ of the unperturbed Hamiltonian of the two particles with spin \vec{I} and \vec{S} in a magnetic field B_0 along the z axis. U_1 and U_2 are the transition probabilities per unit time between the eigenstates of the transverse components of the magnetic moments. This Hamiltonian is given by [28]:

$$H = -\hbar\gamma_I B_0 I_z - \hbar\gamma_S B_0 S_z + H' \quad (2.31)$$

where the first two terms are the Zeeman Hamiltonian terms and H' is the time-dependent perturbation term Hamiltonian for either the spin-spin interaction or interaction between the spin and the RF field. This perturbation term for the case of the dipole-dipole interaction is given by [28]:

$$H' = \frac{-\hbar^2 \gamma_I \gamma_S}{r^3} [3(\vec{I} \cdot \vec{r})(\vec{S} \cdot \vec{r}) - \vec{I} \cdot \vec{S}] \quad (2.32)$$

where r is the separation between the two spins and \vec{r} is the distance unit vector. These eigenstates have corresponding energies E_i and E_j of the perturbed Hamiltonian from the

spin-spin interaction on the Zeeman energies of the spins in a constant magnetic field. The transitional probabilities can be calculated for the equations of motion of the longitudinal components using the equation given below [28]:

$$W_{ij} = \frac{1}{t} \frac{1}{\hbar^2} \left| \int_0^t \langle m_j | H'(t') | m_i \rangle \exp(-i\omega_{ij}t') dt' \right|^2 \quad (2.33)$$

For the transverse components, the defined eigenstates of the spins $|a\rangle$ and $|b\rangle$ are not eigenstates of the energy but can be expanded in terms of eigenvectors of the energy with coefficients a_i and b_j . The transition probabilities per unit time between these states for the equations of motion for the transverse components of the magnetic moment can be calculated using the relationship [28]:

$$U_{ab} = \frac{1}{t} \frac{1}{\hbar^2} \left| \int_0^t \sum_{ij} \langle m_j | H'(t') | m_i \rangle a_i b_j \exp(-i\omega_{ij}t') dt' \right|^2 \quad (2.34)$$

where $\omega_{ij} = (E_j - E_i)/\hbar$. From the computed values of transition probabilities [7,8] in a homogeneous system ($\omega_l = \omega_s = \omega$), the exponential solutions of Eqns (2.29) and (2.30) can be expressed as:

$$\frac{1}{T_1} = 2(W_1 + W_2) \quad (2.35)$$

$$\frac{1}{T_2} = 2(U_1 + U_2) \quad (2.36)$$

These relaxation times can be calculated to give [28]:

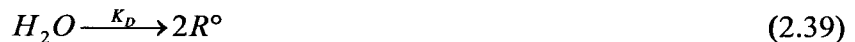
$$\frac{1}{T_1} = \frac{6}{20} \frac{\hbar^2 \gamma^4}{r^6} \left[\frac{\tau_c}{1 + \omega^2 \tau_c^2} + \frac{4\tau_c}{1 + 4\omega^2 \tau_c^2} \right] \quad (2.37)$$

$$\frac{1}{T_2} = \frac{3}{20} \frac{\hbar^2 \gamma^4}{r^6} \left[3\tau_c + \frac{5\tau_c}{1 + \omega^2 \tau_c} + \frac{2\tau_c}{1 + 4\omega^2 \tau_c^2} \right] \quad (2.38)$$

where τ_c is the correlation time and ω the Larmor frequency of the spin. The linear term in τ_c given by $3\tau_c$ in Eqn 2.38 is the primary reason why the relaxation rate parameter $1/T_2$ as opposed to $1/T_1$ is the primary parameter used in quantification of the relative effect of radiation in polymer gel dosimeters.

2.5.2 Chemical Mechanisms of Polymer Gel Dosimeters

A gel dosimeter is a gel matrix (or hydrogel) in which chemicals (monomers for polymer gels) which react to radiation are dissolved. These dosimeters generally have a high water content (~90%) and it is the radicals produced from the radiolysis [96] of water that affect the dissolved solutes which bring about the chemical changes which can then be measured; not the radiation effect on the solute itself. The most prevalent free radicals formed in the time span of $\sim 10^{-8}$ s following irradiation exposure are (i) the aqueous electrons, (ii) the hydroxyl radical (OH^\cdot) and (iii) the hydroxonium ion (H_3O^+). These radicals can react with monomers present in the gel dosimeter. The decomposition of intermediaries can be written as a simplified reaction in which the reaction rate is proportional to the absorbed dose [96,97].



where R° denotes the radicals formed from water. For the purpose of this work only a brief review of the polymerization process induced by radiation is presented below and can be summarized into the following three stages described by *de Deene et al* [97]:

1. *Initiation*: The radicals R° initiate the polymerization of monomers M_n by binding to an electron of the double bond of the monomer. This step can be written as:



where $K_i(n)$ is the reaction rate constant. Initially, there is no polymer in the gel and n will be equal to one, but as the cross-linking monomers have 2 double bonds on the same molecule, there can be reactive double bonds on the cross-linking polymer. Thus, during polymerization there may be monomers M_n consisting of n monomer units that react with the radicals.

2. *Propagation*: The polymer chains grow as a result of the propagation of chain reactions (with reaction rate constant $K_p(n,m)$) by which the created monomer and polymer radicals react further with other monomers or polymer chains:



3. *Termination*: This usually takes place by the combination of two radicals or by disproportionation (chemical reaction in which a single reactant breaks up to produce 2 different products) involving hydrogen abstraction resulting in two dead chains. Also termination may take place by the transfer of radical groups to other molecules with the agent being either the growing polymer chain or the gelatin polymer. The decrease of polymerization rate with increasing gelatin concentration has been observed providing evidence of gelatin moderating the polymerization, possibly through chain transfer reactions or through scavenging of initiating fragments by the gelatin molecules [98]. If oxygen is present in the gel, peroxide radicals are created and will quickly react with other radicals leading to a termination. The presence of oxygen is usually undesirable and

is usually removed by either purging the gel solution with inert gases (nitrogen or argon) or using anti-oxidants.

2.5.3 NMR Response of Polymer Gel dosimeters

Most spin systems are heterogeneous and the spins exist in different environments where they may experience different interactions or undergo different motions on different time scales. Polymer gels for example contain polyacrylamide protons, gelatin protons, water protons hydrating the polyacrylamide, gelatin protons and bulk water protons. Each of these spin groups has inherent relaxation properties determined by the molecular dynamics and interactions experienced by the spins. Usually these spin groups are not isolated and exchange with each other so that the overall observed relaxation differs from the inherent relaxation of the individual groups. The observed relaxation rates are complex functions of the inherent relaxation rates, the exchange rates or times between the different environments and the physical spin fractions [6,50].

If the exchange times of protons between the various environments are long compared to the inherent relaxation times of these environments, the NMR signal is the same as the sum of the signals from the isolated, non-exchanging environments. When this happens the magnetization evolution is multi-exponential of which the population fractions of the different pools determines the weighting factors of the different exponential components. This is otherwise known as slow exchange. For intermediate exchange, where the exchange time is about the same as the relaxation times, the observed relaxation rates and the magnetization weightings are complex functions of the inherent relaxation times and exchange times. But if these exchange times are short

compared to the relaxation times but still long compared to the correlation times (fast exchange limit), the observed magnetization evolution will be mono-exponential with a relaxation rate [94,97,99,143]:

$$R_2 = f_{mob}R_{2,mob} + f_{poly}R_{2,poly} + f_{gela}R_{2,gela} \quad (2.42)$$

where f_i is the fraction of spins in each of the environments in the system with *poly* referring to protons in the radiation formed polymer environment, *gela* to those in the gelatin environment and *mob* to those protons in the remaining or bulk environment which is the mobile proton group (free water and monomer protons). The proton fractions satisfy the condition $f_{mob} + f_{poly} + f_{gela} = 1$. For polymer gel dosimeters, the protons in the various environments are in a fast exchange regime with each other [99]. Eqn 2.42 defines how an increase in R_2 with dose results from an increase in polymer concentration. Thus the extent of the resulting polymerization reaction is dose dependent. These polymer aggregates influence the mobility of the surrounding molecules and according to the theory of Bloembergen-Purcell-Pound [90,95] given in Eqn.2.38, this results in a change in the spin-spin relaxation rate.

The dose dependence or response of the spin lattice relaxation time, T_1 , for polymer gels is not as pronounced as that for the spin-spin relaxation time, T_2 , and the exchange regime is more complicated [99].

Chapter 3

3-D Look-Locker Imaging Method for T_1 Estimation

3.1 Introduction

In Fricke 3-D gel dosimetry the ionizing radiation absorbed is inversely proportional to the T_1 of the irradiated gel due to the conversion of ferrous to ferric ions. These gels face the problem of loss of spatial information due to the diffusion of ferric ions from their formation sites, thereby requiring fast and efficient acquisition methods to limit this effect.

The Look-Locker [100] 2-D imaging [101] scheme is a useful time saving approach for T_1 measurement. This method uses a train of small tip angle RF pulses to sample the longitudinal magnetization recovery curve for a given phase encode and it has been shown to provide highly efficient and accurate T_1 estimation in the time frame of a few minutes [102,103]. However, extension of this method to volumetric (i.e. 3-D) image acquisition is not very practical since it is expected to be very time consuming (approximately 1 hour depending on the number of slices), which would prohibit its routine clinical use especially for gel dosimetry. *Henderson et al* [104] have suggested a method for the rapid acquisition of 3-D images for the estimation of T_1 , based on the 2-D Look-Locker (LL) imaging principle but with appropriate segmentation of k-space [104]. This 3-D LL method has been shown to have an efficiency even higher than that of a 2-D LL imaging sequence [105]. With the 3-D LL method [104], the small tip angle RF

pulses are delivered as rapidly as possible and equally spaced in time ($\tau=10\text{ms}$) to reduce image acquisition time. However, this limits the available SNR since only small tip angles ($\leq 5^\circ$) can be used in order to preserve dynamic range by not driving the magnetization too quickly to steady state.

This chapter is based on the article by *Nkongchu* and *Santyr* [106] and describes a method based on the 3-D LL approach suggested by *Henderson et al* [104] with the addition of a variable delay between successive inversion time (TI) point images. This additional delay allows more magnetization recovery between TI images thus permitting the use of larger tip angle RF pulses ($>5^\circ$) without sacrificing the dynamic range. The larger tip angles give a significant improvement in SNR for a small increase in scan time, thereby providing less noisy data for the estimation of 3-D T_1 maps. A general theoretical and experimental characterization of the magnetization evolution is described for this improved 3-D LL imaging sequence. The improved accuracy and precision of the method is compared to the conventional 3-D LL approach and is demonstrated in phantoms covering a range of T_1 expected in vivo including the range of T_1 ($\sim 200\text{ ms} - 1000\text{ ms}$) for PVA-Fricke gels.

3.2 Theory

Fig. 3.1 shows the 3-D modified imaging LL sequence diagram implemented in this work. In the implementation of this fast 3-D LL sequence, a non-slice selective inversion pulse $\alpha = \pi$ is used to completely invert the longitudinal magnetization (a tangential adiabatic pulse [107] was used in this work) prior to the acquisition of each segment of k_y

space for a fixed k_z value. After the inversion pulse, a series of small flip angle slab selective readout pulses, β , separated by a time interval, τ , are used to rapidly and repeatedly sample the recovery of the longitudinal magnetization. A gradient echo is used

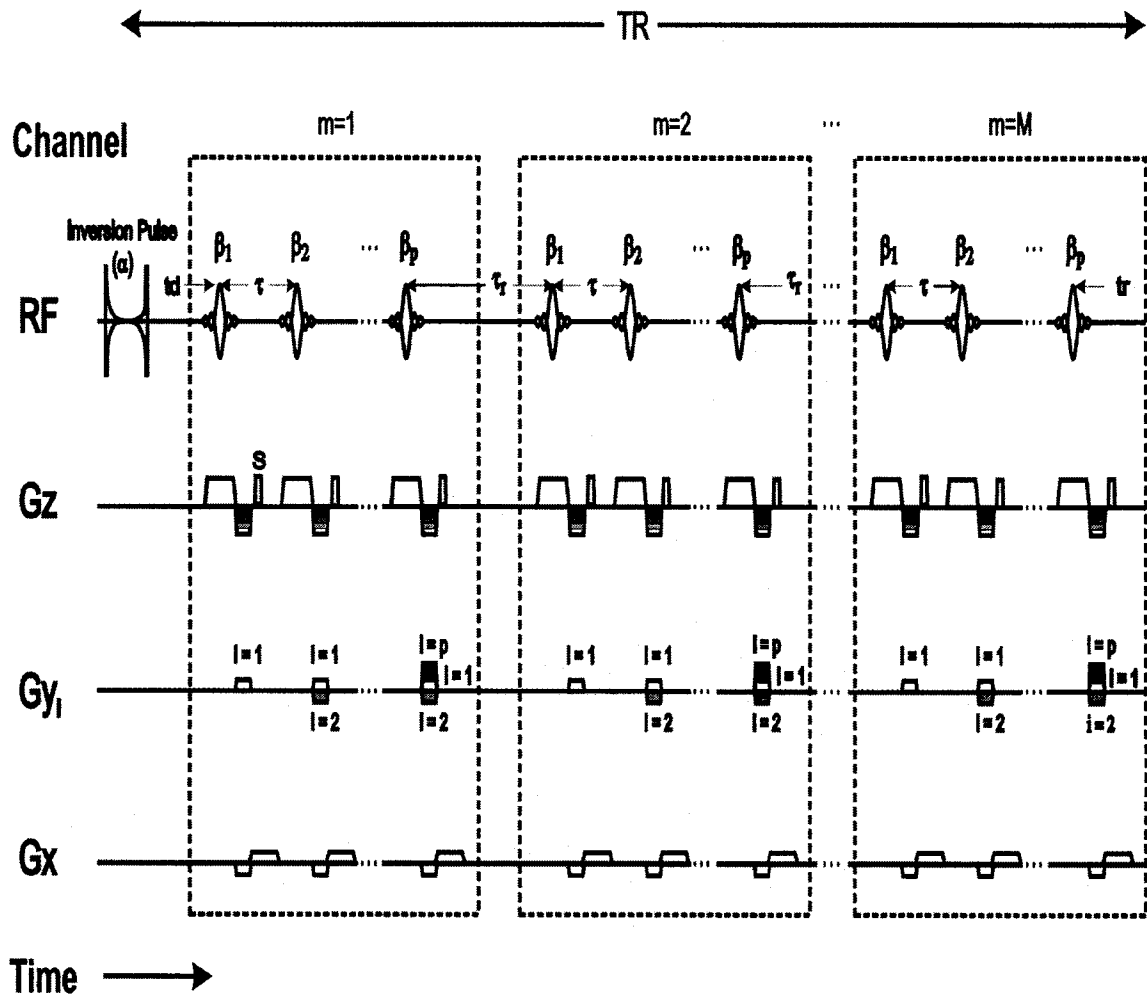


Fig. 3.1. The 3-D LL pulse sequence for a given segment acquiring P phase encode lines for each m group. The τ_r is $\geq \tau$ permitting increased longitudinal magnetization, M_z before the application of the next group of β pulses m representing the next “effective” TI image. α is a tangential adiabatic frequency modulated pulse with a constant phase and amplitude, and S the spoilers.

to sample k_x space following each β pulse for each k_y phase encoding step in the given segment (the number of k_y lines, P , per segment is typically 16). Any residual transverse magnetization, which might interfere with the signal from the next β pulse, is completely spoiled after each gradient echo using a spoiler gradient S .

To sample the recovering magnetization, the segment of P β pulses is re-applied m times ($m = 1, 2, \dots, M$), each separated by a delay time τ_r , where m defines the number of sample, M defines the total number of samples of the recovery curve and τ_r determines the spacing between these samples. $N = PM$ defines the total number of RF pulses following the inversion pulse. More specifically, the “effective” inversion time TI_{eff} for each sample can be defined as:

$$TI_{eff} = (n-m)\tau + (m-1)\tau_r,$$

where n is defined as the number of β assigned to the centre of k -space. This sequence of an inversion pulse followed by N small tip angle pulses is repeated for the number of segments (e.g. 4,8) required to fill k_y space and the entire acquisition is repeated for each k_z value (with phase encoding done in the slice-selective direction or z -direction). To ensure that the TI_{eff} values most closely approximate the sampled recovering magnetization, the k_y lines for a given k_z line are acquired in an interleaved and centric method [104]. In the implementation of *Henderson et al* [104], there is no additional recovery delay τ_r (i.e. $\tau_r = \tau$) and since N can be high (e.g. > 150 since P can be quite large for maximum efficiency (e.g. 32)), steady state can be achieved before adequate sampling of the recovery curve occurs, especially for large tip angles. The principal difference this pulse sequence introduces is that τ_r can be made much larger than τ allowing partial recovery of the magnetization before the next TI_{eff} sample allowing the use of larger tip

angles. This results in a substantial improvement in data quality for a small (typically 10 – 20 %) increase in measurement time. At the end of the entire train of N pulses, an optional recovery, t_r , time is inserted, permitting complete recovery of the longitudinal magnetization prior to the next inversion pulse. The subscripts of β in Fig. 3.1, represent the phase encode line number being acquired. Thus the repetition time can be defined as:

$$TR = t_d + M(P-1)\tau + (M-1)\tau_r + t_r.$$

The derivation of the signal strength equation for the 3-D LL imaging sequence follows that for the 2-D LL method given in *Brix et al* [101], modified to include the recovery time interval τ_r . The longitudinal magnetization, M_n , just before the n^{th} β pulse is given by the relation:

$$M_n = M_{eq} \left[F + (Q - F) \{ \cos(\beta) E_\tau \}^{n-m} \{ \cos(\beta) E_{\tau_r} \}^{m-1} \right], \quad (3.1)$$

where,

$$F = \frac{1}{1 - E_{\tau_r} E_\tau^{P-1} \cos^P(\beta)} \left[(1 - E_\tau) \cdot \left\{ \frac{1 - (E_\tau \cos(\beta))^{P-1}}{1 - E_\tau \cos(\beta)} \right\} + (1 - E_{\tau_r}) (E_\tau \cos(\beta))^{P-1} \right]$$

$$Q = \frac{(D + G) \cos(\beta) \cos(\alpha) E_{tr} E_d + (1 - E_{tr}) E_d \cos(\alpha) + (1 - E_d)}{1 - \{ E_\tau^{N-M} E_{\tau_r}^{M-1} \cos^{N-1}(\beta) \} \cos(\beta) \cos(\alpha) E_{tr} E_d},$$

$$D = F \{ 1 - (E_\tau \cos(\beta))^{P-1} \} \frac{1 - \{ E_{\tau_r} E_\tau^{P-1} \cos^P(\beta) \}^M}{1 - \{ E_{\tau_r} E_\tau^{P-1} \cos^P(\beta) \}},$$

$$G = (1 - E_{\tau_r}) \{ E_\tau \cos(\beta) \}^{P-1} \frac{1 - \{ E_{\tau_r} E_\tau^{P-1} \cos^P(\beta) \}^{M-1}}{1 - E_{\tau_r} E_\tau^{P-1} \cos^P(\beta)},$$

$$E_{\tau_r} = \exp(-\tau_r/T_1), E_\tau = \exp(-\tau/T_1), E_d = \exp(-t_d/T_1), E_{tr} = \exp(-t_r/T_1).$$

Here n is the number of the β pulse at which the centre of k space is acquired and is given by $n = f(m)$ e.g. $f(m) = P(m-1)+8$ (with $m = 1,2\dots M$), Q is the ratio of the longitudinal magnetization just before the β_1 pulse and the equilibrium magnetization M_{eq} , and F is the longitudinal magnetization as the number of β pulses, N , approaches infinity. When $\tau = \tau_r$, it can be shown that the above expressions (M_n , F , and Q) simplify to the equations of the conventional 3-D (or 2-D) LL imaging sequence [101,104]. The signal or image intensity at a given pixel (i,j) for a given slice is then given by the relation [101]:

$$S_n(i, j) = |\sin(\beta) M_n(i, j) \exp(-TE/T_2^*(i, j))|, \quad (3.2)$$

Note that Eqn. (3.2) can also be rearranged into the form of a conventional inversion recovery type equation from which the T_1 can be extracted:

$$S(i, j) = \left| A(i, j) \left\{ 1 - DR(i, j) \cdot \exp(-TI/T_1^*) \right\} \right|, \quad (3.3)$$

where,

$$TI = TI_{eff},$$

$$\frac{1}{T_1^*} = \frac{1}{T_1} - \frac{\ln(\cos\beta)}{\{(N-M)\tau + (M-1)\tau_r\}/(N-1)}, \quad (3.3a)$$

$$A = M_{eq} F \sin(\beta), \quad (3.3b)$$

$$DR = -\frac{1}{F} \left\{ \frac{-(D+G)\cos(\beta)E_{tr}E_d - 2E_d + E_{tr}E_d + 1}{1 + (E_\tau^{N-M} E_{\tau_r}^{M-1} \cos^{N-1}(\beta)) \cos(\beta) E_{tr}E_d} - F \right\}. \quad (3.3c)$$

Recall that $N = PM$ is the total number of RF pulses following inversion, P is the number of phase encode lines acquired per segment. Here one would effectively do a three-parameter fit of Eqn. (3.3) to the pixel magnitude signals as a function of T_{1eff} yielding values for A , DR and T_1^* . T_1 is then extracted from T_1^* using Eq. (3.3(a)).

3.3 Methods

The 3-D LL sequence was implemented at 1.89T (Magnex Scientific, Abingdon, Oxon, England) using a 12 cm internal diameter transmit/receive birdcage coil (Morris Instruments Inc. Ottawa). All measurements were performed at room temperature. The parameters for the 3-D LL imaging sequence were: $t_d = 12$ ms, $\tau = 10$ ms (minimum value attainable), $P = 16$, $M = 12$, FOV = 130 mm, slice thickness of 10 mm with, $\tau_r = 120$ ms and $\beta = 10^\circ$. Choosing $\beta > 20^\circ$ results in poorer T_1 estimation presumably due to the very rapid attainment of steady state and the increased error in β as β increases [102,103]. The repetition time TR was kept fixed at 5000 ms. The matrix size used was $(N_x \times N_y \times N_z) = 128 \times 64 \times 16$ zero-filled to $128 \times 128 \times 16$. The phase encode lines were acquired in 4 segments, thus giving a value of $P = 16$. The choice of P was optimized from a Monte Carlo simulation whereby a one-dimensional image along the phase encode direction was simulated and P was varied between 2 and 32 until a drastic loss in signal was obtained in going from 16 to 32. This was also confirmed experimentally. M was varied between 8, 12, 14 and 16.

T_1 maps were calculated by fitting Eq. (2) to the magnitude signals from each pixel, using a non-linear least-square method, which employs a Levenberg-Marquardt

algorithm (Matlab 6.0, The Matworks Inc. USA), where the fitted parameters were: T_1 and the scaling constant $M_{eq} \exp(-TE/T_2^*)$. A calibration of the transverse B_1 or RF uniformity was found to be quite uniform (a maximum deviation of $\sim 8\%$ was obtained for a 9.5 cm transverse circular diameter). This calibration was done using the method by *Akoka et al* [108]; which makes use of the ratio of stimulated (I_{STE}) and spin (I_{SE}) echo signals. Different I_{STE}/I_{SE} ratio maps for nominal $\beta = 25 - 85^\circ$ in 5° increments were acquired and a fit to the equation $I_{STE}/I_{SE} = \cos(p(\bar{x})\beta)$, with $p(\bar{x})$ providing the spatial B_1 map. There was little or no change in the T_1 estimates using such a correction factor $p(\bar{x})$ on the flip angles, so no subsequent correction was applied in this work.

To validate the performance of this 3-D LL sequence, aqueous gadolinium (Gd-DTPA) samples were prepared with 7 different concentrations varying between about 0.04 mM and 0.70 mM to provide a range of T_1 values from approximately $\sim 300 - 1700$ ms. T_1 values were extracted using the 3-D LL imaging sequence (T_{1_LL}) and compared to T_1 values obtained with a conventional inversion recovery technique (T_{1_IR}) with TI ranging from 100 ms to 10000 ms. Also the T_{1_LL} measurements were compared for four different τ_r values from 10 ms (i.e. conventional ($\tau_r = \tau$)) to $\tau_r = 200$ ms.

3.4 Results and Discussion

Table 3.1 shows a summary of the mean accuracy (defined as $|T_{1_LL} - T_{1_IR}| \times 100 / T_{1_IR}$ for each sample, averaged over all 4 samples) and the range of accuracies for various sequence variables for regions of interest (ROI) of ~ 40 pixels. Table 3.1, also shows the comparison between the T_{1_LL} for the conventional 3-D LL for $\beta = 5^\circ$ ($\tau_r =$

$\tau = 10$ ms) and the T_{1_LL} with $\beta = 10^\circ$ and $\tau_r = 120$ ms. As expected the conventional 3-D LL T_1 measurement accuracy range of 2 to 7.3 % agrees with *Henderson et al* [104] over a similar range of T_1 . The results from the fit for the sequence parameters $M = 16$, $\tau_r = 10$ ms, $\beta = 5^\circ$ (given in Table 3.1 for the conventional method), and a fit from $M = 20$, $\tau_r = 10$ ms, $\beta = 5^\circ$ (thereby making the sampling range approximately the same as that for the parameters $M = 12$, $\tau_r = 120$ ms and $\beta = 10^\circ$) didn't show any significant difference.

Table 3.1: Mean accuracy (defined as $|T_{1_LL} - T_{1_IR}| \times 100 / T_{1_IR}$ for each sample, averaged over all samples) of T_1 estimates using different τ_r , β and M values. The poorer T_1 accuracy for $\beta = 15^\circ$ was due to the 22.5 % poorer accuracy for the T_{1_LL} value compared to the $T_{1_IR} = 1688$ ms vials. Eliminating this value reduces mean accuracy to 3.34 % (range = 2.3 – 4.6 %). The last row gives the accuracy for a conventional 3-D Look-Locker method.

| Sequence Variables | Mean Accuracy (Range) |
|-------------------------------------------------------|------------------------------|
| $M = 14$, $\tau_r = 80$ ms, $\beta = 8^\circ$ | 1.1 % (Range = 0.1 – 2.8 %) |
| $M = 12$, $\tau_r = 120$ ms, $\beta = 10^\circ$ | 1.1 % (Range = 0.2 – 3.1%) |
| $M = 8$, $\tau_r = 200$ ms, $\beta = 15^\circ$ | 6.1 % (Range = 2.3 – 22.5 %) |
| $M = 16$, $\tau_r = \tau = 10$ ms, $\beta = 5^\circ$ | 5.7 % (Range = 2.2 – 7.3 %) |

For example, the fit for a sample using parameter values of $M=16$, $\tau_r = 10$ ms, $\beta = 5^\circ$ gave a T_1 value of 1072 ± 26 ms compared to 1067 ± 33 ms for the parameters $M = 20$, $\tau_r = 10$ ms, $\beta = 5^\circ$. However, the T_1 obtained by the modified 3-D LL method shows an improvement in accuracy ranging from 0.2% to 3.1 % probably due to the improved SNR (Table 3.2) but likely also due to the improved dynamic range sampling of the data as shown in Fig.3.2.

Table 3.2: Relative SNR values for sequence images acquired at approximately the same “effective” inversion time, “ T_{eff} ” for $\beta = 5^\circ$ (the conventional 3-D LL) and $\beta=10^\circ$ ($\tau_r = 120$ ms).

| $\sim T_{\text{eff}}$ (ms) | 90 | 630 | 1170 | 2170 |
|----------------------------|------|------|------|------|
| $\beta = 5^\circ$ | 34.7 | 39.3 | 43.6 | 44.7 |
| $\beta = 10^\circ$ | 52.4 | 56.0 | 60.5 | 59.3 |

Fig. 3.2, illustrates that using $\beta = 10^\circ$ and $\tau_r = \tau = 10$ ms leads to a rapid attainment of

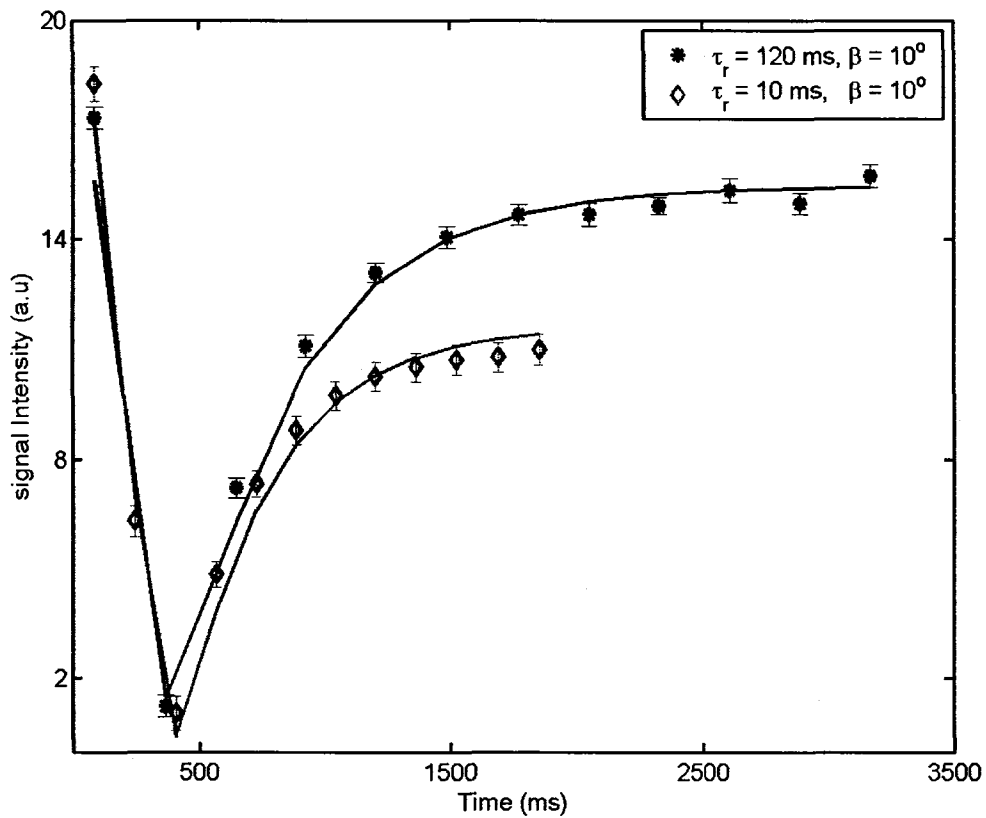


Fig. 3.2. Sample data plots showing the magnetization recovery for $\beta = 10^\circ$ with $\tau_r = \tau = 10$ ms being driven faster to steady state (diamond-shaped data points) compared to the case of $\tau_r = 120$ ms, where the plot shows a less perturbed recovery.

steady state thereby giving poorer T_1 estimates (accuracy up to $\sim 10\%$), compared to the case where $\beta = 10^\circ$ and $\tau_r = 120$ ms which gives an accuracy of $\sim 2.3\%$. Although the extents of sampling for the two curves shown in Fig.3.2 are not the same, this demonstrates the need for a larger recovery time τ_r when using larger tip angles.

Fig. 3.3 shows how the T_1 values for one sample vary as a function of M (the number of recovery samples) for different values of β and τ_r . For $\beta = 15^\circ$ (ROI ~ 40 pixels), the T_1 is consistently overestimated for all values of M , probably due to the poor dynamic range of the data. It is apparent that the choice of optimal β is tied to both the M

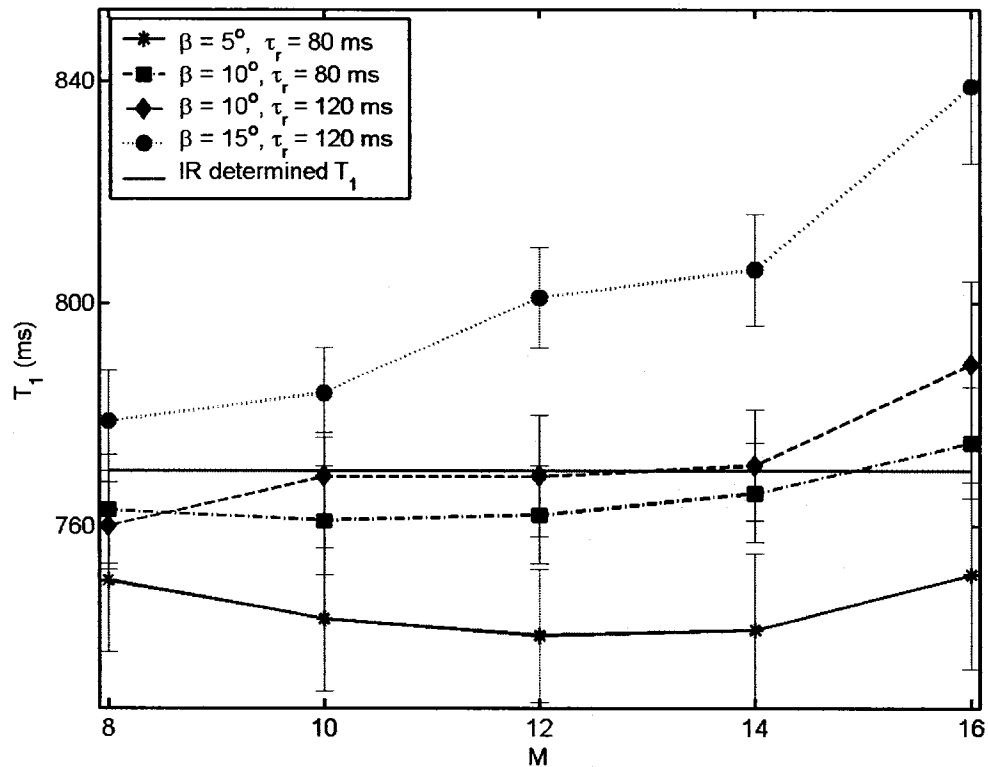


Fig. 3.3. The effect on T_1 estimation of increasing the number of “effective” TI images, M , on a given sample for different tip angles β and intermediate recovery times, τ_r . The horizontal line is the IR estimated T_1 value for this sample (with a T_1 value given by 770 ms).

value as well as the choice of τ_r , a trend which is also observed with the 2-D Look-Locker pulse sequence [102,103] whereby as N (or M) is increased, the optimal tip angle decreases. As the β increases, M must also be reduced to preserve accuracy, however this also reduces the number of samples of the recovery curve (thereby a concomitant reduction in the degrees of freedom), which can lead to unreliable estimates of T_1 . The choice of the τ_r 's for the various flip angles was chosen based on the observation of the data being driven to steady state faster for smaller τ_r values, particularly for $\beta > 8^\circ$.

Figs 3.4(a) and 3.4(b) show the effect of τ_r on the precision and accuracy respectively of a given T_1 as τ_r is increased. Fig.3.4a shows that the precision (given by the percentage standard deviation of the fit of an ROI ~ 40 pixels on the T_1 value for the ROI) gets slightly worse as τ_r is increased. The same trend is shown by the accuracy for $\beta = 5^\circ$ and $\beta = 8^\circ$ in Fig.3.4b. For $\beta = 10^\circ$ and 15° , the accuracy seems to only slightly improve. This is probably because for smaller τ_r (< 120 ms), insufficient magnetization has recovered before the sampling of the recovery curve for the next "effective" TI image occurs. This improvement in accuracy by allowing the magnetization to recover then appears to compensate for any degradation in accuracy resulting from the increase in τ_r .

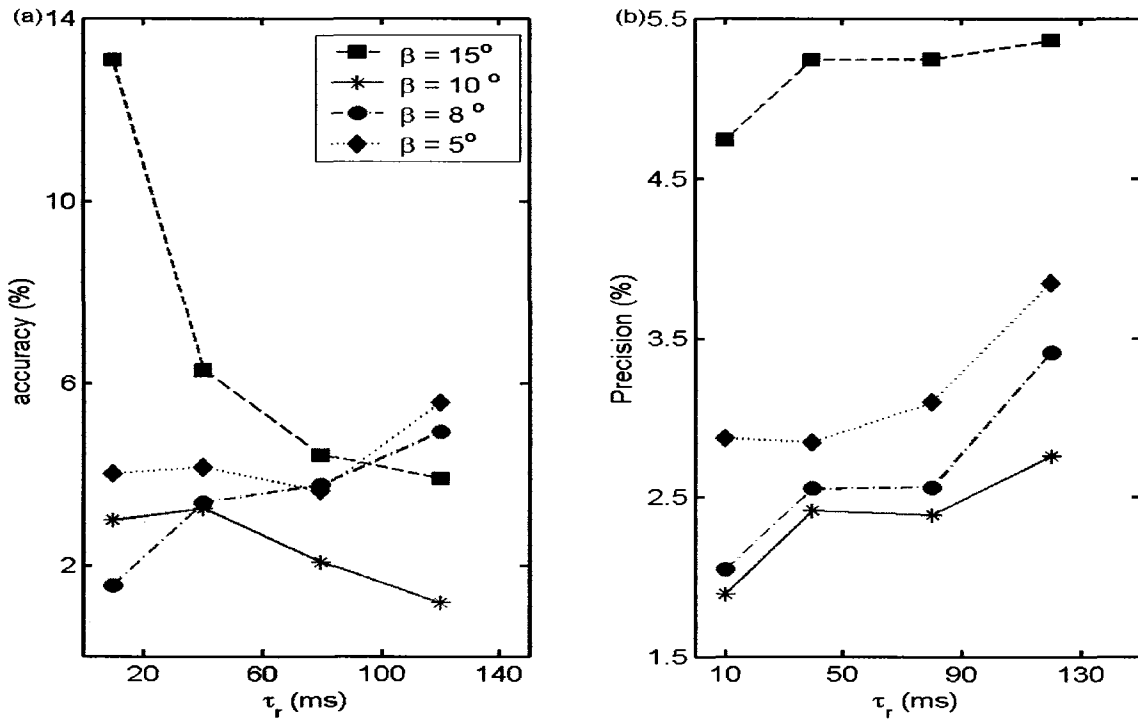


Fig. 3.4. The effect on (a) T_1 accuracy and (b) T_1 precision of increasing the intermediate recovery time variable, τ_r , for different tip angles β with M set at 14.

Fig.3.5, shows T_{1_LL} plotted versus T_{1_IR} as well as the best fit linear regression giving a slope of 1.01 ± 0.01 , an intercept of 2.93 ± 9.41 and an $r^2 = 0.9986$. The data points represent the mean of four calibration vials and the error bars are the resultant standard deviation. These measurements were made with $\beta = 10^\circ$, $M = 12$, $P = 16$, and $\tau_r = 120$ ms. Overall, the T_{1_LL} values showed good accuracy and precision compared the T_{1_IR} values.

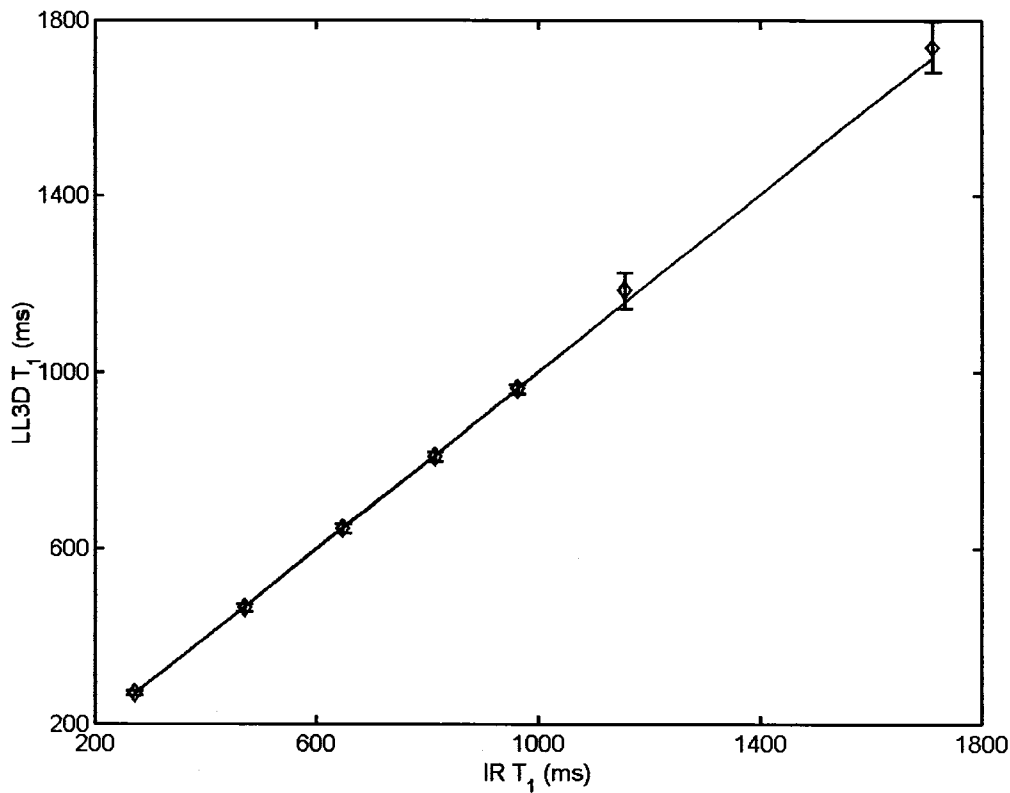
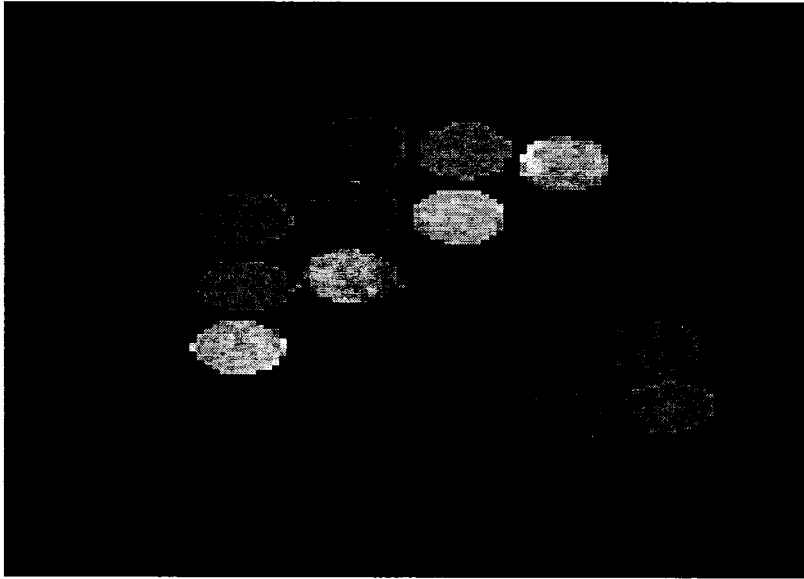


Fig. 3.5. The modified 3-D LL estimated T_1 values compared with inversion recovery determined T_1 values. The straight line is the linear least-square fit to the data. The data points are the mean of four calibration vials weighted by the errors on the fitted T_1 and the error bars are the resultant standard deviation. The 3-D LL sequence variables were, $\beta = 10^\circ$, $\tau_r = 120$ ms, $M = 12$.

Measurements with other parameters such as $\beta = 15^\circ$, $M = 12$, $P = 16$, and $\tau_r = 120$ ms provided fits with much larger intercepts (-19.59 ± 10.44 ms) and worse slopes (0.94 ± 0.07) with an $r^2 = 0.9976$. Figs. 3.6 (a) and 3.6(b) show sample T_1 maps calculated using the conventional method and using the method described in this work respectively. Fig.3.6 (b) was acquired using the parameters $\beta = 10^\circ$, $M = 12$, $P = 16$, and $\tau_r = 120$ ms and is less noisy compared to Fig.3.6 (a).

(a)



(b)

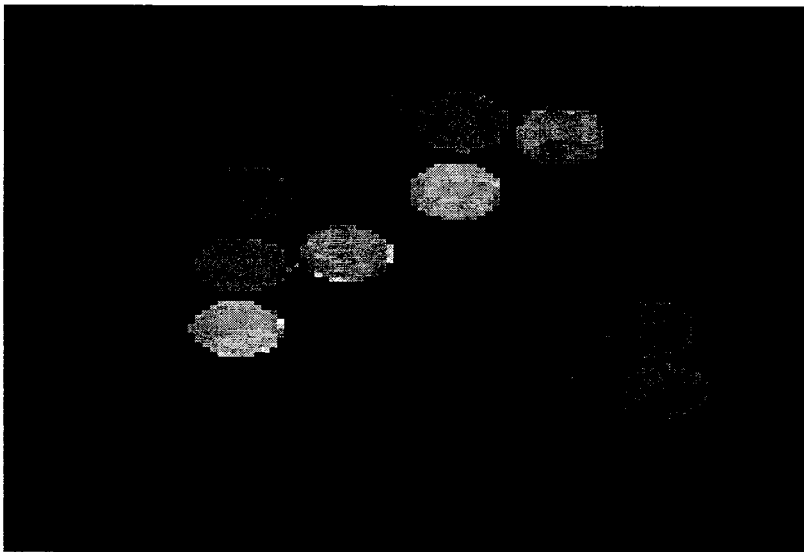


Fig. 3.6. Sample T_1 maps for the conventional 3-D LL with parameters $M = 16$, $\tau_r = 10$ ms, $\beta = 5^\circ$ (6a) and for the suggested method with parameters $M = 16$, $\tau_r = 120$ ms, $\beta = 10^\circ$ (6b).

This modified 3-D LL sequence permitted the acquisition of a $128 \times 64 \times 16$ data matrix in less than 6 minutes with a T_1 accuracy of within 3 % (for the worst case within

the T_1 range investigated). This work indicates that for the range of T_1 values used here, a suggested choice of measurement parameters would be $\tau = 10$ ms, $\tau_r = 120$ ms, $\beta = 10^\circ$, $M = 12$ to give a mean accuracy within 3 %. For larger tip angles such as 20° it would be advisable to reduce P from 16 to about 8 with a concomitant increase in acquisition time. Although the conventional 3-D LL ($\tau = \tau_r$) is marginally faster (~ 15 %) the loss in accuracy is significant and suggests that the small time penalty introduced by the additional delay time, τ_r , is justified.

It is worth noting that this method is still applicable to the 2-D LL imaging method and would be expected to provide similar improvements in accuracy with even less time penalty. The interpretation of the parameters such as M and P (with M being the number of “effective” inversion time TI_{eff} images instead of N as in a conventional 2-D LL sequence) used in a 2-D implementation would be expected to be the same as that presented here for the 3-D case.

3.5 Conclusion

We have described and characterized a 3-D LL imaging sequence which permits the use of larger tip angles ($> 5^\circ$) by the introduction of an additional recovery time delay variable τ_r while still keeping the inter-pulse timing for pulses within each recovery time sample small (≤ 10 ms) and thereby providing more accurate and precise T_1 estimates with only marginal (15 %) increase (compared to the conventional 3-D LL) in the total measurement time. For an acquisition matrix of $128 \times 64 \times 16$ with the sequence parameters of $t_d = 12$ ms, $\tau = 10$ ms, $\tau_r = 120$ ms, $\beta = 10^\circ$, $P = 16$ and $M = 12$, a mean

accuracy in the T_1 estimation within 3 % is obtained for T_1 values ranging from about 300 ms to about 1700 ms within a six minute measurement time.

Chapter 4

3-D Look-Locker Imaging for T_1 Gel Dosimetry: Effect of k-space Data Acquisition

4.1 Introduction

The Look-Locker imaging scheme has been suggested as a possible tool for gel dosimetry (especially with Fricke gel dosimeters which are T_1 radiation sensitive) due to its speed of data acquisition combined with its well established accuracy and efficiency of estimating T_{1s} [100-106, 109,110]. Speed is essential since these gel dosimeters suffer the problem of spatial diffusion of radiation-induced ferric ions (from ferrous ions) and auto-oxidation (of ferrous to ferric ions). Due to its speed of data acquisition, this method faces a problem similar to that faced in fast spin echo imaging [111], in that the main drawback associated with the 3-D Look-Locker (3-D LL) imaging method is that the acquisition of k-space is segmented and within each of these segments the magnetization is evolving (recovering in this case) during the acquisition of this k-space segment of the image. This thereby gives a point spread function (PSF) effect in the phase encode direction when the data is Fourier transformed into object (or image) space, which can result in either some edge blurring or enhancement in the image.

In this chapter the effect of different PSF from four different k-space acquisition schemes on image profiles is explored by simulations such as loss or enhancement in

signals especially for small size objects. The range of T_1 s examined included a clinically-relevant range expected in tissue (300 ms – 1800 ms) which also covers the range of T_1 commonly found in T_1 or Fricke-based gel dosimeters. A suggestion is then made as to a possible k-space acquisition method for optimal gel dosimetry (i.e. Fricke gel dosimeters). Using the PVA-Fricke Hydrogel as an example, an estimate of the spatial resolution loss due to time PSF effect is made. The dose accuracy and dose resolution (a defining quality factor for gel dosimeters that evaluates the dose uncertainty in images) of this method for gel dosimetry is also estimated experimentally for the T_1 range of doses between 0 and 20 Gy.

4.2 Theory

In the implementation of the fast 3-D LL sequence shown in Fig. 3.1, a non-slice selective inversion pulse ($\alpha = \pi$) is used to completely invert the longitudinal magnetization prior to the acquisition of each segment of k_y space for a fixed k_z value. After the inversion pulse, a series or group P , of small flip angle slab selective read-out pulses, β , separated by a time interval, τ , are used to rapidly and repeatedly sample the recovery of the longitudinal magnetization to fill a given k-space segment. A gradient echo is used to sample k_x space following each β pulse for each k_y phase-encoding step in the given segment (the number of k_y lines, P , per segment is typically 16, requiring N_y/P shots to fill an $N_x \times N_y$ image matrix). Any residual transverse magnetization, which might interfere with the signal from the next β pulse, is completely spoiled after each gradient echo using spoiler gradients.

The 3-D LL imaging sequence equation has been defined by *Henderson et al* [104] and modified by *Nkongchu* and *Santyr* [106] (see Chapter 3) to give a more general description of the magnetization evolution during image acquisition. The equation for the longitudinal magnetization for a given voxel after the n^{th} β read-out pulse following a 3-D LL image acquisition is given by [106]:

$$M_n = M_{eq} \left[F + (Q - F) \{ \cos(\beta) E_\tau \}^{n-m} \{ \cos(\beta) E_{\tau_r} \}^{m-1} \right] \quad (4.1)$$

where M_{eq} is the equilibrium magnetization and F , Q , E_τ and E_{τ_r} are all functions of T_1 , P , β , and inter-pulse timings, τ and τ_r , defined in Chapter 3. F is defined to be the longitudinal magnetization as the number of β read-out pulses approaches infinity and Q is the ratio of the longitudinal magnetization just before the β_1 pulse and the equilibrium magnetization M_{eq} . m is the number of the inversion time (TI) image acquired and n is the β pulse used to acquire a given y k-space line. Since there is k-space modulation during image acquisition for this imaging sequence, one can apply a derivation for the theoretical PSF effect on the k-space signal acquisition in a 3-D Look-Locker imaging sequence similar to that applied by *Constable et al* [111] for the fast spin-echo imaging (FSE) sequence.

Following the derivation of *Constable et al* [111], the total k-space signal, $S(k_x, k_y, k_z)$, is given by the sum of k-space signal for all the constituent tissues being imaged for that particular location or voxel and is given by [111,112]:

$$S(k_x, k_y, k_z) = \sum_{r=1}^N S_r(k_x, k_y, k_z) \quad (4.2)$$

where the k-space signal for the r^{th} tissue is defined to be:

$$S_r(k_x, k_y, k_z) = A_r S_r'(k_x, k_y, k_z) \quad (4.3)$$

In Eqn.4.3, A_r is defined to be a function of the tissue characteristics given mainly by the TI image number, m , the tip angle β and the tip angle number n used to acquire a given phase encode line k_y , the inter-pulse spacing τ , the number of k-space lines acquired per segment, P , the tissue dependent parameters T_1 , and T_2 . $S_r'(k_x, k_y, k_z)$ is simply a function of the tissue's geometry. In an ideal object, A_r should be independent of k_x , k_y and k_z , for example in a simple Look-Locker image. Taking the inverse Fourier transform of Eqn.4.3 which would be the scenario for a simple 2-D LL image, one can then obtain the image for the r^{th} tissue:

$$f_r^{LL} = FT^{-1} \left\{ A_r S_r'(k_x, k_y, k_z) \right\} \quad (4.4)$$

For the 3-D LL image acquisition method, which involves a modulation of k-space in the phase encode direction (k_y) during acquisition, A_r becomes a function of k_y , that is $A_r(k_y)$ and the image for tissue r acquired using the 3-D Look-Locker method becomes:

$$\begin{aligned} f_r^{LL3D} &= FT^{-1} \left\{ A_r(k_y) S_r'(k_x, k_y, k_z) \right\} \\ &= FT^{-1} \left\{ A_r'(k_y) A_r(k_y = 0) S_r'(k_x, k_y, k_z) \right\} \end{aligned} \quad (4.5)$$

where $A_r'(k_y) = \frac{A_r(k_y)}{A_r(k_y = 0)}$

Applying the Fourier Convolution theorem (the product of two functions is equal to the convolution of their individual Fourier transforms) to Eqn.4.5, we can observe the effect of the PSF on the 3-D LL image given by:

$$f_r^{LL3D} = FT^{-1} \left\{ A_r'(k_y) \right\} * FT^{-1} \left\{ A_r(k_y = 0) S_r'(k_x, k_y, k_z) \right\}$$

$$= P_r(y) * f_r(x, y) \quad (4.6)$$

where $P_r(y)$ defines the point spread function for the r^{th} tissue in the y -direction due to k -space modulation during image acquisition. This PSF, $p_r(y)$, would be defined in the 3-D LL case for the r^{th} tissue as:

$$P_r(y) = FT^{-1} \left\{ M_n'(k_y) \right\}$$

$$P_r(y) = FT^{-1} \left\{ \frac{1}{M_n(k_y = 0)} \left[F + (Q - F) [\cos(\beta) E_{\tau}]^{n(k_y) - m} [\cos(\beta) E_{\tau_r}]^{m-1} \right] \right\} \quad (4.7)$$

4.3 Method & Simulation

Four different orders of acquiring k -space in a 3-D LL acquisition were investigated using simulation. Fig. 4.1 illustrates four cases of k -space trajectories and will simply be referred to as orders 1 to order 4 as shown in Fig. 4.1a to Fig. 4.1b respectively. In acquisition order 1, the k -space was acquired beginning from the centre of k -space towards the edges of the k -space while order 2 was done in a similar way but with the acquisition done from the edges towards the centre of k -space. Order 3 was done linearly with acquisition done from one end of k -space, $-k_{y\text{max}}$ (where $k_{y\text{max}} = N_y/2$ is maximum y k -space line) to the other end ($+k_{y\text{max}}$) all in one direction for all the number of k -space segments or shots. Order 4 was similar to order 3 except that k -space was acquired from both directions (half of the shots are done from $-k_{y\text{max}}$ to $+k_{y\text{max}}$ and the other half from $+k_{y\text{max}}$ to $-k_{y\text{max}}$). Interleaving of the k -space line between the number of shots needed to fill the k -space was done for all these orders. The effect of these acquisition schemes on the loss of signal from small objects of a few pixels in

comparison to larger objects was investigated. This signal lost was also investigated as a function of various T_1 values.

To study the blurring effect on the object signal profile as a function of the number of k-space lines acquired for a given segment, P , the shape or width of the PSF created by the four different k-space acquisition orders was assessed.

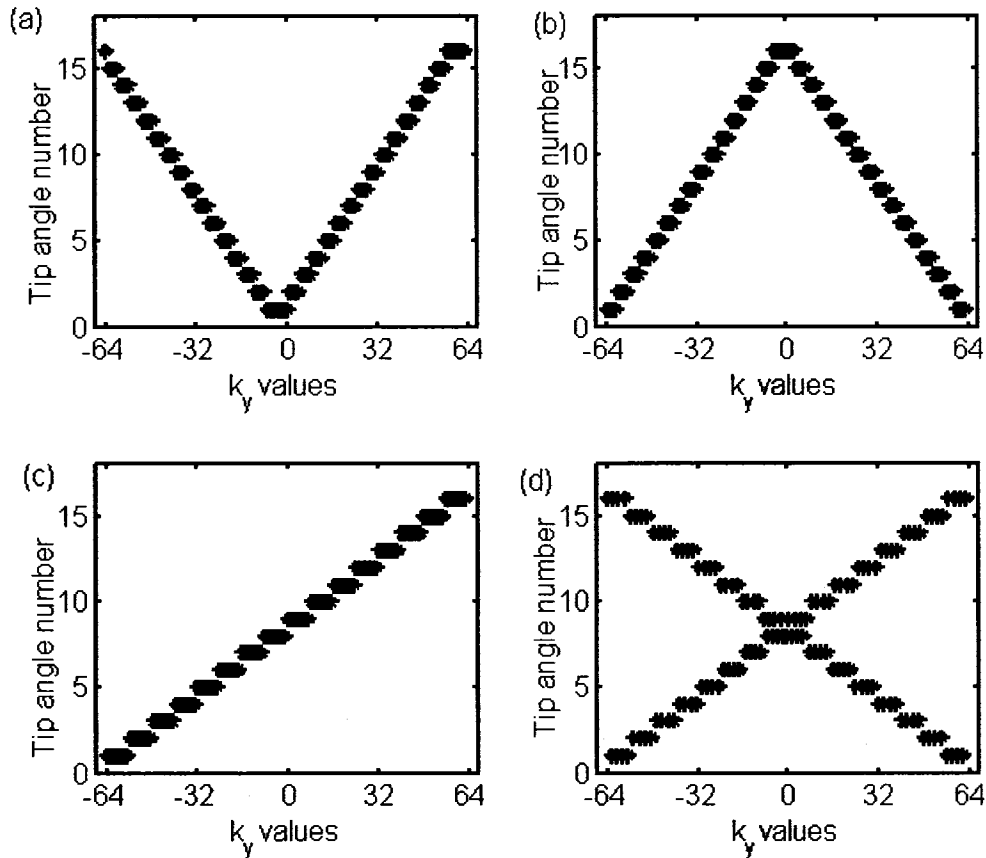


Fig. (4.1): Different k-space acquisition orders for a value of $P = 16$: (a) order 1, (b) order 2, (c) order 3 and (d) order 4. Note that for each plot there are 8 k_y line values having the same tip angle number because the 128 k_y lines were acquired in eight ($= 128/P$) shots with interleaving of k_y lines.

The simulations of the signal profile due to the modulation of k_y -space from the 3-D Look-Locker signal followed the flow chart shown in Fig. 4.2 using $\beta = 10$ and interpulse timing of 10 ms with a repetition time $TR = 4000$ ms. This involved Fourier

transforming a synthetic one-dimensional (1-D) object profile (from image space) in the phase encode direction into Fourier or k-space. The k-space profile of the 1D object was then T_1 weighted using the 3-D LL acquisition method. This T_1 -weighted profile was then inverse Fourier transformed to obtain a representative 3-D LL acquired profile of the object. For a particular k-space acquisition order this procedure was repeated for a set of 14 1-D profiles with an inter-echo timing of 10 ms for the desired value of P to produce

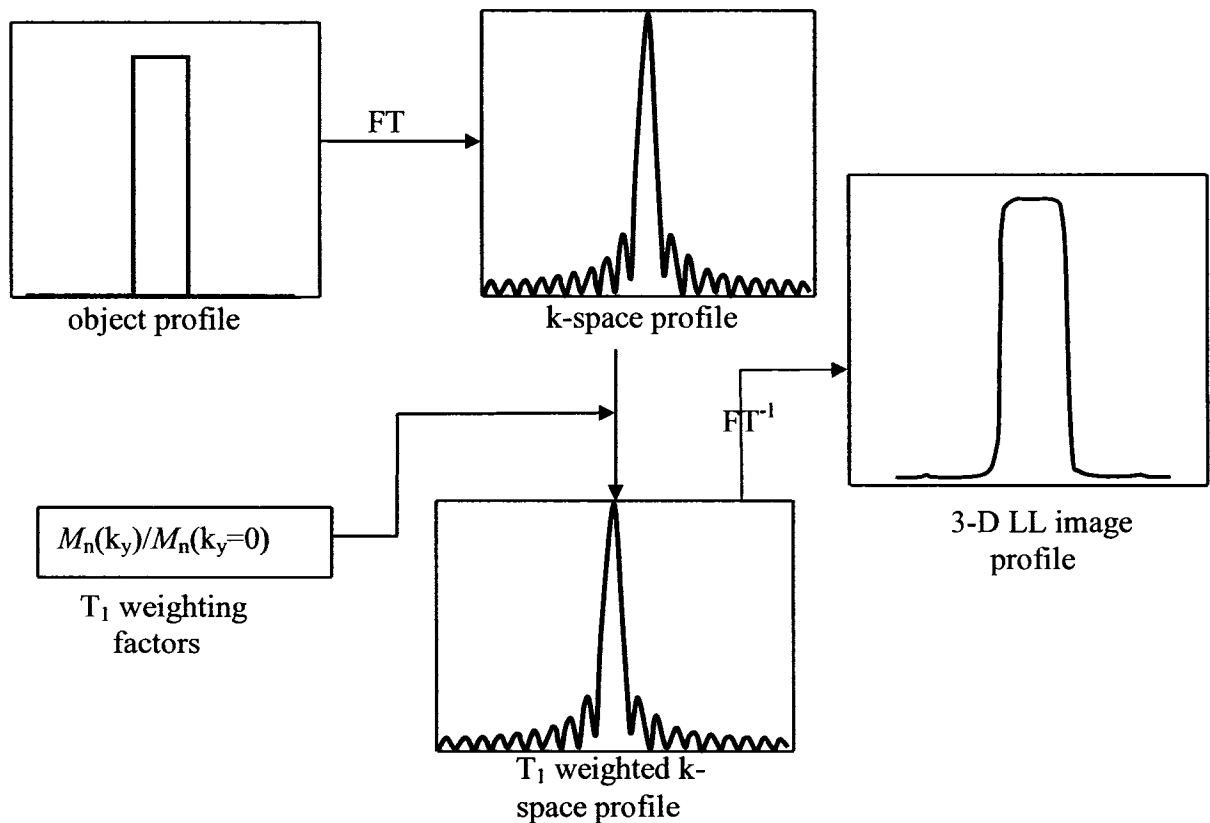


Fig. 4.2: Flow chart of simulation scheme used.

14 different TI images. Though the PSF resolution loss would be defined by the full-width at half maximum (FWHM), the full width at tenth maximum (FWTM) was one of the parameters used to quantify the effect of the smearing of neighbouring pixels as a

result of the k_y -space modulation by the LL3-D sequence due the fact that the PSF for most of the acquisition orders studied where much broader at the tail.

Experimental Signal Profiles

Using a cylindrical phantom, images were acquired using the four different orders to acquire k -space from which 1-D profiles in the phase encode direction were obtained. The 3-D LL image acquisition used the following variables: $P = 16$, $\beta = 10^\circ$, $\tau = 10$ ms, $\tau_r = 120$ ms, 16 slices, $TR = 4$ s, 2 averages, and a matrix size of 128×128 . These 1-D profiles should closely mimick the simulated signal profile along the phase encode directions for all 4 orders. These experimental 1-D profiles were taken as a validation of the simulations permitting the study of the PSF effects on images acquired using the 3-D LL technique.

Spatial Resolution loss

A simple estimation of the effect of k_y -space modulation on the 3-D LL spatial resolution was done by taking into consideration the effective resolution which accounts for: (i) the intrinsic resolution for MR imaging commonly used for gel dosimetry, $\sigma_{img} = 1$ mm, (ii) σ_{diff} , the resolution loss due to the diffusion of ferric ions in Fricke-based gel dosimeters and (iii) σ_{PSF} , the resolution loss due to the PSF effect (simulated) from the k_y -space modulation using 3-D LL given by the full-width at half maximum (FWHM). The resolution loss from (ii) can be estimated from the relationship [113]:

$$\sigma_{diff} = \sqrt{2DT_{acq}} \quad (4.8)$$

where D is the diffusion coefficient of ferric ions in a gel dosimeter, which for the PVA Fricke hydrogel was estimated to be ~ 0.14 mm²hr⁻¹ [15,114]. T_{acq} is the total imaging or

acquisition time. For $T_{acq} = 0.57$ hrs and a 3-D LL acquisition using a value of $P = 8$, $\beta = 20^\circ$, 16 slices, $TR = 4s$, and a matrix size of 256×256 , σ_{diff} was calculated to be 0.399 mm. Note that in 3-D LL, the total imaging or acquisition time is given by:

$$T_{acq} = (N_y/P) * N_{sl} * TR * N_{ex} \quad (4.9)$$

where N_y is the number of phase encode lines acquired, N_{sl} is the number of slices or number of phase encodes in the slice selection direction, P is the number of phase encode lines within a given k_y -space segment, TR the repetition time and N_{ex} is the number of averages. Combining (i), (ii) and (iii) in quadrature, the effective resolution is given by:

$$\sigma_{eff} = \sqrt{\sigma_{img}^2 + \sigma_{diff}^2 + \sigma_{PSF}^2} \quad (4.10)$$

Eqn.4.10 was used to calculate the loss of spatial resolution using the 3-D LL method.

T_1 Accuracy and Dose Resolution

T_1 Accuracy: To estimate the T_1 of the samples, the raw images were fitted for T_1 using Eqn.4.1 for experimental images acquired using k_y -space ordering “order 1” and “order 4” (order 2 images have very low SNR as shown in Section 4.4 and order 3 gave the same accuracy as order 4). In this process, n is defined as the tip angle pulse that is assigned to the centre of k -space. The tip angle pulse number was calculated using the following relationship:

$$n = P(m-1) + n_c \quad (4.11)$$

where $m = 1, 2, \dots, M$ and M is the number of inversion time images and P is the number of phase encode (k_y) lines acquired per segment of an m image. For order 1, $n_c = 1$, and for order 4, $n_c = 4$. The accuracy of the T_1 values estimated from data acquired using orders 1 and 4 were compared to the inversion recovery estimated T_1 values, which was

considered the gold standard. The optimal method of filling k-space in terms of accuracy was then used to calculate the dose resolution (below) for the PVA-Fricke hydrogel dosimeter [15,114]. The 3-D LL images were acquired using the following parameters $\beta = 20^\circ$, $\tau = 10$ ms, $\tau_r = 120$ ms, $P = 8$, $M = 10$, TR= 4s, 2 averages (according to chapter 3) and a spatial resolution of approximately $1 \times 1 \times 3$ mm³ from a $128 \times 128 \times 16$ matrix.

Dose Resolution A dose resolution, D_Δ^P , is defined as the minimal separation between two absorbed doses such that they may be distinguished with a given level of confidence [51,]. Following the derivation in *Baldock et al* [51], one can obtain a general formula for the dose resolution of a given gel dosimeter. The standard deviation of the sampling distribution resulting from the difference of the two dose populations centred at dose D_1 and D_2 is given by [51]:

$$\sigma_{diff} = \sqrt{\sigma_{D_1}^2 + \sigma_{D_2}^2} \quad (4.12)$$

The probability condition P , that the difference between the values D_1 and D_2 is greater than zero is given by $P\left[|D_1 - D_2| = D_\Delta^P > 0\right] = \alpha$, where the level of confidence p is then given by $p = 1-\alpha$. For a specific level of confidence p , the dose resolution can be stated as:

$$D_\Delta^P = k_p \sigma_{diff} \quad (4.13)$$

where k_p is the coverage factor and is given by the t-distribution for the experimental degrees of freedom. For example, for a 95% level of confidence and assuming Gaussian distributed data points, one has $k_{95\%} = 1.96$. For two neighbouring dose distributions,

Baldock et al [51], assumed that a good approximation of the error on the dose, σ_D , is given by $\sigma_D = \sigma_{D1} = \sigma_{D2}$, thus the dose resolution becomes [51]:

$$D_{\Delta}^P = k_p \sqrt{2} \sigma_D \quad (4.14)$$

Assuming a linear relationship between dose D and $R_1 = \delta D + R_{10}$, within a certain dose interval (for the case of PVA Fricke Hydrogel and cryogel – linearity has been demonstrated up to 20 Gys [51]), the dose resolution [56, 115] can be written as a function of the standard deviation in R_1 , similar to the case of R_2 for polymer gel dosimeters [56, 115]:

$$D_{\Delta}^P = k_p \sqrt{2} \frac{\sigma_{R_1}}{\delta} \quad (4.15)$$

where δ is the dose response of the gel dosimeter. For the case of the Fricke Hydrogel, this value has been measured at a magnetic field strength of 1.89 T to be $0.033 \pm 0.003 \text{ s}^{-1} \text{ Gy}^{-1}$ [114]. Eqn.4.15 indicates that the dose resolution is determined by the dose response (or dose sensitivity δ) and the signal-to-noise ratio (SNR) which appears in Eqn 4.15 as σ_{R_1} .

To obtain an estimate of the T_1 accuracy, precision and the dose resolution expected for PVA-Fricke hydrogels, aqueous gadolinium samples were prepared with T_1 values spanning the range expected for PVA-Fricke hydrogels irradiated up to doses of 20 Gy. The standard deviation in R_1 was then estimated which in conjunction with the linear relationship between dose and R_1 ($R_1 = 0.033D + 1.007 \text{ (s}^{-1})$), permitted calculation of an estimate of the PVA-Fricke Hydrogel dose resolution using Eqn. 4.15. The images from which the T_1 values were estimated were acquired using the following

parameters $\beta = 20^\circ$, $\tau = 10$ ms, $\tau_r = 120$ ms, $P = 8$, $M = 10$, TR= 4s, 2 averages and a spatial resolution of approximately $1 \times 1 \times 3$ mm³ from a $128 \times 128 \times 16$ matrix.

4.4 Results and Discussion

As indicated in *Constable* and *Gore* [111] for fast spin echo (FSE) imaging, the MR data for the 3-D LL scheme is effectively multiplied by a modulation function prior to the signal being picked up by the receiver. This modulation transfer function (MTF) happens to be not only a function of the imaging scheme but also a function of the sample (or tissue) (T_1, T_2 , β amongst others) in question since the PSF (given in Eqn 4.7) is simply a Fourier transform of the MTF. Fig. 4.3 shows the corresponding PSFs for the various k_y -space acquisition orders given in Fig. 4.2. When the k_y -space filling trajectories for the orders shown in Fig. 4.2 are weighted by the appropriate T_1 signal ratio, their respective MTFs can be calculated. Thus from these MTFs, different regions of k_y -space will be enhanced depending on the effective β , that is the β number assigned to the centre of k_y -space. The maximum blurring is observed for imaging using order 1 and order 2 will show the most edge enhancement of image due to the assignment of the earlier tip angles to the high spatial frequencies. From Fig. 4.3, the PSF width for a sample (or tissue) of $T_1=1800$ ms is considerably less than that with $T_1 = 300$ ms as expected. The smearing effect between neighbouring pixels is also reduced for longer T_1 values.

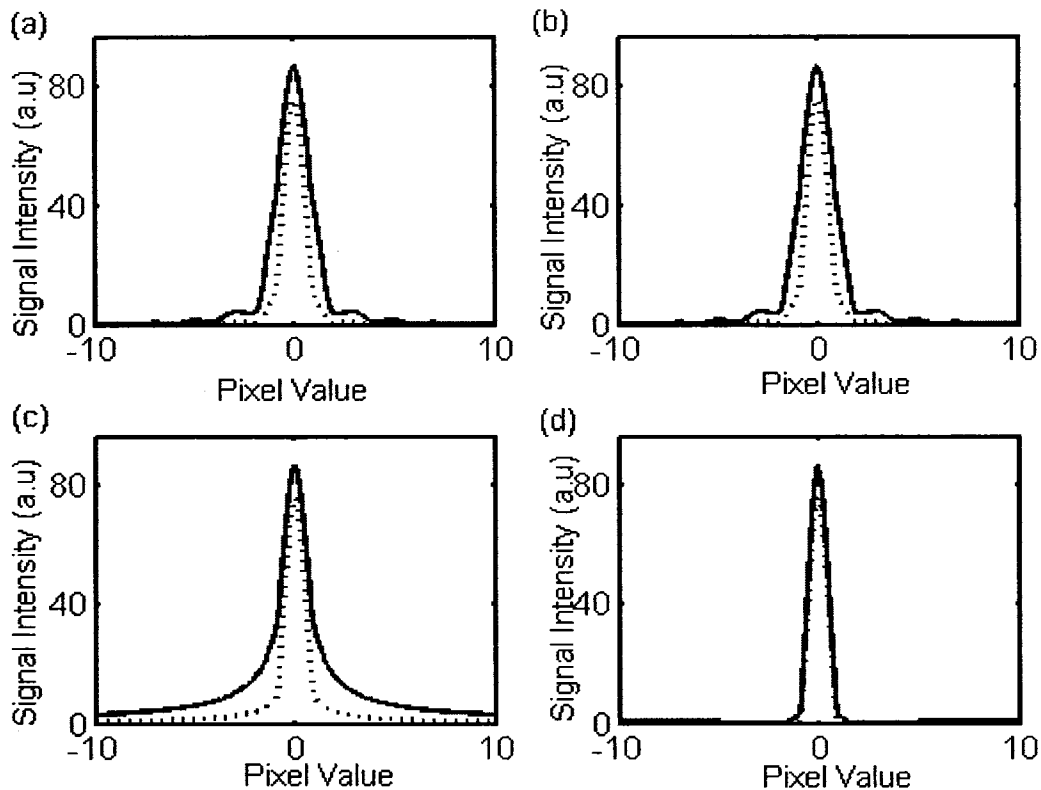


Fig. 4.3: Simulated PSFs for (a) order 1, (b) order 2, (c) order 3, and (d) order 4 for two T_1 values. The dotted line is for a sample (or tissue) T_1 of 1800 ms and the solid line is for a sample (or tissue) $T_1 = 300$ ms for a value of $P = 16$.

The PSF for order 3 and $T_1 = 300$ ms, shows a smearing effect across many more pixels compared to the other orders. For order 4, the PSF for both T_1 values are basically the same with a smaller PSF width. To further investigate the effect of P on the PSF including the broadening of PSF at the base for order 3, a FWTM was calculated for other P values to see the change in the PSFs. This change in PSF width is shown in Fig. 4.4(a) and (b) for $T_1 = 300$ ms and $T_1 = 1800$ ms respectively. The change in FWTM is approximately the same for order 1 and order 2.

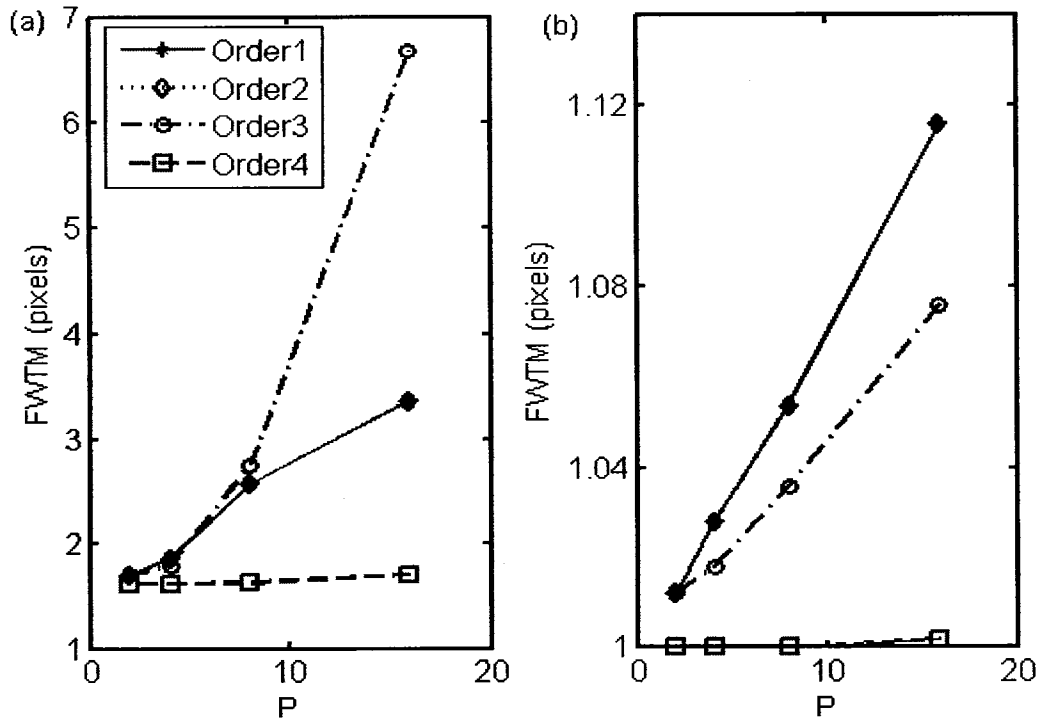


Fig 4.4: Simulated FWTM of the PSF with respect to the number of k_y -space lines acquired within a k_y -space segment for a tissue of (a) $T_1 = 300$ ms and (b) $T_1 = 1800$ ms. Plots for FWTM using order 1 and 2 are identical to each other.

For short T_1 , the FWTM gets worse for the k_y -space acquisition order 3 but outperforms order 1 and 2 for $T_1 = 1800$ ms. From the increase in FWTM with P , this would suggest that the loss of object contrast gets worse with increasing the number of k_y -space lines per segment P , used for orders 1 to 3. But acquisition using order 4 has very little or no dependence on the value of P used and thus outperforms the other three orders.

Effect of interpulse timing τ and tip angle β on PSF

Fig. 4.5(a) shows the effect of the change in inter-pulse timing, τ , on the FWTM for the different orders. This figure shows that using k_y -space acquisition orders 1 to 3, the smallest inter-pulse timing (gradient performance constraints permitted) should be used to limit the PSF effect of the k_y -space modulation acquisition on the object being

imaged. But it can be seen that k_y -space acquisition using order 4 has very little dependence on this inter-pulse timing, τ , (when compared to the other 3 methods) and despite showing the same trend as orders 1 to 3 as shown in Fig. 4.5(b) it has an overall FWTM much smaller than the other acquisition orders.

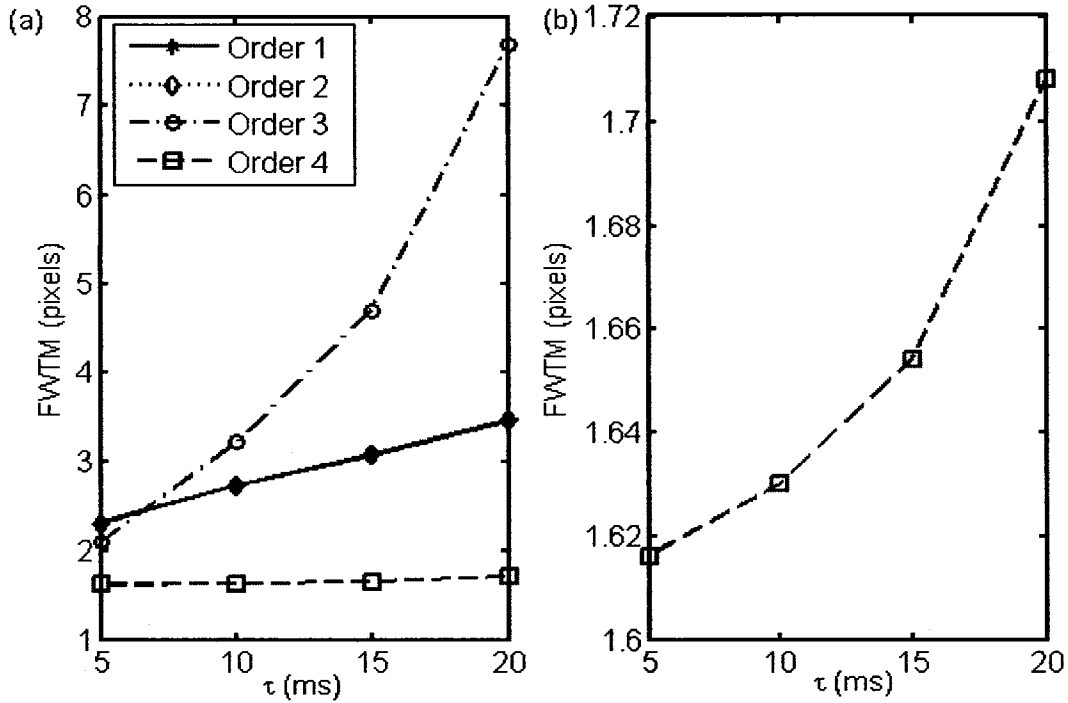


Fig. 4.5: (a) FWTM of the PSFs of a given T_1 value as a function of inter-pulse spacing τ for the 4 different k_y -space filling orders. (b) Enlargement of k_y -space acquisition order 4 from (a) shown separately. The value of P here was set to 16 and a tip angle of 10° . Note that the lines were added as a visual guidance.

Fig. 4.6a shows the change in FWTM of the PSF as a function of the tip angle, β , used for four values of P for sample T_1 of 300 ms. For all four orders, the FWTM gets worse for increasing β and better as one decreases the value of P from 16 (Fig. 4.6a) to 2 (Fig. 4.6d). For $P = 16$, the worst smearing is shown by order 3 and best by order 4. For orders 1, 2, 3 the FWTM gets worse with increasing tip angle for all values of P . However, order 4 shows this trend only for $P = 16$ while staying relatively constant for

other values of P . For $P = 2$, the orders 1,2, and 3 all give similar values but order 4 still shows less smearing effects indicated by its lower FWTM values. This same trend was shown with a simulated $T_1 = 1800$ ms but with much smaller FWTM values (data not shown). The maximum FWTM for order 4 was 1.05 pixels for a tip angle of 20° and $P = 16$ for $T_1 = 1800$ ms, 1.5 pixels for order 3 and, 1.7 pixels for order 1 and 2. These factors would

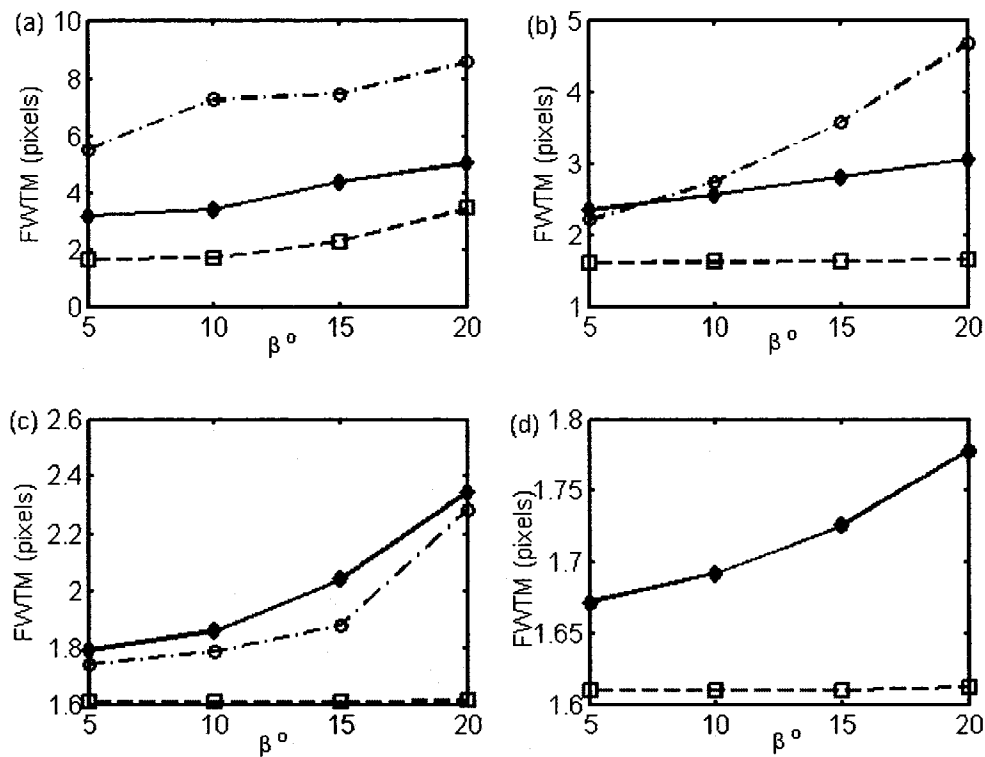


Fig. 4.6: Simulated FWTM of the PSF as the tip angle is increased from 5° to 20° for (a) $P = 16$, (b) $P = 8$, (c) $P = 4$, (d) $P = 2$ for a tissue of $T_1 = 300$ ms. The simulated data points plotted with diamond are for orders 1 and 2, those with circles are for order 3, and the square points for order 4.

suggest order 4 as the best way to acquire data for the purpose of imaging in gel dosimetry where an attempt to have areas with high dose gradients aligned with the read

encode direction might not be possible. This would limit the loss of information in the area of high dose gradients and/or possible hot spots present in the dosimeter.

Effect of k-space acquisition on Signal Profile

Fig. 4.7 shows the effect on object signal profile of the four different orders of acquiring k-space described earlier. These profiles represent an $N_y = 128$ with a value of $P = 16$, for the number of lines acquired per k-space segment. These figures also show that there is either loss of signal or enhancement in signal at the edges of the object being

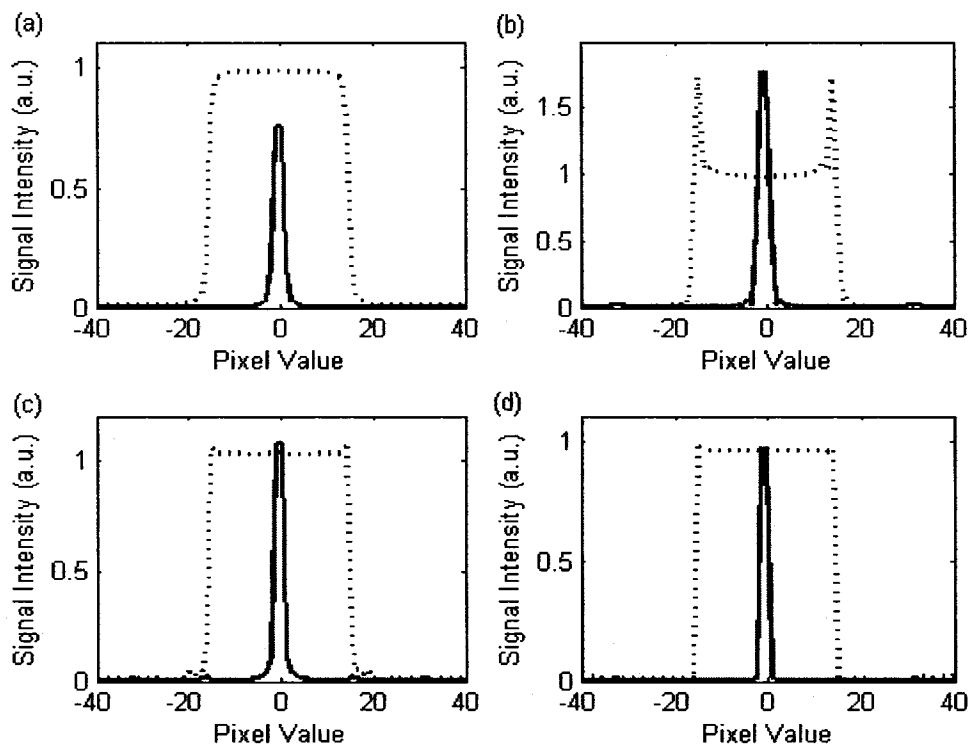


Fig. 4.7: Simulated object signal profile (for 2 and 30-pixel object for 128 k-space lines both with $T_1 = 600$ ms) using the four different orders of acquiring k-space data, with (a) using order 1, (b) order 2, (c) order 3 and (d) order 4. The solid line style is for the 2 pixel object while the dotted line is for the 30-pixel object.

imaged depending on the k-space trajectory. The profiles were normalized to the value of the 30-pixel object at the centre of k_y -space. For the acquisition using order 1 (central k_y -space acquisition) shown in Fig. 4.7(a), there is an apparent loss of signal or blurring

effect at the edges and also a spread of the signal beyond the image boundary (i.e. 'smearing'). Fig. 4.7(a) also shows that there is a loss of signal of a 2-pixel object in comparison to the 30-pixel object, suggesting that a data acquisition scheme using order 1 might lead to a possible loss of small objects if they are embedded in (or in the vicinity of) a larger pixel object. Fig. 4.7(b) is the profile acquired using k-space acquisition order 2. There is a signal enhancement at the image boundaries using order 2 for the 30-pixel object. There is enhanced signal for the 2-pixel object in comparison to the 30 pixel object, meaning small (i.e. 2-pixel) objects are more likely to be seen for an image acquired using this k-space acquisition scheme. Fig. 4.7(c) shows the profile acquired using order 3 (linear k_y -space filling). It has good edge definition when compared to the original simulated rectangular object with just a slight signal enhancement at the edges of the image profile. The 2-pixel object in Fig. 4.7(c) does show some signal enhancement and would mostly likely be seen in an image acquired using this order. Looking at the image profile acquired using order 4 shown in Fig. 4.7(d), it shows a similar signal behaviour to that of order 3 with the 2 pixel object also still visible. The simulated image using order 4 shows a much better profile definition in comparison to the original object. In Figs. 4.7(a)-(c) there is some spread of the signal beyond the boundaries of the image, but Fig. 4.7(d) shows much less spread beyond its boundaries thus implying it would be advantageous to use this scheme for an acquisition where loss of small object signal might be a problem. The profiles in Fig. 4.7 are all for a given T_1 of 600 ms.

Signal Loss with T_1 and Object Width

Fig. 4.8 shows the results of the study of the signal loss or enhancement for the T_1 values within a relevant clinical range (300 ms – 1800 ms, within which the T_1 -based Fricke gel dosimeter lies), for a 2-pixel object in comparison to a 30-pixel object due to the PSF. The results shown in Fig. 4.8 are for the mean of the signal from 5 pixels around

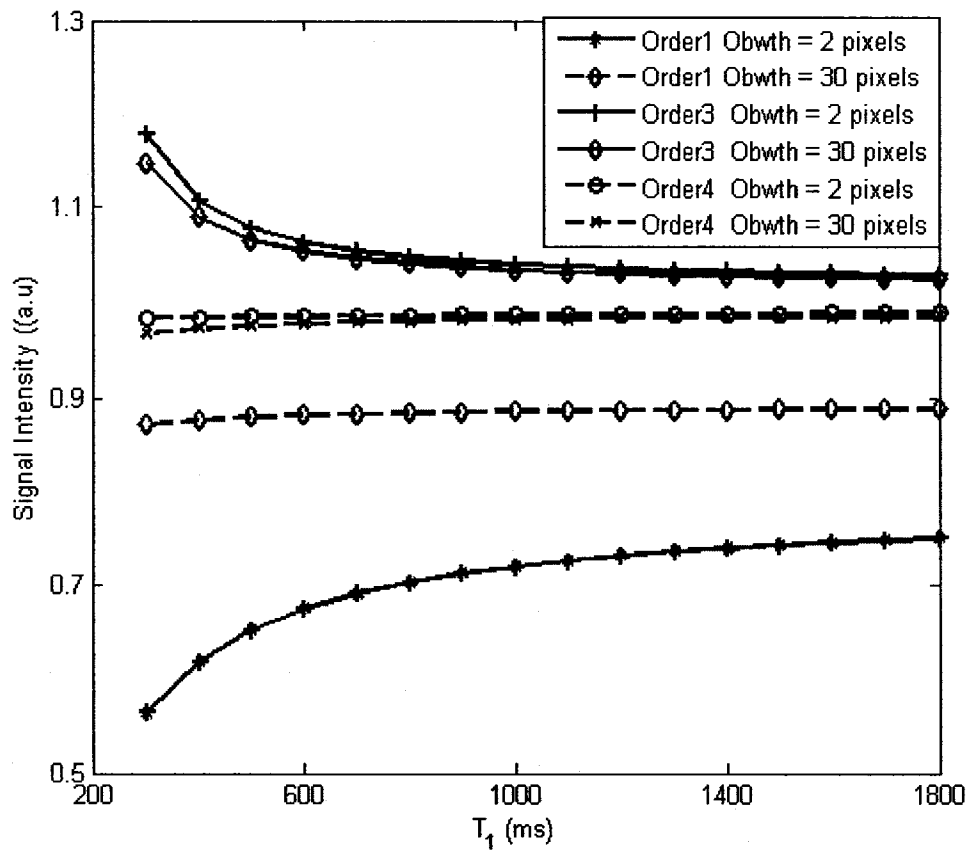


Fig. 4.8: Signal behaviour as a function of T_1 for a 2-pixel object in comparison to a 30-pixel object. An offset was also applied to the plots of order 1 and 3 to provide a better display or visualization, but the relative intensity between the 2 and 30-pixel objects remain the same. Order 2 plot was omitted to enable better visualization of the other plots due to the much enhanced signal of its 2-pixel image.

the centre of k_y -space ($k_y = 0$) for the 30-pixel object and compared to the mean of the signal of the 2-pixel object. The result for order 4 as a function of sample (or tissue) T_1 is

shown to have very little signal loss or enhancement (which is shown by the 2 pixel object for small T_1 values). For order 1, there is an apparent loss of signal for the 2 pixel object for the whole range of T_1 in comparison to the 30 pixel object in contrast to the acquisition using order 2, where the 2-pixel object signal was consistently enhanced in comparison to the 30-pixel object. The gel dosimetry operating range for a gel such as the PVA-Fricke Hydrogel would be approximately 1200 – 200 ms and the difference in PSF effect on a T_1 of 300 ms compared to 200 ms is minimal. Orders 3 and 4 in the plot show the signal of both objects are approximately the same and this favours a k_y -space acquisition using these orders. But the rapidly increasing FWTM of order 3 with variables such as P and/or τ suggests order 4 is still the best way to acquire k_y -space information. A recommendation for image acquisition involving objects with an obvious thin profile, would be to acquire the images such that the long axis of the object is aligned or parallel with the phase encode axis so as to minimize the signal loss. In choosing the value of P and order of filling k_y -space, one should consider the need for a rapid image acquisition in light of possible loss of signal and/or contrast, particularly for small objects.

Fig. 4.9 shows the mean image signal as a function of the pixel width due to the PSF effect for a simulated object of $T_1 = 600$ ms. A similar trend was observed for other T_1 values. For orders 3 and 4, this is almost constant with object width with a slight enhancement at 2 pixels. However, order 1 shows a loss of signal from 10 pixels to 2 pixels while order 2 shows an opposite trend within the 10 pixels to 2 pixels region. These simulations used a τ of 10 ms, which is the minimum attainable with our imaging

system. Smaller inter-pulse timings will give less smearing effect from their PSFs and a correspondingly smaller FWTM.

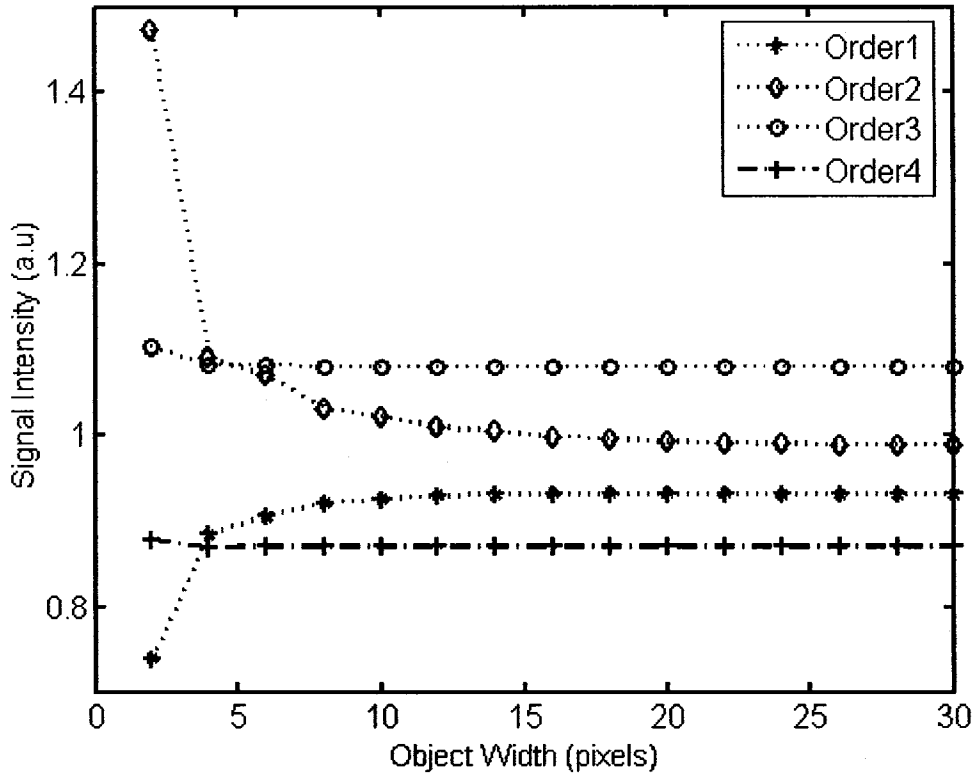


Fig. 4.9: Trend shown by image signal as a function of object width using the 4 acquisition orders. As in Fig. 4.8, an offset was applied to orders 1,3 and 4 to enable better visualization of the plots.

Experimental Signal Profiles along y-axis

Fig. 4.10 shows the experimental 1-D image profiles acquired for the 4 different orders measured with a value of $P = 16$. In Fig. 4.10 (a) the loss of signal at the edges for images acquired using order 1 can be seen. For images acquired using order 2, an enhancement at the edge of the images can be observed with the rest of the image at the noise level thus completely ruling out 3-D LL image acquisition using this order. This is because the centre of the k-space (which governs most of the bulk signal and contrast) for these images is acquired when the recovery curve or magnetization has almost if not

completely recovered. Fig. 4.10 (c) and (d) show little or no signal loss at the edges but rather seem to show some signal enhancement at the edges particularly for order 4. This would further suggest that there should be little signal loss for small object widths when imaged with order 4. However, comparison of order 1 with order 4, as can be seen from Figs. 4.8(a) and (d) shows that there is a relative loss in signal of $\sim 50\%$.

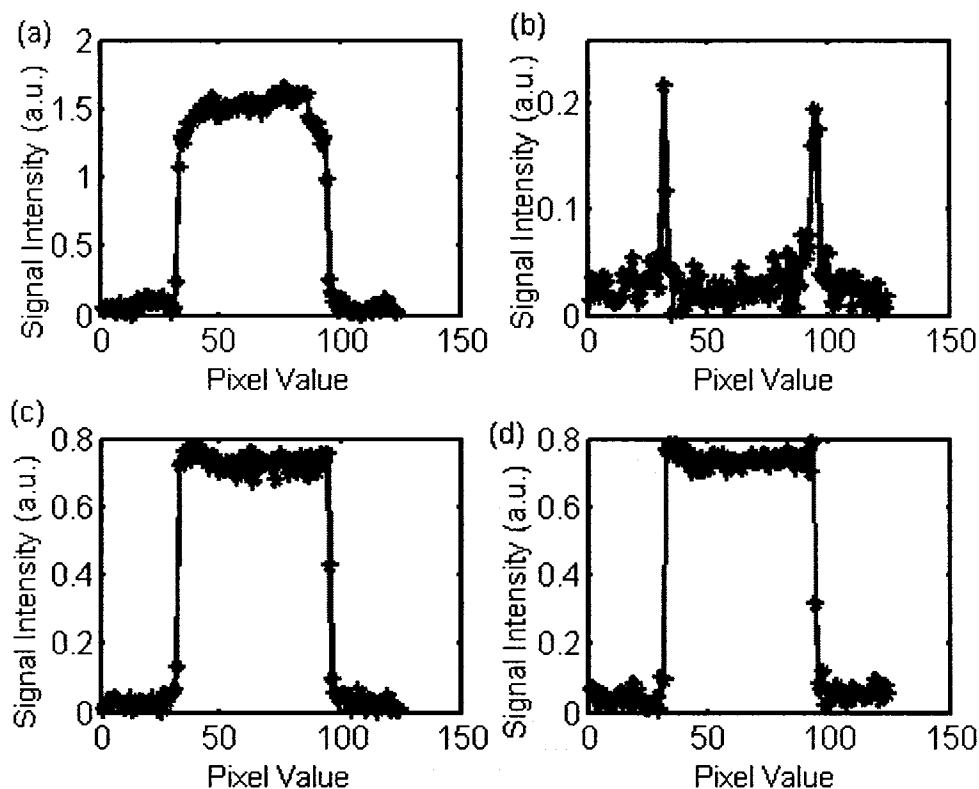


Fig. 4.10: Experimentally reconstructed image profiles in the phase encode direction from k-space acquired data using the following ordering (a) order 1, (b) order 2, (c) order 3 and (d) order 4

This confirms the results obtained from simulations which also showed a relative loss in signal of $\sim 50\%$. Thus on the basis of signal or SNR alone, k-space ordering using order 1 would be a better choice for data acquisition, but in order to avoid loss of signal from small objects and avoid blurring at the edges, order 4 would be a better choice. The

choice of ordering between order 1 and 4 for dosimetry (apart from avoiding small object loss and blurring) should therefore be based on the derived accuracy in estimating the T_1 values as described in the “ T_1 accuracy and dose resolution” section below.

Spatial Resolution Loss

For a T_1 of 250 ms, using the 3-D LL imaging variables with $P = 8$, $\beta = 20^\circ$, $TR = 4s$, $\tau = 10$ ms. σ_{img} and σ_{diff} were converted to pixel values by normalizing their values with σ_{img} thereby permitting the effective resolution to be estimated in terms of pixels. For the 3-D LL imaging order 4 (in order to provide the minimum resolution due to the PSF) to fill k-space with $P = 8$, $\beta = 20^\circ$ (to provide sufficient SNR for the accurate estimation of T_1 values), $TR = 4s$, $\tau = 10$ ms, one can compute an estimate of the effective resolution of ~ 1.3 pixels using Eqns.4.8 - 4.10. The computed $\sigma_{eff} \sim 1.3$ pixels employed a PSF resolution (or FWHM) $\sigma_{PSF} = 0.76$ pixels for the optimized variables given above. Note that because the calculation of the resolution loss due to diffusion in Fricke gel uses the total acquisition time, this provides the worst case of diffusion that can be observed within the gel being imaged and the lower value of $T_1 = 250$ ms provides the worst case resolution due to PSF effects. Nevertheless, the spatial resolution is of order 1 pixel (and thus 1 mm) which is about the 1 mm spatial resolution acceptable for gel dosimetry for MR imaging.

T_1 Accuracy and Dose Resolution

T_1 Accuracy: The experimental T_1 values of the gadolinium samples made were estimated to have a standard deviation (on the fitted parameters) of approximately 1.5 % using the 3-D LL with the k-space coverage employing order 4. Table 4.1 compares the

T_1 estimates of the samples using order 1 and order 4. With data acquired using order 1 (in which the first pulse is assigned to the centre of k-space), a significant loss in accuracy of the estimated T_1 when compared to the inversion recovery estimated T_1 was observed as shown in column 1 of Table 4.1. On increasing this value of n_c to $n_c + 3$, an improvement in the accuracy of the estimated T_1 was observed, though it is still significantly lower than the T_1 estimated from data acquired using “order 4” for the k – space acquisition which showed an accuracy within 2 % (Table 4.1). For data acquired using order 1 with $P = 16$, the same loss and later improvement in accuracy was observed when n_c was changed from 1 to 8. The improvement in accuracy using order 1 when n_c was changed to assume the same value for order 4 shows that the optimal values or formula for acquiring the centre of k-space is given by:

$$n = P(m-1) + P/2 \quad (4.16)$$

where $m = 1, 2, \dots, M$.

Table 4.1: Estimated T_1 values in (ms) from data acquired using order 1 (column 1) and order 4 (column 3). Column 2 is for T_1 estimated from data acquired using order 1 with n_c increased by 3 (from the value used in data acquisition) during the fitting process. In parentheses is the mean accuracy (defined as $|T_{1_LL} - T_{1_IR}| \times 100 / T_{1_IR}$) of T_1 estimates using $\tau_r = 120$ ms, $\beta = 20$ and $M = 10$, and $P = 8$ values.

| Order 1 - T_1 (accuracy) | Order 1 - T_1 (accuracy) | Order 4 - T_1 (accuracy) |
|----------------------------------------------|----------------------------------------------|----------------------------------------------|
| $n_c = 1$ | $n_c = n_c + 3$ | $n_c = 4$ |
| 148 ± 3 (33.6 %) | 267 ± 4 (19.7%) | 227 ± 3 (1.8%) |
| 299 ± 4 (26.7 %) | 447 ± 7 (9.6%) | 405 ± 5 (0.9 %) |
| 407 ± 6 (29.6%) | 588 ± 7 (1.9%) | 579 ± 7 (0.5 %) |
| 598 ± 8 (22.7%) | 900 ± 13 (16.3%) | 789 ± 10 (2.0%) |
| 770 ± 15 (15.2%) | 968 ± 24 (6.6%) | 920 ± 14 (1.4%) |

An n_c value of $P/2$ gave the best accuracy when compared to other k-space coverage which had n_c different from $P/2$ using the order 3.

In the conventional 3-D LL study by *Henderson et al* [104], they opted not to use the k-space ordering “order 1” indicated in this work, but used the relationship $n = 16(2m-1)$ for the tip angle assigned to the centre of k-space. This means that in the study by *Henderson et al* [104] where they used $P = 32$, it is the 16th tip angle pulse or $n_c = P/2$ that was assigned to the centre of k-space for the $m = 1$ inversion time image. This is in agreement with k-space ordering “order 3” and “order 4” used in this study which provides an optimal accuracy for T_1 when compared to the other k-space orderings despite the significant loss in signal when order 1 is compared to order 4 method for filling out the k-space. In the *Henderson et al* [104] study, despite using $n_c = P/2$, the overall k-space coverage pattern they used is similar to “order 3” which tends to have a long PSF tail smearing across many pixels as already indicated by the behaviour of the simulated FWTM with variables such as tip angles β , P and τ_r . So k-space order 4 is seen as a recommended method of filling out k-space for the purpose of gel dosimetry. This optimal accuracy using order 4 k-space coverage was obtained despite the relative loss in SNR between data acquired using order 1 and order 4 which gives estimated average standard deviation of 1.5 % for T_1 .

Dose Resolution: A standard deviation of ~ 2.1 % was observed on the $R_1 (=1/T_1)$ map obtained from acquired baseline images of a homogeneously filled liquid cylindrical phantom (~ 7.5 cm diameter). This was calculated from a region of the phantom image containing about 4409 pixels with the image having a resolution of $\sim 1 \times 1 \times 3$ mm³, with

the 3mm being in the slice direction (from a 128 x 128 x 16 imaging matrix). These images were acquired using k-space ordering method order 4. Since this method employs phase encoding in the slice-selection direction, there is an improvement in SNR of $\sqrt{N_{sl}}$ (N_{sl} = number of phase encoding steps in the slice selection direction) when compared to the multislicing 2-D LL method. From Eqn. 4.15, the dose resolution calculated for three different levels of confidence is shown below in Fig. 4.13. None of the estimated dose resolutions meets the 2 % ICRU recommended for dose uncertainty (extrapolated by *Baldock et al* [51] based on recommended computer dose calculations uncertainty not exceeding 2% [52] and the clinically recommended delivered dose to patients not exceeding the prescribed dose by 5% [115]). This inability to attain the 2% ICRU recommended dose uncertainty doesn't necessarily come only from the limitation in the uncertainty in measuring R_1 ($=1/T_1$) but also from the low dose response of the Fricke-Hydrogel ($0.033 \text{ s}^{-1}\text{Gy}^{-1}$ [114]) when compared to dose responses of about $0.108 \text{ s}^{-1}\text{Gy}^{-1}$ (*Olsson et al* [30]) and $0.200 \text{ s}^{-1}\text{Gy}^{-1}$ (*Gambarini et al* [116]) obtained for other Fricke gel dosimeters (gelatin and agarose based Fricke-gel dosimeters). The attractiveness of the PVA-Fricke hydrogel, despite its low dose response is its low diffusion coefficient and auto-oxidation compared to other Fricke gels. This inability to attain the ICRU 2% dose uncertainty recommendation has also been observed for most of the polymer gel (PAG) dosimeters which has been the focus of much recent research, partly due to its stability in terms of retaining spatial information over time when compared to Fricke-based gel dosimeters. For instance, in the study by *De Deene and Baldock* [56], on the PAG gel dosimeter (PAG gel dosimeters have a typical dose response of $\sim 0.331 \pm 0.012 \text{ s}^{-1}\text{Gy}^{-1}$

[42]) the ICRU 2% deviation from reference dose was not attainable even after relaxing the confidence level to 52 %.

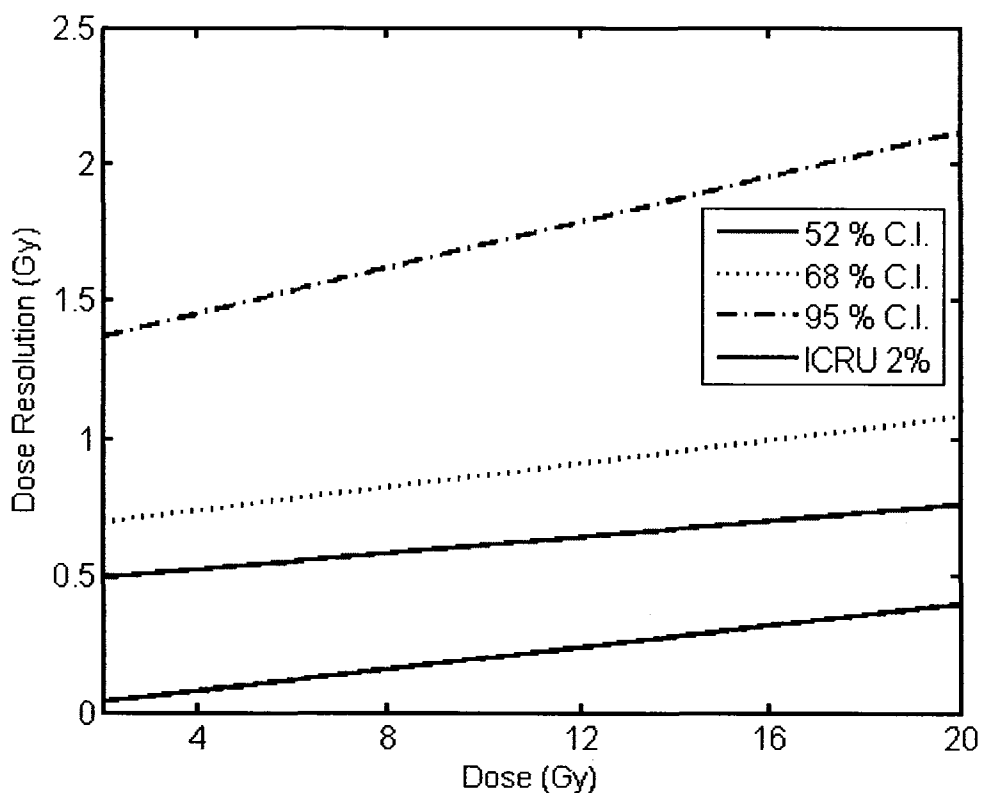


Fig.4.11. Expected PVA-Fricke hydrogel dosimeter dose resolution estimates for 52, 68 and 95% confidence levels for measurements taken using 3-D LL. Also shown is the ICRU 2 % recommended dose uncertainty.

The percent standard deviation of the T_1 of ~ 2.1 % obtained from a homogeneous phantom shows that 3-D LL has potential as a gel dosimeter especially for Fricke-based gel dosimeters suffering from the effect of spatial information blurring due to the diffusion of ferrous and radiation-induced ferric ions from their site of formation. Thus, while more work on the 3-D LL imaging sequence might be required, further work on improving the sensitivity of the PVA-Fricke gel is also required, if the 2% ICRU dose resolution is to be attainable.

4.5 Conclusion

From the study of the behaviour of the PSF (FWTM) and its effect signal profile, signal loss amongst others shown, these factors would suggest order 4 as the best way to acquire data for the purpose of imaging particularly in the case of gel dosimetry where an attempt to have areas with high dose gradients aligned with the read encode direction to limit loss of small objects signal might not be possible. A value of P as small as possible within the imaging constraints required should be chosen so as to limit the PSF effect due to the modulation of k_y -space during image acquisition. When this is combined with the effect of diffusion of ferric ions in the case of Fricke-based gel dosimeters, and the need for a better SNR at a flip angle of 20° , a value of $P = 8$ would be recommended to limit the loss of information particularly in areas of high dose gradients and/or possible hot spots present in a gel dosimeter. The total imaging (or acquisition) time could be reduced with little or no loss in the effective resolution by increasing P to 16 but with the tip angle reduced to 15° (gives $\sigma_{\text{eff}} = 1.37$ pixels).

Chapter 5

T₂ Imaging and B₁ Field Inhomogeneity Correction

5.1 Introduction

The polymer based gel dosimeters such as the PAG [36-39] gel dosimeter consist of a matrix (usually gelatin) in which monomers (acrylamide) and cross-linkers (N,N'-methylene-Bis-acrylamide) are dissolved. Upon irradiation, this gel dosimeter experiences a polymerization of the co-monomers to polymers (polyacrylamide) resulting in a change in the spin-spin relaxation time parameter T₂ [36-39]

The relaxation rate parameter 1/T₂ (R₂) has been found to be proportional to the dose given (at least for a given dose range) to the PAG gel dosimeter. In polymer based gel dosimeters, the R₂ is the most efficient dose enhanced MR imaging parameter compared to longitudinal (or spin lattice) relaxation rate parameter R₁ (1/ T₁). Given the three-dimensional (3-D) capability of magnetic resonance (MR) imaging, this means 3-D dose information can be obtained for PAG gel dosimeters via R₂ maps. This thereby provides a route for 3-D dose verification; especially given the advent of complex dose deliveries techniques such as IMRT which are geared towards obtaining better dose conformation to a tumour.

As noted earlier R₂ can usually be obtained from raw images acquired using a MEMS imaging sequence or the simple spin-echo sequence usually which uses a pair of spin-echo images. For the MEMS sequence this requires the application of a 90° RF pulse

followed by the repeated application of 180° pulses with signal acquisition (or images) performed in between these 180° RF pulses while the signal is decaying producing images with different T_2 weighting during a single repetition time. In MR imaging, artifacts may perturb a dose map since the dose maps are calculated via the measured R_2 . One of the sources of these inaccuracies is RF or B_1 -field inhomogeneities. B_1 -field inhomogeneities can arise from multiple sources: RF amplifier distortions [117], digitization of the RF pulse [118], RF coil geometry [119,120] and non-uniform penetration of the scanned object [121,122]. B_1 -field inhomogeneities tend to influence the slice profiles and lead to a variation of the actual RF tip angle from the expected values. This can in turn lead to the generation of unwanted signals, in particular stimulated echoes (STEs) in MEMS sequences [123] to varying extents depending on the excited slice. These signals interfere with the MEMS echo train introducing inaccuracies in the dose maps via the R_2 parameter.

STEs arise from incomplete excitation and refocusing of spins subject to multiple (>2) RF pulses. In a multiple spin-echo sequence, transverse magnetization may be stored in the longitudinal direction following a second RF pulse during which time spin-lattice relaxation occurs rather than spin-spin relaxation. STEs can affect signal strength and lead to image artifacts (e.g. zipper or mirror artifacts [123]) A useful method for reducing STEs effects involves combining images acquired using a Carr-Purcell (CP) and a Carr-Purcell-Meiboom-Gill (CPMG) multiple spin-echo imaging scheme [123]. This imaging scheme is also known as the phase alternating phase shift (PHAPS) sequence which involves alternation of the phases of the 180° RF pulses. An alternative to PHAPS involves mapping the axial and transverse B_1 -field of the RF coil and correcting MEMS

images. In this chapter the PHAPS and B₁ corrected methods are compared. The axial mapping used in this study is based on a method by *Barker et al* [124], and the transverse mapping follows that by *Akoka et al* [108].

5.2 Theory and Method

5.2.1 B₁-field Mapping

The mapping of the B₁ field was done both longitudinally (B_{1z}) and transversely (B_{1xy}). These B₁-field maps provide calibration factors which can then be used to correct for the effects of the non-uniformity of the B₁-field.

B_{1z} Uniformity Mapping:

The longitudinal axis mapping was based on the method by *Barker et al* [124] summarized below. This method employs a spin-echo sequence where, for a uniform sample, the NMR signal $S(\mathbf{r})$ from a point with vector position \mathbf{r} can be written as [124]:

$$S_i(\bar{\mathbf{r}}, p_i) = \left| K_{sc}(\bar{\mathbf{r}}) \sin^3(\theta(\bar{\mathbf{r}})T(\bar{\mathbf{r}})) \right| \quad (5.1)$$

where S_i is the signal measured at transmitter output p_i ; the scaling constant K_{sc} is given by product of the proton density $\rho(\bar{\mathbf{r}})$; the receiver field dependence $R(\bar{\mathbf{r}})$; and a constant of proportionality k , representing the gain at a reference point, the isocentre. This scaling constant is given by:

$$K_{sc}(\bar{\mathbf{r}}) = k\rho(\bar{\mathbf{r}})R(\bar{\mathbf{r}}) \quad (5.2)$$

$T(\bar{\mathbf{r}})$ defines the spatial dependence of the transmitter field and $\theta(\bar{\mathbf{r}})$ is given by:

$$\theta(\bar{\mathbf{r}}) = \frac{\pi}{2} \frac{b(p_i)}{b(p_{\pi/2}, 0)} \quad (5.3)$$

with $i=1,2,\dots,N$. Here the function $b(p_i)$ is the transmitter output (in either volts or watts).

In this case the transmitter output is given by:

$$b(p_i) = 10^{(TA_i - TA_0)/200} \quad (5.4)$$

where TA_i is the transmitter attenuation or gain and TA_0 is the transmitter gain for a reference tip angle in this case $\pi/2$. The units of TA_i and TA_0 are in 1/10 dB. $T(\vec{r})$ and $R(\vec{r})$ are normalized to a reference position, measured in this study at the isocentre ($\vec{r} = 0$), such that $T(\vec{r} = 0) = R(\vec{r} = 0) = 1$. Fitting the measured signal at the isocentre to Eqn.5.7 gives $k\rho(\vec{r} = 0)$ and $P_{\pi/2,0}$ (since $T(\vec{r} = 0) = R(\vec{r} = 0) = 1$) while fitting any other position gives $k\rho(\vec{r})R(\vec{r})$ and $T(\vec{r})$. The above method of mapping the B_1 -z field for the transmitter output $T(\vec{r})$ works for both a homogeneous and heterogeneous phantom since the proton density appears in Eqn 5.1 as a multiplicative constant. This would only affect the signal amplitude and not the transmitter output required, thus can be used for a heterogeneous material samples as demonstrated by *Barker et al* [124]. This method of mapping the B_1 -field along the longitudinal axis has been shown to be independent of the material in the sample being imaged due to the fact that it (the B_1 -z field) has no dependence on the dielectric properties of the sample unlike the transverse B_1 -field [125].

This above method was used to map the longitudinal B_1 -field since, in a gel phantom where there might be inhomogeneities inserted into the gel matrix having different dielectric properties, B_{1z} is expected to change with each new gel phantom. The phantom (cylindrical) used to map the B_1 field was of the same dimensions as the subsequent phantoms described in Chapter 7 for dose verification, to avoid the problem of B_1 dependence on the coil/sample loading characteristics. In B_1 -z field mapping, a

simple spin-echo sequence was used; it was modified to acquire slice profiles along the longitudinal axis with slice thicknesses of 2 mm for different power (or attenuation) settings. Since this method for mapping the uniformity of the transverse B₁-field (B₁-xy) has a dependence on the sample properties and the material in the phantom has to be uniform, the method suggested by *Akoka et al* [108], which has no dependence on sample properties and provides a pixel-by-pixel B₁-xy field mapping was used.

B₁-xy Uniformity Mapping:

The *Akoka et al* [108] method is based on the imaging sequence shown in Fig. 5.1. This imaging sequence makes use of three RF pulses inducing flip angles of values α , 2α and α respectively. This three pulse train generates five different echoes but only the first 2 echoes are acquired and used to calculate the tip angle α (and thus the B₁-xy field on a pixel-by-pixel basis). The first echo acquired is the classical spin-echo acquired at time TE/2 (TE stands for echo time) after the second RF pulse and the second echo is a stimulated echo (STE) acquired at time TE/2 after the third RF pulse. The signal equation describing the signal from these two echoes is given by [108]:

$$S_{SE}(i, j) = k \sin^3(\alpha(i, j)) \quad (5.5)$$

and

$$S_{STE}(i, j) = \frac{k}{2} \sin^2(\alpha(i, j)) \sin(2\alpha(i, j)) \quad (5.6)$$

where k is simply a proportionality (or catch-all gain) constant, S_{SE} and S_{STE} are the image signal intensities for the first echo and the second echo respectively. From the ratio

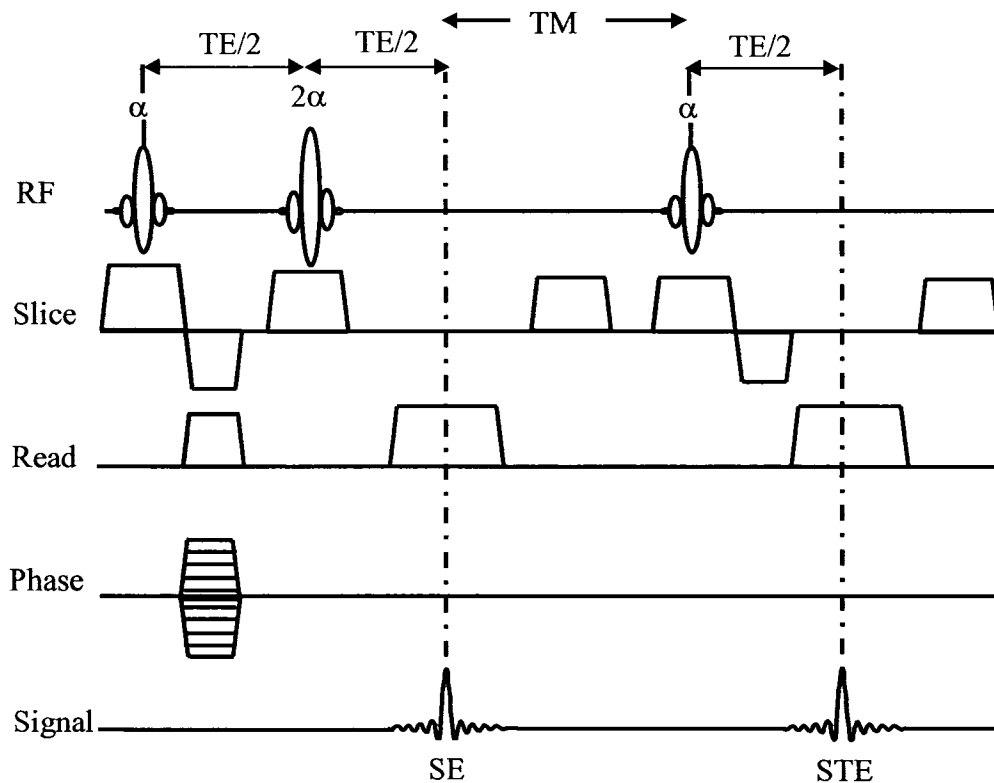


Fig. 5.1: The imaging sequence diagram used to calibrate the flip angle (and hence the transverse B_1 -field) on a pixel-by-pixel basis. The labels SE and STE stand for spin-echo and stimulated echo respectively.

of these image signal intensities the flip angle was calculated by [108]:

$$\alpha(i, j) = \cos^{-1}(S_{STE}(i, j)/S_{SE}(i, j)) \quad (5.7)$$

This method has no dependence on the sample properties (ρ , T_1 , T_2). Its non-dependence on T_1 makes it relatively fast since the repetition time TR is usually set in most imaging sequences to allow sufficient recovery of the magnetization due to T_1 , thereby prolonging image acquisition time.

5.2.2 Multiple Spin-echo Imaging Schemes –(MEMS and PHAPS Relative Performance)

The T_2 (or R_2) of a gel matrix measurement using the MEMS and the PHAPS imaging schemes is described in this section.

MEMS Imaging Scheme:

The MEMS sequence implemented in the 1.89T magnet is shown in Fig. 5.2. This sequence is based on the CPMG based imaging scheme which involves applying a 90° RF pulse to nutate the magnetization into the transverse plane. This 90° RF pulse is then followed by the repeated application of 180° RF pulses at 90° out of phase from the 90° RF pulse. Thus a short hand notation for this sequence can be written as: $90-x' - 180-y' - 180-y' \dots - 180-y'$. This $90-x' - 180-y' - 180-y' \dots - 180-y'$ procedure is repeated for all the phase encode lines required to completely fill the k-space. In order to preserve phase relationship between any generated stimulated echoes and spin-echoes, the phase encode gradient is rewound before each 180° pulse.

It has been shown that in conventional MR sequences where linear k-space sampling is used, a temperature rise of 3°C can be attained and can result in a dose underestimation of up to 10 % [54]. Thus, all our spin-echo based sequences (MEMS and PHAPS) were modified to do centric k-space acquisition which would limit any errors due to temperature rise as a result of RF deposition to areas of high dose gradients [54].

PHAPS Imaging Scheme:

This imaging scheme is almost the same as for the MEMS or CPMG sequence except that each y k-space line is acquired twice using (i) a CPMG-encoding scheme, 90-

$x' - 180-y' - 180-y' \dots - 180-y'$ and (ii) a CP-encoding scheme, $90-x' - 180-x' - 180-x' \dots - 180-x'$. The magnetizations were added algebraically according to the PHAPS sequence formulae given by [123, 125]:

$$M_{PHAPS} = \frac{M_{virtual} + M_{real}}{2} \quad (5.8)$$

with

$$M_{real} = \left\{ \left(M_{x,CP} - M_{x,CPMG} \right)^2 + \left(M_{y,CP} - M_{y,CPMG} \right)^2 \right\}^{1/2} \quad (5.9)$$

and

$$M_{virtual} = \left\{ \left(M_{x,CP} + M_{x,CPMG} \right)^2 + \left(M_{y,CP} + M_{y,CPMG} \right)^2 \right\}^{1/2} \quad (5.10)$$

for the odd echoes in the multiple echo sequence and

$$M_{real} = \left\{ \left(M_{x,CP} + M_{x,CPMG} \right)^2 + \left(M_{y,CP} + M_{y,CPMG} \right)^2 \right\}^{1/2} \quad (5.11)$$

and

$$M_{virtual} = \left\{ \left(M_{x,CP} - M_{x,CPMG} \right)^2 + \left(M_{y,CP} - M_{y,CPMG} \right)^2 \right\}^{1/2} \quad (5.12)$$

for the even echoes in the multiple echo sequence.

The resultant transverse magnetization given by the echo amplitudes (for both PHAPS and MEMS) collected for every given image pixel was fitted by an exponential function in order to extract the T_2 parameter according to:

$$S(i, j) = A \exp(-nTE / T_2) \quad (5.13)$$

where TE is the echo time and $n = 3, 4, \dots, N$ with N being the total number of images acquired. The first two images were not used in the fit since these points seemed to deviate from the mono-exponential decay given in Eqn. 4.13 probably due to non-

existence of stimulated echo effects. A two-parameter fit of the scaling constant A and the spin-spin relaxation time constant T_2 was done. All fits were done using the Matlab software package (Matlab 6.3, The Math Works Inc. USA).

For both the MEMS and PHAPS imaging schemes, the following variables were used: $TE = 40$ ms, 26 echoes, a repetition time, $TR = 4000$ ms which increased accordingly depending on the number of slices being imaged, field of view (FOV) = 128 mm, a matrix size of 128×128 , slice thickness (ST) = 5mm with slice interleaving

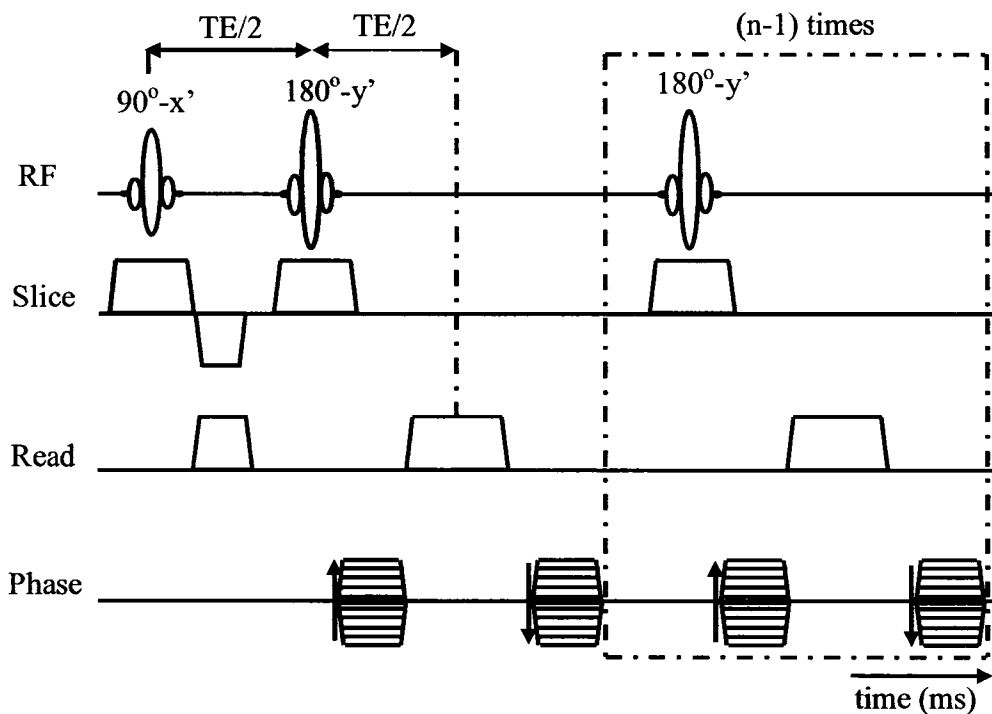


Fig. 5.2: The schematics of the MEMS (CPMG) imaging sequence used to acquire baseline images for the estimation of T_2 .

employed in order to limit the amount of magnetization “cross-talk” between slices [91].

The choice of $TE = 40$ ms was made based on an investigation of the quality of the raw images acquired using multiple spin-echo based sequences in our imaging system. It was

found that images acquired with TE less than 40 ms gave low quality images corrupted by an artifact. Since the PHAPS sequence acquisition time (TA) is twice that of a normal MEMS sequence, the number of averages for the MEMS sequence was doubled in order to make the acquisition times for both MEMS and PHAPS comparable. All measurements were done using a cylindrical, uniform gel-filled phantom.

5.2.3 Correction of effects of B_{1z} and B_{1xy} inhomogeneities

In both the PHAPS and MEMS imaging sequences, the scaling factor for the transmitter field $T(\vec{r})$ obtained from mapping the B_{1z} field was used to modulate the power setting depending on the slice being excited along the longitudinal axis. These scaling or modulation factors were programmed into the imaging sequences (MEMS and PHAPS) to automatically update the power setting for the slices in question. This active power modulation follows a similar scheme used in correcting the effects of B_{1z} on the estimated T_1 suggested by *Clare et al* [126].

The correction of the effects of B_{1xy} field inhomogeneities was done by obtaining an R_2 versus flip angle (α) calibration curve using a homogeneous cylindrical phantom of the same dimensions as that of the polymer gel phantoms used in Chapter 7. The α vs R_2 calibration curve data was fitted to a polynomial and permitted the generation of a set of correction factors given by:

$$CF(\alpha) = \frac{R_{2_true}}{R_2(\alpha)} \quad (5.14)$$

where R_{2_true} is the relaxation rate value of the homogeneous gel determined using a bulk (or spectroscopic) sequence. This is a sequence with no imaging gradients applied. This

calibration curve allowed the correction (or scaling) of R_2 maps subsequently acquired using the MEMS sequence. The R_2 dependence on α shown by MEMS was not observed for the PHAPS imaging sequence.

5.3 Results and Discussion

B_{1z} Uniformity Mapping and Correction:

Fig. 5.3 shows the slice profiles acquired using a simple spin-echo sequence with slice thicknesses of 2 mm for a given power setting. It can clearly be seen that as one

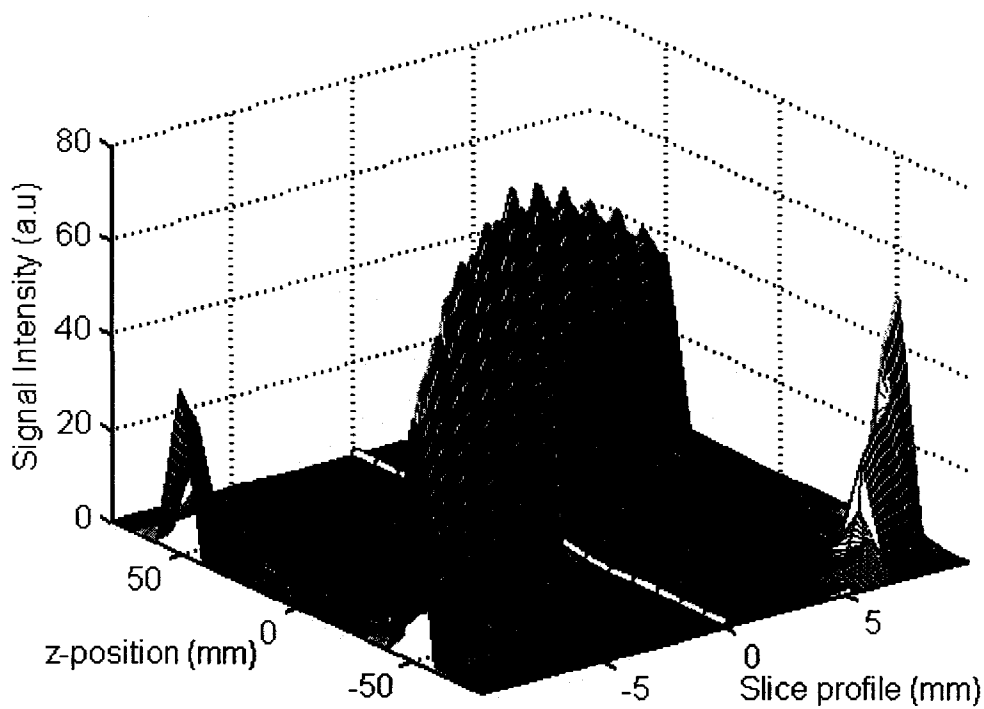


Fig. 5.3: Slice profiles acquired along the longitudinal axis (z-axis) of the magnet with slice thicknesses of 2 mm each. The spikes at the edges are from a wrap-around artifact brought about due to the fact that the product of the slice thickness and number of slices exceeded the FOV in the slice-select direction.

moves away from the isocentre of the magnet, the amplitude of the slice profiles are reduced more and more. This reduction is a consequence of the non-uniform behaviour of the B_1 field along the longitudinal axis. This is expected for a birdcage coil [125].

Fig. 5.4 shows the flip angle calculated from Eqn. 5.2 where the flip angle is scaled by the spatial dependence of the transmitter field $T(\vec{r})$. The scaling factor $T(\vec{r})$ was then used to modulate the power setting depending on the slice being excited along the longitudinal axis. This provided a uniform excitation of a given flip angle value along the longitudinal axis. This corrected flip angle is given in Fig. 5.4 and represented by the “corrected B_1 ” legend shown on the graph. The advantage of doing a slice-by-slice power modulation to provide a uniform flip angle is that it provides a better signal-to-noise ratio

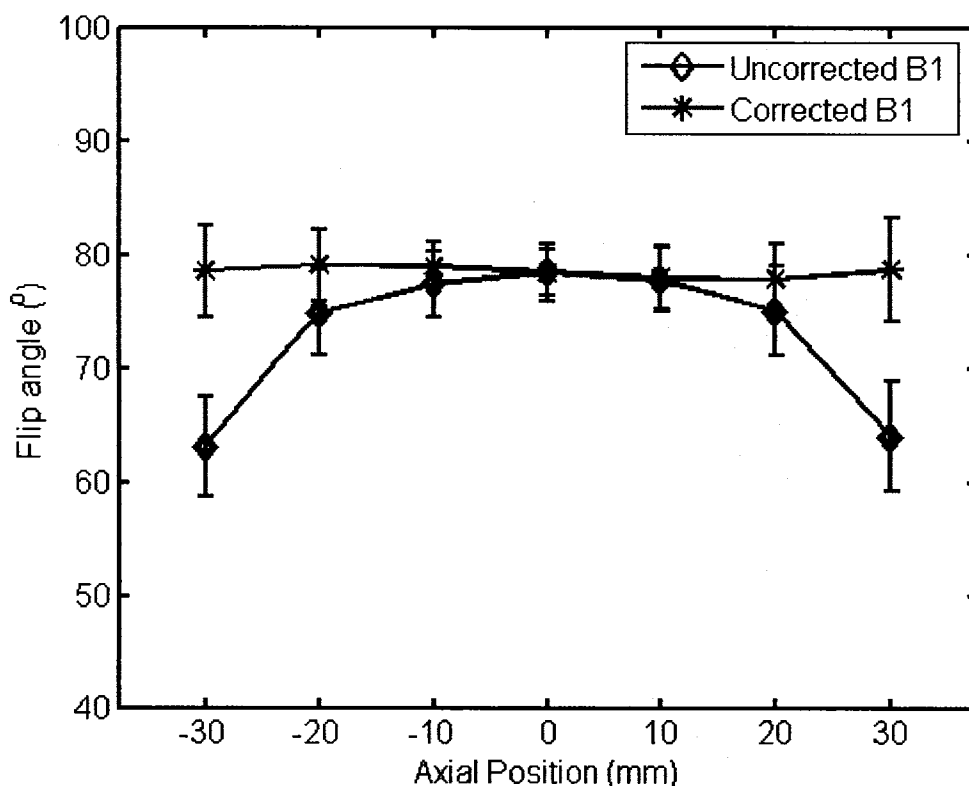


Fig. 5.4: The longitudinal B_1 -field (B_1 -z) prior to correction and after correction using automatic power modulation within the imaging sequences.

(SNR) for the baseline images for the estimation of T_2 as opposed to doing a correction of the T_2 after acquiring the baseline images with the non-uniform axial B_1 -field. Little or no change in temperature ΔT (via phase change, $\Delta\phi$, using a FLASH sequence since $\Delta T \propto \Delta\phi$ [54]) was observed as a result of the power modulation calibration included in the imaging sequences for 16 slices, 2 averages with a matrix size of 128 x 128.

B_{1xy} Uniformity Mapping and Correction:

Fig. 5.5 (a) is a typical B_{1xy} map shown here as a flip angle image acquired using the sequence given in Fig. 5.1. Fig. 5.5 (b) shows a simple one dimensional (1D) B_{1xy} profile drawn across the image to show the non-uniformity of B_{1xy} . This B_{1xy} map was acquired for every slice imaged using a MEMS imaging sequence. The T_2 (R_2) was calculated for every image pixel and the corresponding B_{1xy} map using the uniform cylindrical phantom.

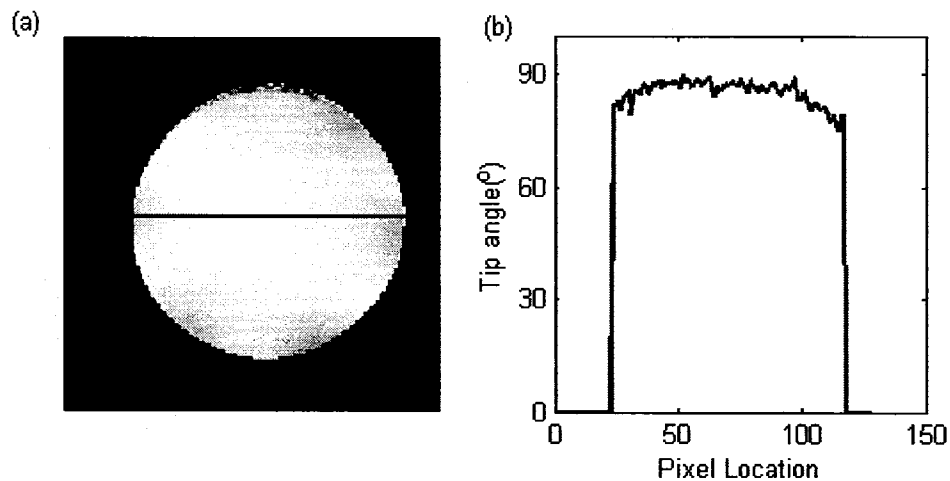


Fig. 5.5: A sample B_{1xy} map displayed as an image (a) and (b) a 1-D horizontal profile drawn through the image showing the change in B_{1-x} with pixel position.

Fig. 5.6 shows the R_2 versus the flip angle curve generated and thus provides a α - R_2 calibration curve. The true relaxation rate value, R_{2_true} , of the homogeneous gel used to generate the calibration curve (shown inset in Fig. 5.6) was used in conjunction with Eqn. 5.14 to generate the R_2 correction factors. These correction factors were then used to scale the R_2 values on a pixel-by-pixel basis depending on the measured flip angle.

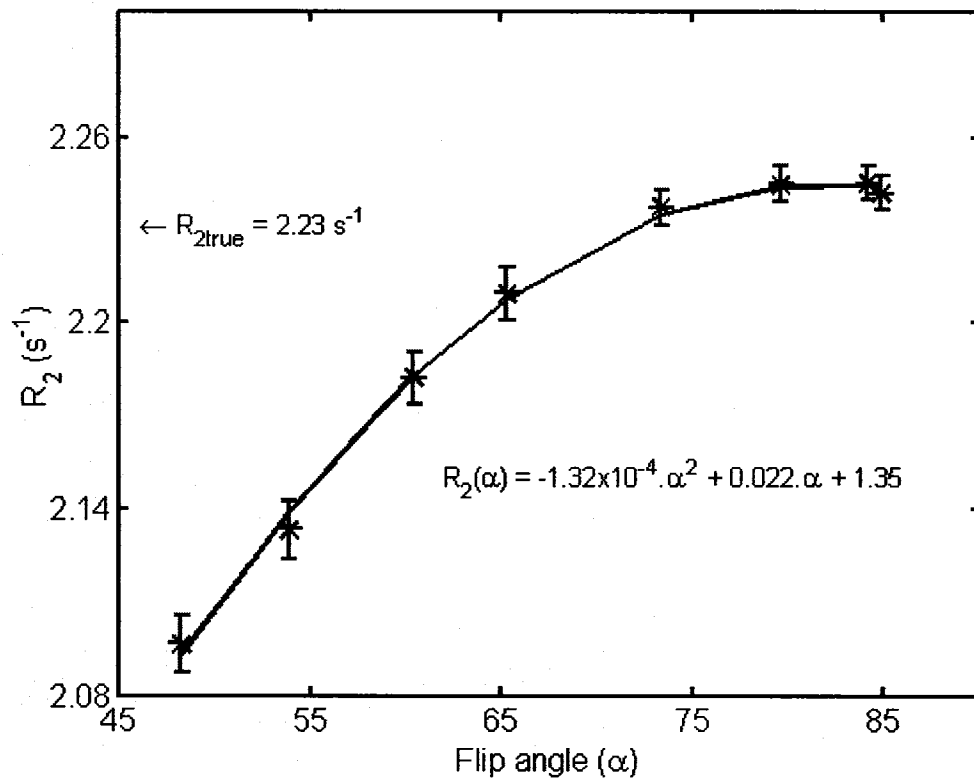


Fig. 5.6: R_2 versus flip angle calibration curve generated for subsequent correction of the effect of B_1 -xy on the R_2 values obtained.

Fig. 5.7 is a 1D R_2 versus position profile showing the R_2 before and after the application of the correction factor CF given in Eqn. 5.14 for a different gel phantom. In the 1-D profile shown in Fig.5.7 the worst percentage deviation of R_2 from the true value before the application of the correction factor is was approximately 3.7 %, but after

application of this correction factor this percent deviation was reduced to about 1.4 % for this given slice.

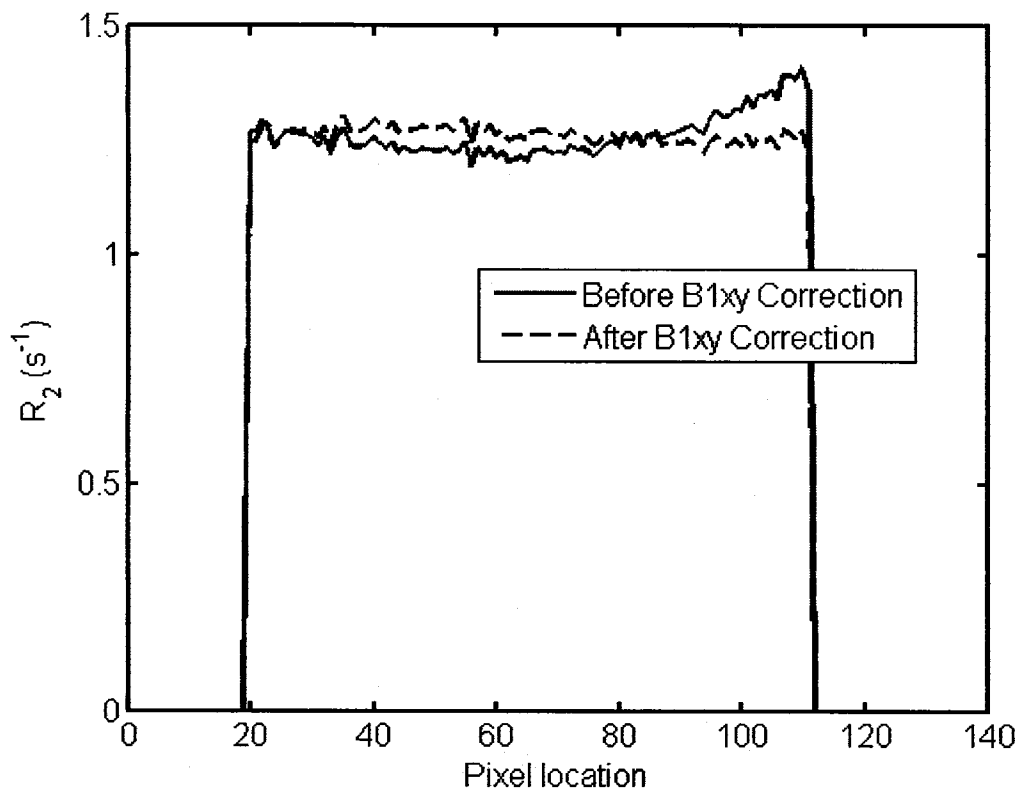


Fig. 5.7: A sample 1-D R_2 profile across an R_2 image before and after correction of the effects of B_{1-xy} on R_2 .

Before the correction of the effect of B_{1-xy} on the estimated R_2 values, the average percentage deviation on the R_2 per given slice was about 3.3 % with a worst value of about 9%. After the correction of B_{1-xy} the intra-slice R_2 deviation improved to within 2 %. Fig.5.8 shows the accuracy in R_2 as function of the longitudinal (or axial) position of the slice. The worst deviation (defined by $100 \cdot \sum (|R_2 - R_{2_true}| / R_{2_true} * 100)$) is about 91 % prior to correction and within 95 % after the correction of the B_1 -field inhomogeneity effects.

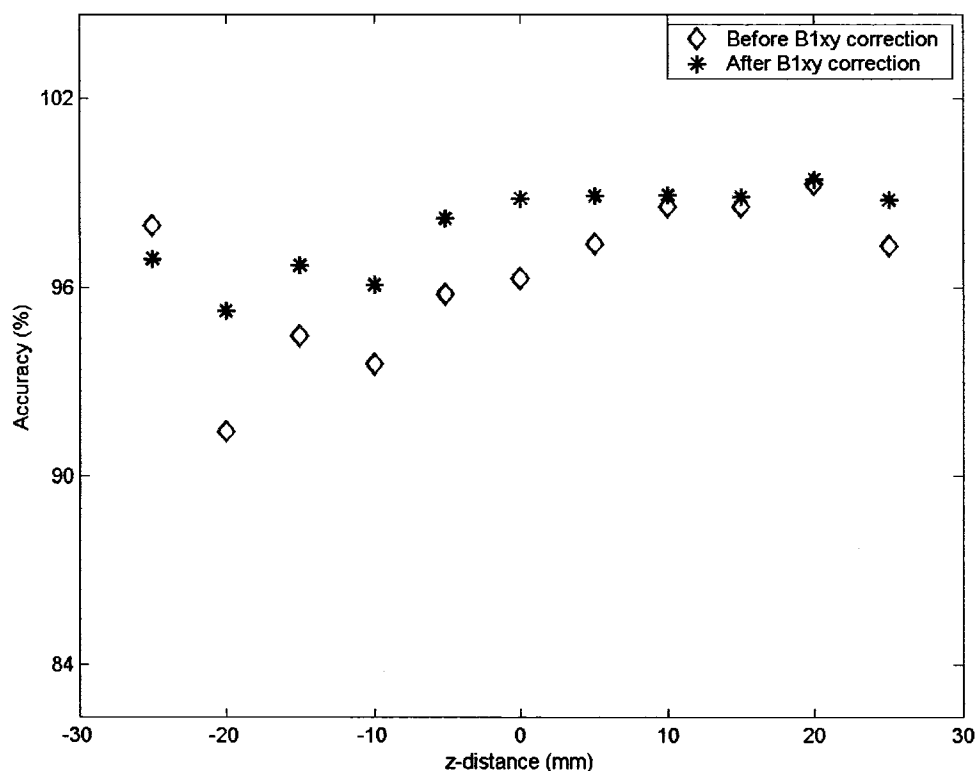


Fig. 5.8: Accuracy of the estimated R_2 values as a function of axial position within the magnet with the zero z-distance on the horizontal axis representing the isocentre of the MR imaging system.

MEMS and PHAPS Imaging Scheme Relative Performance:

Fig. 5.9 (a) shows the relative signal to noise ratio (SNR) comparisons of the baseline images between the MEMS and PHAPS imaging sequences. The SNR was calculated by drawing a region of interest (ROI) within the homogeneous region of the image away from any influence of the background noise for the signal estimation and the noise was estimated from the background away from any influence of the imaged object. The ratio of these two signals gave the SNR values. These same ROIs (~2000 pixels) were propagated through all the MEMS images with: (i) no averaging done, and (ii) MEMS acquired with two averages. The PHAPS image SNR is also shown. The plots

show that the MEMS acquired images with one or two averages have a better SNR compared to the PHAPS acquired images. A closer look at the averaged percentage deviation of the R_2 values from the average values of a given slice (Fig.5.9 (b)) shows the MEMS obtained B_1 -field corrected R_2 is better than the PHAPS estimated R_2 value. This

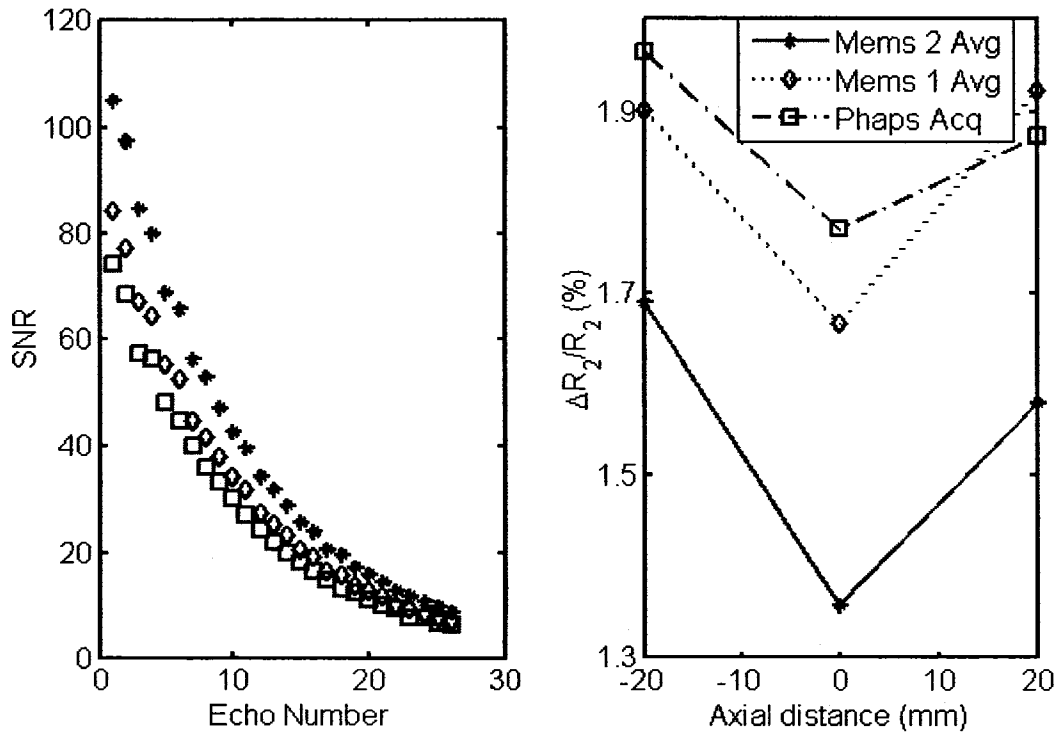


Fig. 5.9: Relative performance of the MEMS and the PHAPS imaging sequence. (a) SNR of the baseline images and (b) precision based on the percentage standard deviation on the mean of the R_2 values for a given slice. The lines were added as a guide to the eye.

can be attributed to the better SNR from the averaged MEMS images for the image acquisition time. In terms of the averaged fitted errors on the estimated R_2 , the MEMS sequence showed an improved error when compared to PHAPS by a ratio of approximately 1.4. Thus, the MEMS imaging sequence when corrected for B_1 -field

inhomogeneities showed a better performance compared to PHAPS (also corrected for B_1 -field inhomogeneities) in terms of SNR and the estimated R_2 values.

5.4 Conclusion

Using a slice-by-slice B_1 axial transmit calibration combined with the correction of transverse B_1 inhomogeneity on a pixel-by-pixel basis provides an intra-slice deviation of the estimated R_2 using multiple spin-echo sequences of less than 2 % for the purposes of gel dosimetry. This slice-by-slice pulse calibration combined with pixel-by-pixel R_2 correction with an acquired B_1 -xy map, can be used to obtain better precision (and/or) using a simple MEMS (or CPMG) when compared to PHAPS for the same total acquisition time. Despite the superior performance of MEMS when compared to PHAPS after correction of B_1 inhomogeneities, it is still advisable to alternate the phase of the application of the 180° RF pulses between $-y'$ and y' for the even and odd phase encode lines so as to push any streak artifacts to the edges of the image which can be then be discarded [123].

Chapter 6

Non-Linear Gradient Field Mapping and Correction

6.1 Introduction

The non-destructive and 3-D nature of MR imaging makes it one of the best methods to evaluate the spatial distribution of dose information in an irradiated gel dosimeter. MR imaging-obtained spatial dose distributions in gel dosimeters can be used as a dose verification tool for the planned irradiation treatment of a patient. However, the use of MR imaging for gel dosimetry for treatment planned dose verification requires minimal or no geometrical distortion in the eventual dose map. In general, MR images can be susceptible to image distortions due to non-linear gradient magnetic fields and/or inhomogeneities in the main (or static) magnetic field B_0 [74,127-133]. The order of distortions can vary from a few mm [133] to distortions of order greater than 25 mm [132] for conventional MRI scanners. Some scanner manufacturers usually provide software ('Grad Warp') to restore the geometry of the imaged object. In some cases, these distortion corrections act on only the phase and read-out directions leaving the slice-selection uncorrected [133]. These distortions are due to the fact that the precise encoding of spatial information (as expected by the reconstruction algorithms) in MR images highly depends on the production of precisely linear variations in the magnetic field across the imaging volume containing the sample or samples during the image acquisition process. These image distortions can have serious consequences when used in

medical applications for diagnostic purposes or for the purposes of dose verification in radiotherapy treatment planning where high spatial accuracy is required.

MR imaging system-dependent errors such as image distortion from non-linear gradients must be reduced as much as possible to obtain the target figure of accuracy in high precision radiotherapy (2-3 % of the maximum dose in the regions of uniform dose and a spatial error of less than 2 mm in regions of high dose gradients [134]).

This chapter describes a method for the mapping and correction of the effects of static field (B_0) inhomogeneity and non-linear gradient magnetic field on MR images (Fourier transform reconstructed) for the 1.89 T MR scanner (Magnex Scientific, Abingdon, Oxon, England) used to implement the 3-D Look-Locker imaging sequence and to measure the spatial dose distribution delivered to gel dosimeters via R_2 ($=1/T_2$) maps studied in this thesis. This gradient field distortion mapping method requires the acquisition of two sets of images of a gel-filled grid phantom with the direction of the applied gradients being altered. From these two sets of images, the change in position of a given imaged point is estimated and then fitted to a three-variable (to account for distortions in all three planes) (x,y,z) fourth-order polynomial. Distortions of the order of 12 mm were measured within the 120 mm imaging diameter of the transmit/receive birdcage coil (Morris Instruments Inc. Ottawa) used. These distortions were reduced to within the order of a millimeter with the aid of the estimated polynomial used to account for the distortions. The magnetic field deviations measured were also considered in the correction of R_2 images, since R_2 values can be affected by large gradient magnetic fields [135].

6.2 Theory and Methods

6.2.1 Theory

A multi-echo multi-slice spin-echo sequence described earlier in Chapter 2 was used to map the field inhomogeneities and gradient field non-linearities. The theoretical derivation presented here follows that by *Chang and Fitzpatrick* [127] and *Kawanaka and Takagi* [128]. The magnetic field gradients used for spatial encoding are the slice-select, read-out and the phase-encode gradients with their magnitude values denoted by G_z , G_x and G_y , respectively. In the absence of any static field inhomogeneity, a slice selective 90° pulse selects an axial slice at $z_1 = (\omega_1 - \omega_0)/\gamma G_z$ where ω_1 is the central angular frequency of the selective pulse, ω_0 is the Larmor frequency (nominal angular frequency value in the absence of gradient fields) and γ is the gyromagnetic ratio. Denoting the duration of the read-out and phase encode gradients by T_x and T_y , the signal obtained in the absence of B_0 inhomogeneities and gradient non-linearity after a time $\tau = t - TE$, ($TE - T_x \leq t \leq TE + T_x$) is given by:

$$S(\tau, G_y, z_1) = A \iiint \rho(x, y, z) \delta(z - z_1) e^{i\gamma[(\omega_0 + \gamma G_x x)\tau + (G_y y T_y)]} dx dy dz \quad (6.1)$$

where A is a proportionality constant, $\rho(x, y, z)$ is the proton density, $G_y = p\Delta G_y$ ($p \in [-N_p/2, N_p/2 - 1]$ with N_p being the number of phase encode lines (see Chapter 2) and ΔG_y the incremental phase encode gradient values. Slice selection is modeled here by the δ function. In the presence of field inhomogeneities and gradient non-linearities, the slice selection modeled by $\delta(z(x, y, z) - z_1)$ is replaced by $\delta(z'(x, y, z) - z_1)$ where $z'(x, y, z)$ is defined as:

$$z' = z + \frac{\Delta B_0(x, y, z)}{G_z} + \frac{\Delta B_{G_z}(x, y, z)}{G_z} \quad (6.2)$$

In Eqn 6.2, ΔB_0 is the inhomogeneity of the static field (this term incorporates the object-induced and system-related imperfections in the static field B_0), and ΔB_{G_z} denotes the non-linearity of the slice-select gradient.

B_0 field inhomogeneity and gradient non-linearities also lead to undesired components being added to the phase of the protons at (x, y, z) . The dephasing due to the undesired components develops as time increases in either direction away from the centre of the spin-echo signal with the perturbed phase given by:

$$\Phi'(x, y, z, n, p) = \Phi(x, y, z) + \gamma(\Delta B_0 + \Delta B_{G_x})n\Delta t + \gamma p \Delta B_{G_y} T_y \quad (6.3)$$

where $\Phi(x, y, z)$ is the unperturbed phase given by the term in the exponent of Eqn. 6.1, $n \in [-N_s/2, N_s/2-1]$ (with N_s being the number of time samples with a time interval Δt), ΔB_{G_x} and ΔB_{G_y} are both functions of x , y and z , and are the non-linearities in the read-out and phase-encoding directions. It can be shown that after Fourier transformation of the perturbed signal and with the appropriate change of integration variables, the relationship between the resultant distorted image $I_d(x, y, z)$ and the correct image expected $I_t(x, y, z)$ is given by the relationship [128]:

$$I_t(x, y, z) = I_d(x + \Delta x, y + \Delta y, z + \Delta z) J(x + \Delta x, y + \Delta y, z + \Delta z) \quad (6.4)$$

where $J(x + \Delta x, y + \Delta y, z + \Delta z)$ is the Jacobian of the transformation, and $\Delta x(x, y, z)$, $\Delta y(x, y, z)$, and $\Delta z(x, y, z)$ are the spatial distortions. The Jacobian is used to compensate for the effect of a given slice being stretched or compressed into a different volume thereby altering the apparent proton density and hence image regional intensity. This Jacobian is defined by:

$$J(x,y,z) = \begin{vmatrix} 1 + \partial\Delta x/\partial x & \partial\Delta x/\partial y & \partial\Delta x/\partial z \\ \partial\Delta y/\partial x & 1 + \partial\Delta y/\partial y & \partial\Delta y/\partial z \\ \partial\Delta z/\partial x & \partial\Delta z/\partial y & 1 + \partial\Delta z/\partial z \end{vmatrix} \quad (6.5)$$

This change of variables is given by Eqn 6.2 for the z variable and Eqns. 6.6 and 6.7 below for the x and y variables:

$$x_1 = x + \frac{\Delta B_0(x,y,z)}{G_x} + \frac{\Delta B_{G_x}(x,y,z)}{G_x} \quad (6.6)$$

$$y_1 = y + \frac{\Delta B_{G_y}(x,y,z)}{G_y} \quad (6.7)$$

where (x_1, y_1) is the positions of the displaced image. From Eqns 6.6 and 6.7, it can be seen that for spin-echo imaging the geometrical distortions which bring about intensity distortions in the read-out direction are caused by both static field inhomogeneity and the non-linearity of the read-out gradient. In the phase-encoding direction, the distortions come solely from the non-linearity of the phase encode gradients. Therefore, knowledge of $(\Delta B_0, \Delta B_{G_x}, \Delta B_{G_y}$ and $\Delta B_{G_z})$ allows correction of all image distortions.

6.2.2 Methods

6.2.2.1 Mapping of Spatial Distortions

To be able to map the distortions due to the inhomogeneity in the B_0 field and the non-linear gradients, a grid phantom composed of rectangular containers with known dimensions was made with the overall dimensions of the phantom larger than that of the magnet's recommended imaging volume (cylindrical length < 75 mm and diameter < 90 mm). The phantom spanned a diameter of ~100 mm in the transverse direction and a

length of ~95 mm in the axial direction. The rectangular tubes were filled with gels made with gelatin of approximately the same concentration as used in the polymer gel dosimeters used in this study (described later in chapter 7). The purpose of gelatin was to eliminate or reduce any distortions from sample induced inhomogeneities in the static field. In this chapter, all subsequent reference to x , y and z follow the static coordinate system shown in Fig. 6.1, which were set up for the measurements and calculations of these distortions. G_x , G_y , and G_z represent the physical imaging gradients and also follow the coordinate system shown in Fig. 6.1.

A MEMS sequence similar to that used to generate R_2 maps described in Chapter 7, was modified to acquire four sets of images for the transverse (x,y) imaging direction and two sets for the coronal direction. For the transverse orientation, the first set of images I_1 were acquired with the read-out gradient in the x -direction and the second set I_2 with the read-out gradient direction in the $-x$ direction (i.e. reversed) as shown by the images in Fig. 6.2. The third and the fourth sets (I_3 and I_4) were just a repetition of sets one and two but with the roles of the G_x and G_y gradient interchanged. The fifth and sixth sets were coronal images oriented such that the z gradient was long the read-out direction (forward and reverse directions). This sequence was implemented at 1.89T (Magnex Scientific, Abingdon, Oxon, England) using a 120 mm internal diameter transmit/receive birdcage coil (Morris Instruments Inc. Ottawa). The following parameters were used: TR = 2000 ms, TE = 40 ms, FOV = 128 mm scanned with a matrix size of 256 x 256, 4 averages and 19 slices for given imaging directions each of thickness 5 mm.

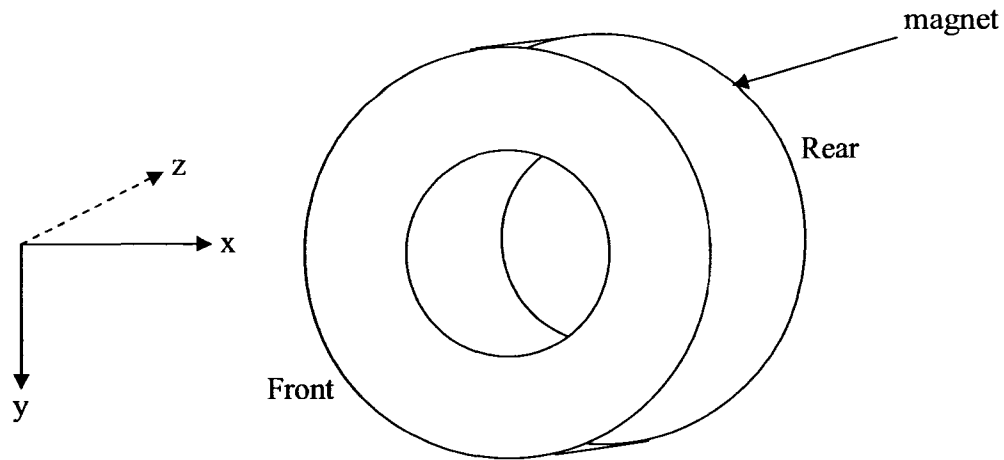


Fig. 6.1: The coordinate system (static) used for the experiments and calculations in this chapter. The $(0,0,0)$ coordinate is assumed to be at the isocentre of the magnet.

These transverse images (17 of the 19) provided the $\Delta x(x,y,z)$ and $\Delta y(x,y,z)$ distortion maps, while the coronal images provided the $\Delta z(x,y,z)$ distortion map as well as $\Delta x(x,y,z)$. The derivation of these distortion maps $\Delta x(x,y,z)$, $\Delta y(x,y,z)$ and $\Delta z(x,y,z)$, from the acquired spin echo images is simply given by the difference between the positions of the corners of the rectangular tubes in a given image from their true position. The corners of the rectangular tubes in the phantoms were determined by using a Matlab (Matlab 6.5, The Matworks Inc. USA) edge-detection algorithm with a threshold (based on the mean signal of the imaged tubes) applied to remove the influence of noise. This means each tube provided four data points given by its angled corners which as a result gave a total of at least 150 data points per image. As for the true position of the edges or corners, this was obtained by taking the arithmetic average of its position in the forward and reverse gradient images (either I_1 and I_2 respectively or I_3 and I_4 respectively). The “averaging” method used to obtain the true dimensions was tested using an algorithm written to adjust the dimensions of any rectangle that did not exactly fit the known physical dimensions and was found to have little or no effect.

This method of deriving the $\Delta x(x,y,z)$, $\Delta y(x,y,z)$, and $\Delta z(x,y,z)$ distortions can also be used to remove the B_0 inhomogeneity, ΔB_0 , from the distortion maps (as described in section 6.2.2.3). The I_3 and I_4 images used to obtain the B_0 inhomogeneity and the non-linear gradient field distributions for the subsequent correction of R_2 maps since these non-linearities could affect the R_2 values estimated from MEMS acquired images depending on the magnitude of the non-linearity.

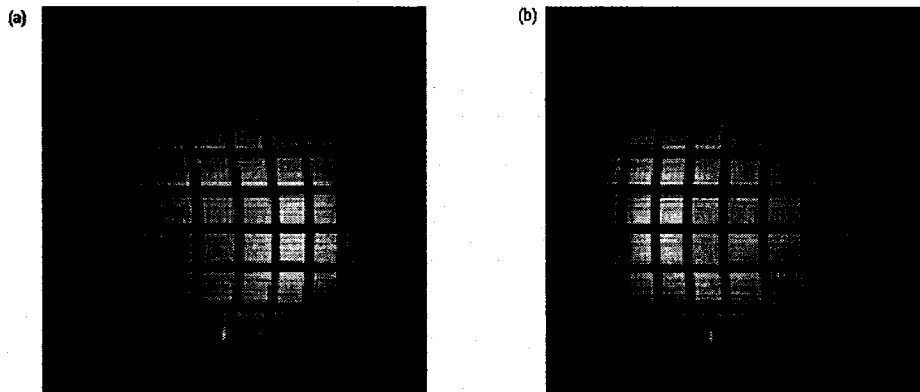


Fig. 6.2: Two spin-echo images acquired with the orientation of the read-out gradient in (a) negative and (b) positive direction. The true position of the edges or the corners in the image is the arithmetic average of the position of the edges or angled corners in both images.

6.2.2.2 Correction of Spatial Distortions

Most distortion and signal intensity correction schemes described in the literature [74,127-132] use only approximations based on two variable polynomials with interpolation and/or extrapolation for slices for which no distortion data is acquired. In the correction scheme used in this work, the inconvenience and possible errors due to approximation from interpolation/extrapolation was avoided by using a three variable

continuous function. These distortion data were fitted by a three variable (x,y,z) polynomial which for the $\Delta x(x,y,z)$ distortion was given by:

$$\Delta x(x, y, z) = \sum_m \sum_n \sum_k a_{mnk} x^k y^n z^m \quad (6.8)$$

where a_{mnk} are the coefficients of the polynomial to be fitted for. The other distortions $\Delta y(x,y,z)$ and $\Delta z(x,y,z)$, were also fitted to a similar polynomial. A non-linear least-squares fit method was used to estimate the a_{mnk} coefficients (Matlab 6.5, The Mathworks Inc. USA). From the estimated distortions, the images were corrected for the effects of the static inhomogeneity and gradient non-linearity by simply using an interpolation algorithm. After interpolation, the images were scaled by the intensity factor given by the Jacobian defined in Eqn. 6.5.

6.2.2.3 Estimation of Change in Gradient Fields

The B_0 inhomogeneities, ΔB_0 , and the gradient field non-linearities ΔB_{G_x} , ΔB_{G_y} and ΔB_{G_z} were estimated from the Δx , Δy and Δz distortion maps. The ΔB_0 , ΔB_{G_x} and ΔB_{G_y} distributions were estimated from the set of four transverse images described above via these distortion maps (Eqn 6.8). From images I_1 and I_2 and using Eqns 6.6 and 6.7 the following relationships were used [128]:

$$\Delta B_0(x, y, z) + \Delta B_{G_x}(x, y, z) = G_x \Delta x(x, y, z) \quad (6.9a)$$

$$\Delta B_{G_y}(x, y, z) = G_y \Delta y(x, y, z) \quad (6.9b)$$

From images I_3 and I_4 :

$$\Delta B_0(x, y, z) + \Delta B_{G_y}(x, y, z) = G_y \Delta x'(x, y, z) \quad (6.10a)$$

$$\Delta B_{G_x}(x, y, z) = G_x \Delta y'(x, y, z) \quad (6.10b)$$

From Eqns 6.9 and 6.10, the distribution of the B_0 inhomogeneity and gradient non-linearity were:

$$\Delta B_{G_x}(x, y, z) = G_x \Delta y'(x, y, z) \quad (6.11)$$

$$\Delta B_{G_y}(x, y, z) = G_y \Delta x'(x, y, z) \quad (6.12)$$

$$\Delta B_0(x, y, z) = G_x [\Delta x(x, y, z) - \Delta y'(x, y, z)] \quad (6.13)$$

The ΔB_{G_z} distribution was estimated from the coronal images using Eqn. 6.2 and the estimated ΔB_0 of Eqn 6.13.

6.3 Results and Discussion

6.3.1 Mapping of Spatial Distortions

Fig. 6.3 shows sample distortion maps of Δx and Δy obtained for a transverse slice located at -35 mm from the magnet's isocentre. In Fig. 6.3, Δx distortions of up to 10 mm were observed in the images or the maps obtained due to the combined effects of B_0 inhomogeneity and gradient non-linearity. At this same location on the magnet's axis, Δy distortions of about 2 mm were measured as shown in Fig. 6.3(b). The Δx and Δy distributions shown in Fig. 6.3 (a) and (b) are from the read-out and phase-encode directions of a transverse image with read-out and phase-encode gradient in x and y directions respectively. Distortions of up to 13 mm were measured for transverse image slices acquired at $z = \pm 45$ mm of the isocentre.

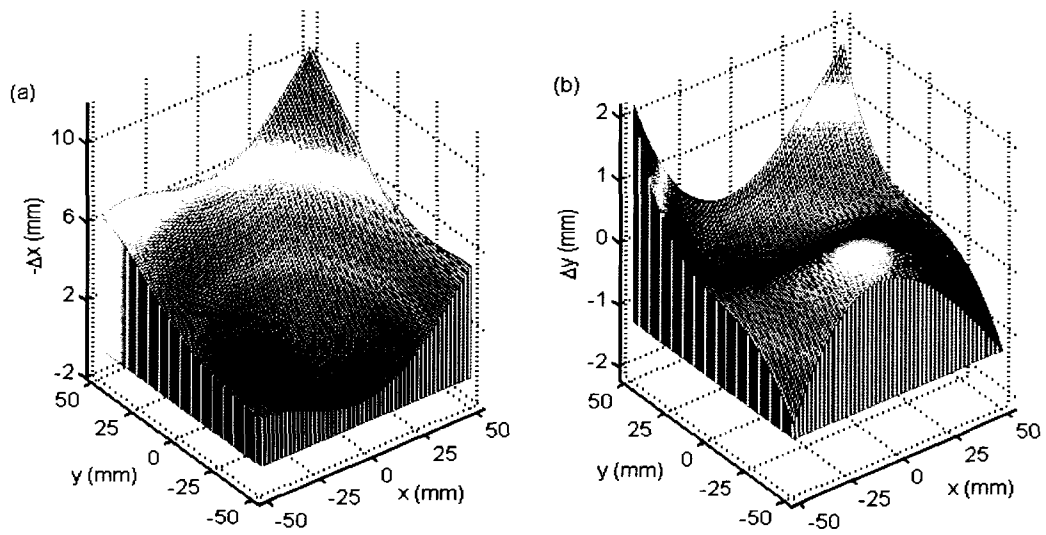


Fig. 6.3. Distribution (or map) of (a) $\Delta x(x,y,z)$ and (b) $\Delta y(x,y,z)$ obtained from a transverse slice located at $z = -35$ mm of the magnet's isocentre.

Fig. 6.4 shows distortion Δz distortion map obtained from a coronal slice located at $y = -25$ mm of the isocentre. The coronal image taken was such that the read encode gradient

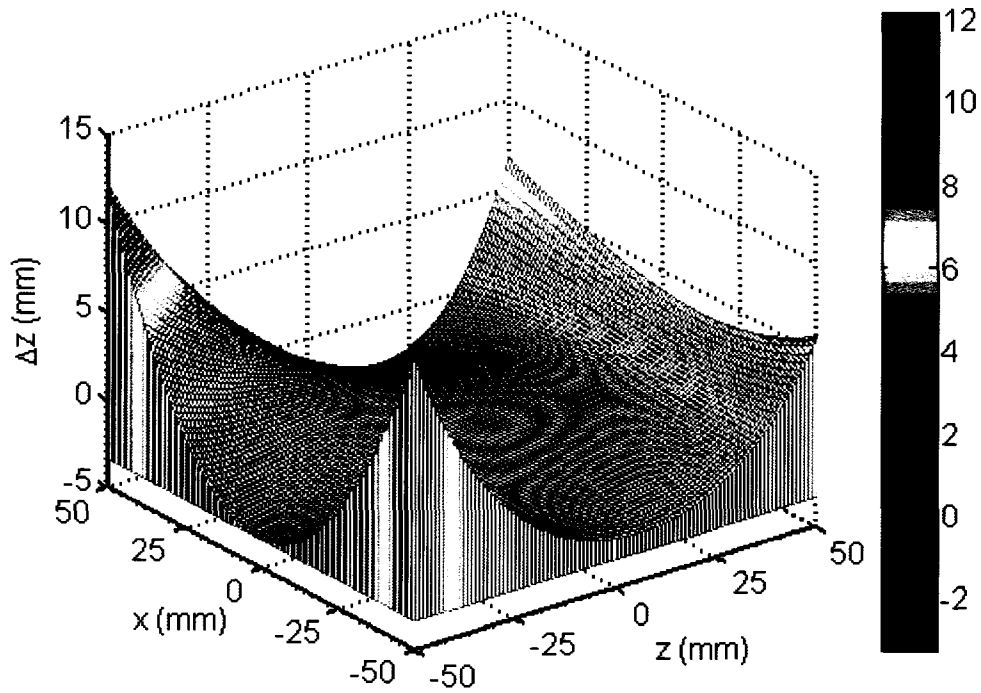


Fig. 6.4. Distribution (or map) of $\Delta z(x,y,z)$ obtained from a coronal slice located at $y = -25$ mm from the magnet's isocentre. The scale represents the degree of spatial distortions.

was oriented in the same direction as the physical z- axis of the magnet. This Δz mapping was done for all the coronal slices acquired.

6.3.1 Correction of Spatial Distortions

The measured distortion data, were fitted to a three variable polynomial given in Eqn. 6.7. These estimated continuous functions were then used to correct the distorted images by interpolation. For transverse images (xy-plane) acquired within $z = \pm 25$ mm of the isocentre, a 3rd-order polynomial (with 20 coefficients estimated) was sufficient to correct the distortions in the images. However, this 3rd-order polynomial was insufficient to correct the transverse images acquired at $z > 25$ mm, thus a 4th-order polynomial was used instead, which was found to be sufficient to correct the distortions within $z = \pm 45$ mm. Fig. 6.5 (a) shows a sample transverse distorted image and (b) its corresponding corrected image taken at $z = -35$ mm from the isocentre of the grid phantom. Fig. 6.6

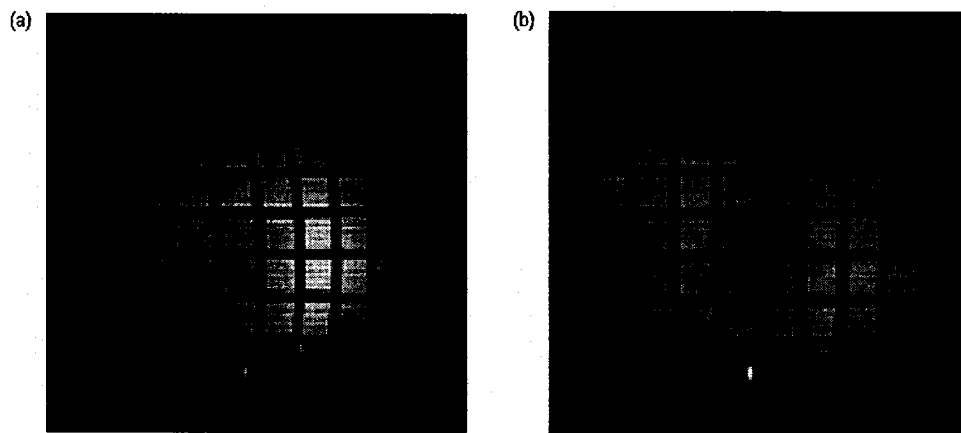


Fig. 6.5. Sample (a) distorted and (b) corrected transverse images acquired at $z = -35$ mm of the magnet's isocentre. The corrected image has also been corrected for the intensity non-uniformity due to spatial distortions using the Jacobian (see Eqn 6.4).

shows the correction of a transverse circular (xy-plane) image of a cylindrical phantom acquired at $z=-35$ mm from the isocentre using the estimated function. The correction algorithm was able to correct distortion in images of the phantom to within 1 mm of its true diameter (95 mm). For this 4th-order polynomial, a total of 35 coefficients were estimated with residual values within 40 for the Δx , Δy and Δz distortions. A residual of 35.8 was produced for $\Delta x(x,y,z)$; 31.1 for $\Delta y(x,y,z)$ and 6.5 for $\Delta z(x,y,z)$ from a set of ~ 2000 data points per distortion direction. The fit using the continuous polynomial function permitted easier correction of slices (for spatial and intensity distortion) for which no distortion data were acquired, thereby avoiding possible errors due to approximations from interpolation and/or extrapolation. This continuous function allows for correction of both 2-D multi-slice images and 3-D images. In fact, slices for which no distortion data were acquired were successfully corrected using the estimated function. A summary of the polynomial terms and their corresponding estimated coefficients are given in Appendix A.

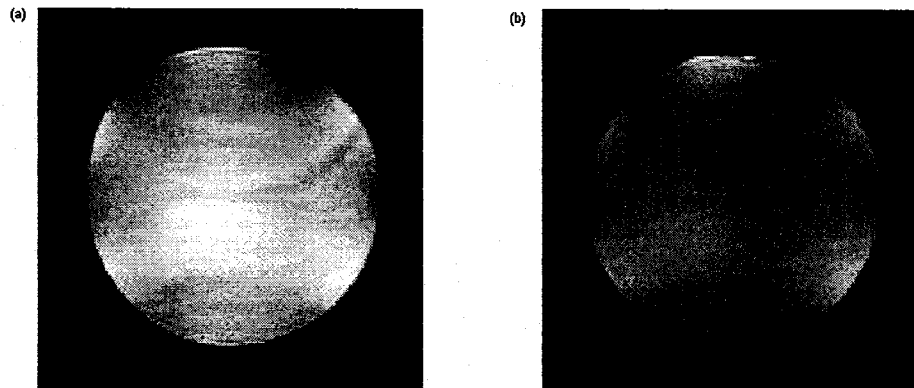


Fig. 6.6. (a) Distorted and (b) corrected (spatial and intensity) images taken of a cylindrical phantom at $z = -35$ mm from the isocentre.

Fig. 6.7 shows a sample map of the Jacobian values used to correct the intensity “distortions” of transverse images acquired at an axial location $z = -35$ mm. Locations without any intensity “distortions” have Jacobian values of unity.

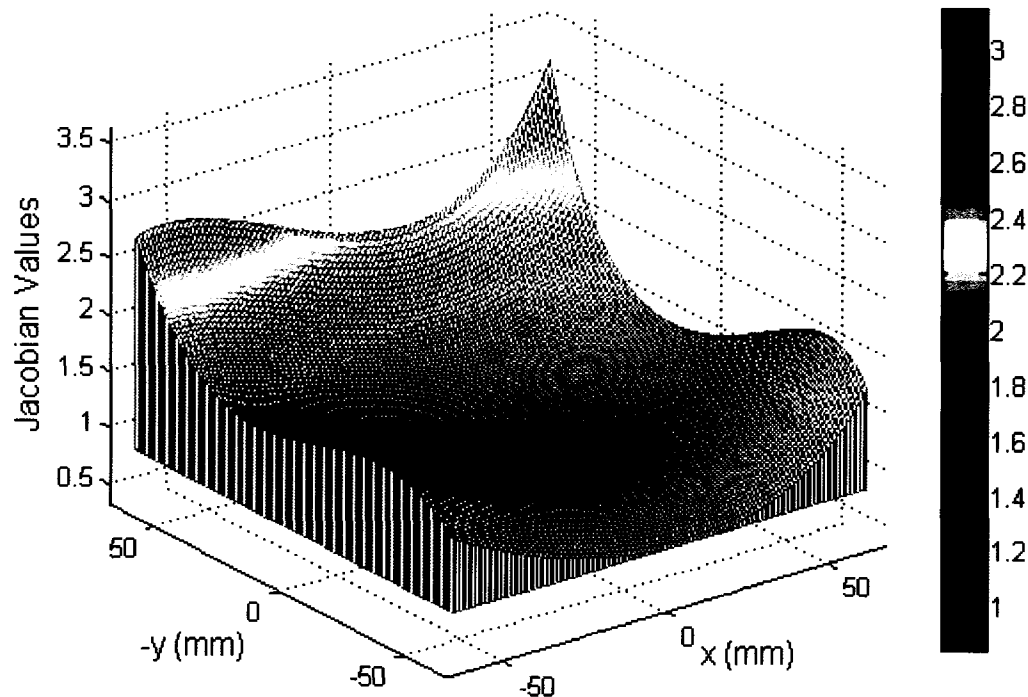


Fig. 6.7: A map of Jacobian values used to correct intensity “distortions” in transverse images acquired at $z = -35$ mm.

6.3.2 Estimation of Change in Gradient Fields

Figs. 6.8 (a), (b), (d) show the behaviour of the gradient non-linearities of the x, y and z imaging gradients respectively at $z = -35$ mm. Fig. 6.8 (c) shows the static field inhomogeneity at this same location. This non-linearity of MR imaging gradients (generated for the whole imaging volume) has an influence not only on the estimation of diffusion coefficients (or tensors) when doing diffusion imaging but can also have an influence on the estimated $R_2 (= 1/T_2)$ values derived from multiple spin echo baseline

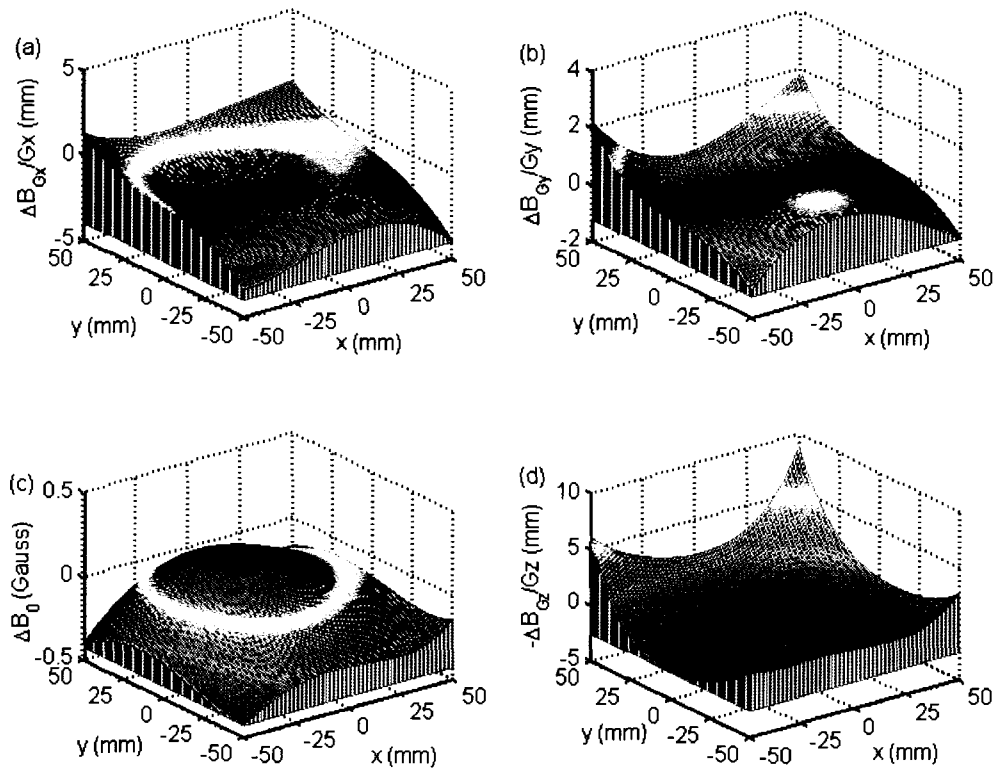


Fig. 6.8. The measured non-linearity of the (a) x gradient, (b) y gradient, (c) static field inhomogeneity and (d) z gradient at $z = -35$ mm from the isocentre. The x and z gradient non-linearity plots have been corrected for the static field inhomogeneity.

images. Thus the estimation of these field inhomogeneities for all the slices acquired enables subsequent (see chapter 7) checking and correction of any changes in the estimated R_2 maps, which would also affect the derived dose maps (for gel dosimetry) .

6.4 Conclusion

In this chapter, a description is provided for the design of a simple gel-filled phantom and for the mapping of spatial distortions due static field inhomogeneities and

gradient non-linearities. The dimensions of this phantom were made such that it enclosed the imaging volume normally used and large enough to cover the dimensions of the gel phantoms to be used for dosimetric studies (Chapter 7). From the distortion maps generated, distorted images were corrected not only for the spatial distortions but also for signal intensity “distortions” that result from the gradient non-linearity measured. Static field inhomogeneity and gradient field non-linearity maps were then derived from these distortion maps which can be used to check for the possible influence of these non-linear gradient fields on estimated R_2 maps.

Chapter 7

Dose Distribution Verification Using Two New Polymer Gel Dosimeters with Reduced Toxicity and MR Imaging

7.1 Introduction

One of the steps involved in radiotherapy treatment planning, is computer dose planning to optimize the radiation delivery. This computed treatment plan distribution needs to be verified by an accurate dose verification technique. To date, dose distribution verification has mostly been done by methods such as thermoluminescent dosimeters (TLDs), ion chambers, and films amongst others. These methods all suffer from the fact that they are not inherently three-dimensional (3-D) in nature, thus there has been a lot of interest in the use of imaging for gel dosimetry which can provide 3-D information as a dose verification tool in clinics. One the most reliable forms of gel dosimeters investigated so far has been the polyacrylamide gel (PAG) dosimeter gel which has the disadvantage of being very toxic. A current area of research is the development of polymer gel dosimeters with reduced toxicity. Two such polymer gel dosimeters have been developed at the Kingston Regional Cancer Centre, KRCC have been developed by replacing acrylamide with the less harmful monomers diacetone acrylamide (DAAM) and *N*-isopropylacrylamide (NIPAM) [136]. In this study our aim was to investigate the feasibility of using these two gel formulations as a dose verification tool for conformal therapy. The aim was to develop a dosimeter which could be read not only by MR but

also by optical computed tomography (CT) as well. These two gel dosimeters were irradiated according to a treatment planning system to obtain a desired dose distribution. This treatment planned dose distribution was verified by comparing it to the MR dose maps. The MR dose maps were then compared directly to the optical CT obtained dose distributions.

7.2 Methods and Materials

7.2.1 Gel Preparation

The two gel dosimeters included two monomers DAAM and NIPAM and the conventional cross-linker *N,N'*-methylene-bis-acrylamide (commonly referred to in gel dosimetry circles as “Bis”) and the antioxidant tetrakis (hydroxymethyl) phosphonium chloride (THPC). The addition of THPC ensured convenient preparation of the gels under normoxic conditions. The preparation of these gel dosimeters were all done at KRCC according to a procedure described in the publication by *Senden et al* [136]. These gels were then put in four cylindrical containers (2 for diacetone acrylamide and 2 for isopropylacrylamide) with each having a diameter of approximately 94 mm and length of ~100 mm.

The preparation of these gel dosimeters was done in a fume hood and under normoxic conditions to produce a 6%T (percent weight fraction of the gel that is Bis and monomer), 50%C (percent weight fraction of Bis and monomer that is Bis) recipe. Gelatin (300 Bloom Type A) was allowed to swell in 80 % of de-ionized water at room temperature before being heated to a temperature of 50°C. Under continuous stirring,

3%wt Bis was dissolved at 50°C, with complete dissolution taking about 15 min. This was followed by the addition of the same amount of monomer (DAAM or NIPAM) after the gelatin – crosslinker (Bis) mixture had cooled to ~37°C. Lastly, the remaining 20 % of the water was used to prepare a solution of the anti-oxidant THPC (1.98g) and added to the gel solution at this temperature. These gel solutions were then transferred to the cylindrical phantoms and stored in the refrigerator.

7.2.2 Treatment Planning and Irradiation

The gel-filled phantoms were irradiated a day after preparation with a Cobalt-60 benchtop tomotherapy unit [87] mounted on a T-780C unit (Theratronics, Kanata ON). These phantoms were placed at the center of a remotely-controlled turn-table and irradiated using 1cm x 1 cm pencil beams with the gantry rotated at 90°. Using custom-built software in Custom Labview (National Instruments Corporation) by the KRCC Medical Physics group, these phantoms were appropriately rotated while in the path of the beam to obtain desired treatment plan shapes. The treatment plan system (TPS) used was originally conceived as a matrix in Excel (Microsoft Corp.) and has been verified by the KRCC Medical Physics group using custom-built software in Matlab (Mathworks Inc). Previous polymer gel dosimeter phantom irradiations using these treatment plans and scanned using optical CT have also been validated [87]. The treatment-planned irradiation was done to obtain a conformal “K” shape in all the 4 phantoms. For the DAAM and NIPAM monomer filled phantoms, two phantoms (one for each of the monomer types) were irradiated to a maximum dose of ~200 cGy and the other two to a

maximum dose of ~500 cGy. A calibration treatment plan pattern was also done in these phantoms as described in the “Dose Calibration and Dose Maps” section below.

7.2.3 MR Imaging and Optical CT Scanning

After irradiation, the gel phantoms were stored in a refrigerator for 3 days (for the gels to stabilize [136]), these phantoms were taken out of the fridge and placed in the magnet room for ~24 hours in order to allow the gel to reach thermal equilibrium. MRI scans were then performed on the gel phantoms using the multi-echo multi-slice spin-echo (MEMS) sequence described in Chapter 5. MR imaging was performed at a static field strength of 1.89T (Magnex Scientific, Abingdon, Oxon, England) and images were acquired with the aid of a transmit/receive birdcage coil (Morris Instruments Inc. Ottawa) having a 12 cm internal diameter. The MEMS sequence had the following variables; TE = 40 ms, 26 equidistant echoes, and 17 slices with slice thicknesses of 5 mm each. A 128 mm field of view was used with the matrix sizes chosen to give a spatial resolution of 1 mm x 1 mm x 5 mm with 2 averages taken per scan. As indicated in Chapter 5, a corresponding B_1 map was acquired for each MEMS slices imaged for later correction of R_2 ($= 1/T_2$) for any effects due to B_1 inhomogeneity. The baseline images were then transferred to a personal computer where B_1 -corrected R_2 maps were obtained from 23 of the 26 MEMS images.

Optical scanning of these gel phantoms was done by the KRCC Medical Physics group at the Kingston Regional Cancer Centre, Ontario on a cone-beam CT scanner (Vista Scanner, Modus Medical Devices London, ON). The technology of optical CT scanning employed in this scanner is analogous to first generation x-ray CT, except that a

visible light source is used instead of an x-ray source. A more detailed description of this optical CT scanner is provided in *Schreiner et al* [87].

7.2.4 Data Analysis

7.2.4.1 Dose Calibration and Dose Maps

The R_2 images or maps were converted to dose maps using a linear calibration factor obtained for each gel phantom. Due to the fact that significant temperature changes occur within gel dosimeters during irradiation and thermal history effects during MR scanning on dose response have been observed [137, 138], the use of vessels of different size and geometry from the calibration phantoms would not seem to be appropriate. As a result we used the irradiation of a treatment planned calibration triangular pattern within each gel phantom to minimize the effects mentioned above. From these R_2 images containing the calibration triangle, a linear calibration curve was obtained which was then used to convert all the R_2 fitted maps obtained to dose maps.

Any non-uniformity imposed on the R_2 maps due to the gradient field non-linearity measured (Chapter 6) was also investigated. This is based on the well-known fact that the Brownian motion of water molecules in the presence of strong magnetic field gradients can cause the MR signal to be attenuated [135]. This gradient field non-linearity, if strong enough, would cause the various echo signals to be attenuated differently for multiple spin-echo sequences and thereby could lead to a change in the measured R_2 values estimated from the baseline images. This change in R_2 due to the combined effect of strong gradient fields and the self diffusion of water molecules is based on the relationship:

$$R_{2_nlingd} = R_{2_lingd} + \frac{bD}{TE} \quad (7.1)$$

where D is the molecular self-diffusion coefficient of water in the presence of magnetic field gradients, TE is the echo time, R_{2_lingd} and R_{2_nlingd} are the R_2 of the sample with linear and non-linear gradient field effects respectively. The b -value (also known as the b-factor) is a diffusion weighting factor defined as:

$$b(TE) = \gamma^2 \int_0^{TE} \left(\int_0^{\tau} G(t) dt \right)^2 d\tau \quad (7.2)$$

where $G(t)$ is the time dependent gradient field strength. Using the non-linear gradient field maps measured in Chapter 6 and combined with expressions of b -factors for the MEMS sequence [55] with a typical diffusion coefficient of $1.66 \times 10^{-9} \text{ m}^2\text{s}^{-1}$ [55] for polymer gels, no significant change in R_2 was observed due to these non-linear gradients.

7.2.4.2 MRI and Optical CT Gamma Maps

The verification of treatment plan dose distributions required the comparisons of measured and calculated dose distributions. The criterion for acceptable calculation performance for treatment plan verification is generally defined as a tolerance of the dose and distance-to-agreement (DTA) in regions of low and high dose gradients respectively. The γ index developed by *Low et al* [139] unifies dose distribution comparisons using the acceptance criteria. The multidimensional distance between the measurement and calculation points in both the dose and the physical distance, scaled as a fraction of the acceptance criteria, is taken as the measure of the treatment planning system validation. Thus this γ index is defined as the minimum radial distance between the measurement

point and the calculation points (expressed as a surface in the dose-distance space) [139].

Mathematically this γ index is defined as [139]:

$$\gamma(r_m) = \min\{\Gamma(r_m, r_c)\} \forall \{r_c\} \quad (7.3)$$

where

$$\Gamma(r_m, r_c) = \sqrt{\frac{r^2(r_m, r_c)}{\Delta d_M^2} + \frac{\delta^2(r_m, r_c)}{\Delta D_M^2}}, \quad (7.4)$$

$$r(r_m, r_c) = |r_c - r_m|, \quad (7.5)$$

and

$$\delta(r_m, r_c) = D_c(r_c) - D_m(r_m) \quad (7.6)$$

Eqn.7.6 represents the difference between the calculated and the measured dose respectively, where r_c and r_m represent the spatial location of the calculated and measured distributions respectively while ΔD_M is the dose difference criterion and Δd_M is the DTA criterion set. The pass-fail criteria is set such that $\gamma(r_m) \leq 1$, means the calculation passes and $\gamma(r_m) > 1$ means the calculation fails.

For all the dose maps obtained by either MR imaging or optical CT, a γ map was calculated between the MR and the treatment plan dose distribution, between the optical CT and treatment plan and finally between the MR and optical CT dose maps. All the optical dose maps were done by the Medical Physics group at the Kingston Region Cancer Centre, Ontario. The acceptance criteria used in the calculation of the gamma maps was a dose difference of 3 % and a DTA of 3 mm; values used at the Kingston Regional Cancer Centre and typically used in most clinics.

7.3 Results and Discussion

7.3.1 Dose Calibration and Dose Maps

Fig. 7.1 (a) and (b) show the calibration (triangle) R_2 image and the corresponding treatment plan image with isodose contours overlaid on the image for the *N*-isopropylacrylamide monomer dosimeter with a maximum dose of ~500 cGy. Fig. 7.1(a) and (b) provided the calibration curve used to convert the R_2 images of all the gel

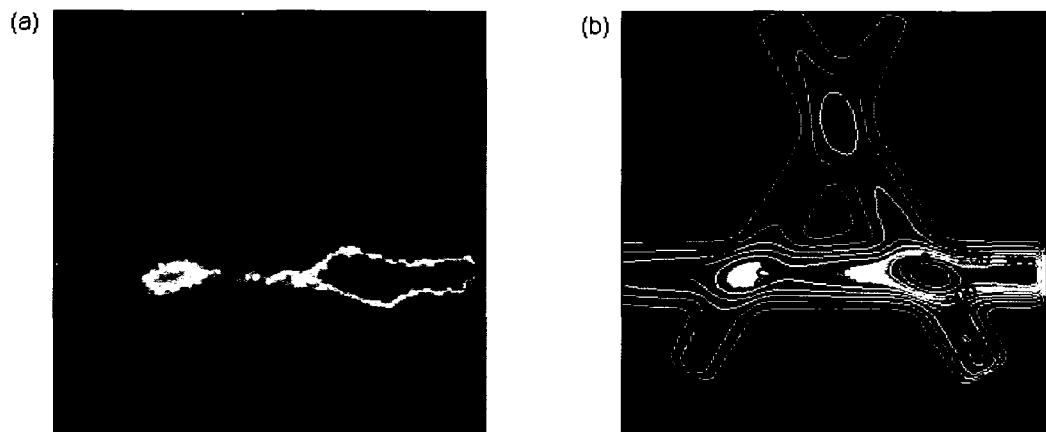


Fig. 7.1: Calibration triangle (a) R_2 image for the NIPAM monomer dosimeter and (b) corresponding treatment plan used to irradiate the phantom. The 100, 200, 300 and 400 cGy isodose contours are overlaid on the treatment plan image.

dosimeter phantoms to dose maps. The R_2 image was acquired with a 128 mm field of view (FOV) and a matrix size of 128 x 128. From Fig. 7.1 a calibration curve was then generated by drawing ROIs (regions of interest ~15 pixels) in quite uniform areas on the treatment plan image to calculate the mean dose value and the corresponding mean R_2 values from the R_2 maps. These values were then used to generate a calibration curve. Fig. 7.2 shows a typical calibration curve from the NIPAM monomer filled gel dosimeter

which had been irradiated with a maximum dose of ~ 500 cGy with a dose response of $0.0007 \pm 0.0001 \text{ s}^{-1}\text{cGy}^{-1}$ ($r^2 = 0.9988$). The error bars shown represent one standard deviation of the R_2 values from the ROI drawn. The possible non-uniformity on the estimated R_2 maps due to the gradient non-linearity measured was investigated using Eqn. 7.1 and no significant change in the R_2 maps was observed.

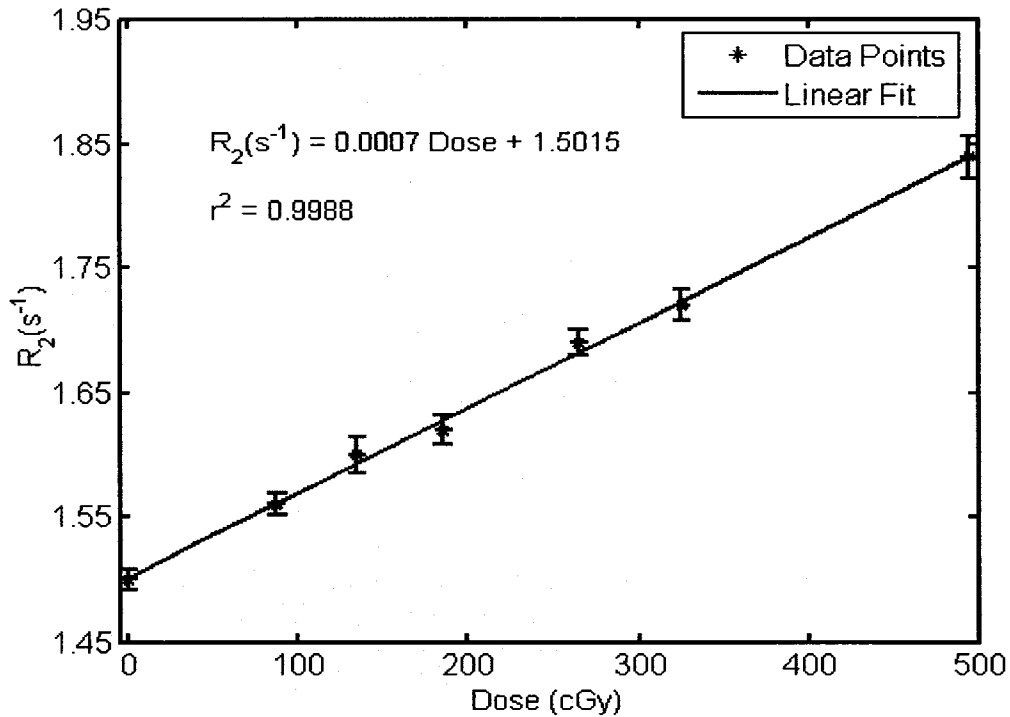


Fig. 7.2: A Calibration curve generated from an R_2 image and its corresponding treatment plan image or map for the NIPAM monomer dosimeter in Fig. 7.1.

This procedure for generating calibration curves for the gel phantoms was repeated for all the gel phantoms (one with a maximum dose delivered of ~ 200 cGy and the other with a maximum dose delivered of ~ 500 cGy for both of the gel dosimeter types). From the generated calibration curve or equation, a dose map was then calculated for each of the four gel dosimeter phantoms. As earlier mentioned, the purpose of a calibration triangle in the same gel phantom was based on reducing or limiting the effect of the thermal

history during scanning affecting the dose response if a phantom of a different geometry is used. This would be particularly more prominent if small test tubes or vials are used as calibration phantoms; a practice which is commonly used to generate calibration curves. Small test tubes or vials used for calibration provide a larger surface-to-volume ratio ($\propto 1/\text{radius}$) which facilitates a faster energy exchange and/or re-establishment of a temperature equilibrium within the gel dosimeter (and quicker redistribution of heat due to radiofrequency or RF heating). This means that there may be a difference in dose response between the calibration vial and the gel dosimeter due to temperature. Another method that is commonly used to limit this thermal history effect on dose response is to image the calibration vials at the same time as the phantoms themselves. This method still faces the problem of differences in surface-to-volume ratio discussed above since calibration phantom has a different geometry.

Fig. 7.3 shows the MR-derived dose map for the gel phantom containing the NIPAM monomer that received a maximum dose of approximately 500 cGy. Overlaid on the MR-derived dose image are the isodose contours of 50, 150, 250, 350 and 450 cGy from the treatment plan. This shows good agreement between the measured MR dose map and the treatment plan used for the irradiation. As for the optical CT image data, a similar procedure was followed to obtain the dose images.

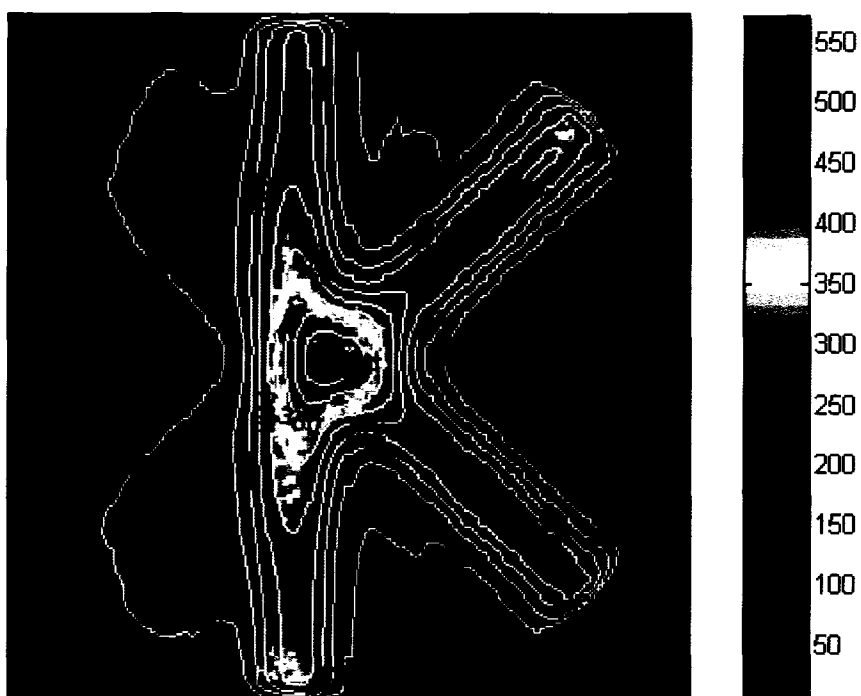


Fig. 7.3. An MR dose map for a gel dosimeter containing the NIPAM monomer irradiated to a maximum dose of ~500 cGy. This MR image was acquired with a matrix size of 128 x 128 and a FOV = 128 mm.

7.3.2 MRI and Optical CT Gamma Maps

Fig. 7.4 shows the gamma index map obtained from the quantitative comparisons of the (a) MR dose map and the treatment plan dose distribution and (b) the MR dose map and the optical CT dose map on a pixel-by-pixel basis for the gel dosimeter phantom containing the NIPAM monomer. Fig. 7.4 shows that within the irradiated treatment planning target region of the “K” symbol, most of the γ values pass the acceptance criteria ($\gamma \leq 1$). Within the phantom image shown in Fig. 7.4 (a), 94 % of the pixels have a value of γ -index less than unity which means measurements by MR and treatment plan calculations meet the acceptance criteria of 3 % dose difference and 3 mm distance-to-agreement adopted. A similar calculation between the dose maps obtained by MR and by

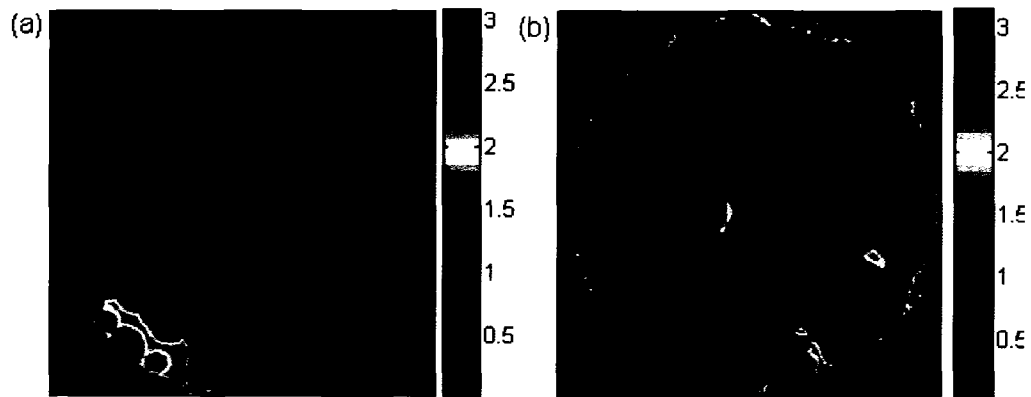


Fig. 7.4: γ -index map between the (a) MRI and treatment plan (b) MRI and optical CT dose maps for a gel dosimeter phantom containing the NIPAM monomer irradiated to a maximum dose of ~ 500 cGy.

optical CT is shown in Fig. 7.4(b) and gave an 81 % value of pixels within the phantom having a γ -index value less than or equal to unity. These percentages went up if a region around the “K” irradiated pattern is defined such that the dose within this region didn’t fall below 10 % of the maximum dose delivered (98.2 % for MR vs TPS and 93.5 % for MRI vs optical CT). Fig. 7.5 shows the comparison between: (a) MR vs the treatment plan dose maps and (b) MR vs optical CT dose maps for distribution irradiation of maximum dose ~ 200 cGy delivered to the phantom. Fig.7.5 (a) shows good agreement between the MR and the treatment plan dose maps but a lesser agreement between the MRI and optical CT dose maps is observed in the γ -index map in Fig.7.5 (b). For the defined region around the “K” irradiated pattern such that the dose was within 10% of the maximum dose, 97.7 % (MR vs TPS) and 86 % (MRI vs optical CT) of the pixels passed the acceptance criteria.

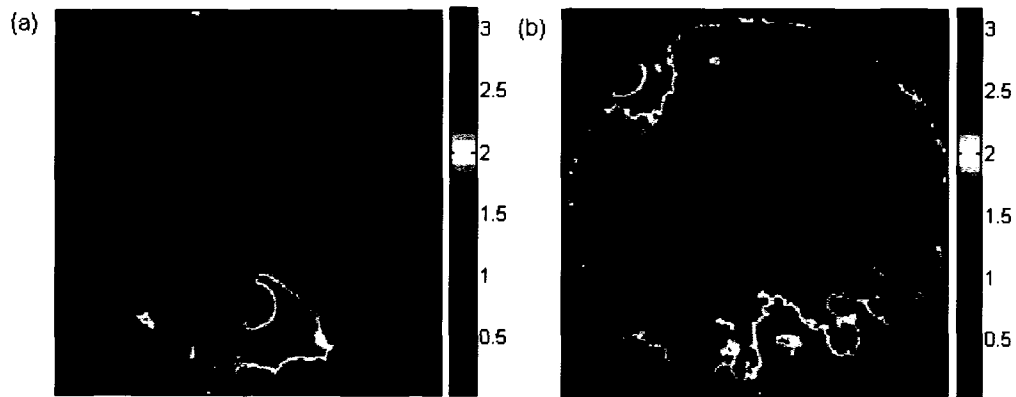


Fig. 7.5: γ -index map calculated for (a) MR vs TPS and (b) MR vs optical CT dose maps (200cGy maximum) for the NIPAM monomer gel dosimeter.

Fig. 7.6 show the γ -index maps for the gel dosimeter containing the DAAM monomer irradiated to a maximum dose of ~ 500 cGy. Good agreement between the MR and the treatment plan system (TPS) maps is seen in Fig. 7.6(a) within the treatment planned area (the “K” symbol). For the MR vs optical CT, the γ -index value map is shown in Fig.7.6 (b), a large area of the γ -index map shows values less than or equal to unity except in a limited region of the image and at the edges of the image, which indicates a good agreement between the dose maps obtained using both methods. For the same region as above defined around the “K” symbol such that the dose doesn’t fall below 10% of the maximum dose delivered, 97.2 % (MR vs TPS) and 94 % (MR vs optical CT) of the pixels had a γ -index value less than or equal to unity.

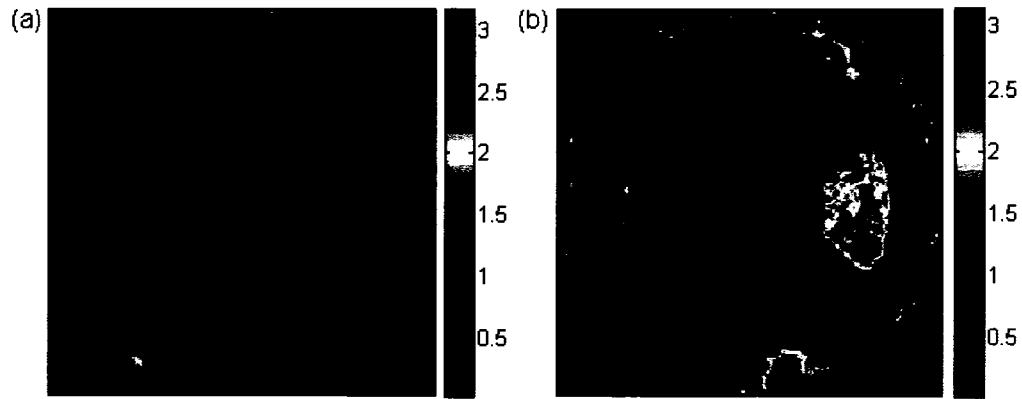


Fig. 7.6: γ -index map calculated for (a) MR vs TPS and (b) MR vs optical CT derived dose maps (500cGy maximum) for the gel dosimeter made from the DAAM.

Fig. 7.7 shows the pixels that pass the acceptance criteria for the DAAM monomer dosimeter (500 cGy) for: (a) MR and treatment plan dose maps and (b) MRI and the optical CT dose maps. The dose distribution delivered was such that maximum dose of approximately 200 cGy was delivered to the gel phantom. Good agreement between the MR and treatment plan dose maps was observed as shown in Fig 7.7(a). Also good agreement between MR and optical CT dose-derived distributions given by the γ -index map is shown in Fig. 7.7(b). For these γ -index maps, approximately 98.1% of the pixels within the defined region around the “K” irradiated pattern such that the dose doesn’t fall below 10% of the maximum dose passed the acceptance criteria. Despite the fact that these DAAM monomer dosimeters show better agreement between the TPS and the MRI dose maps, they showed a smaller MR dose response (factor of ~ 2.5 smaller) compared to the NIPAM monomer dosimeters. This was such that the irradiated “K” pattern in the MR dose gel image was not as clearly distinguishable from the background region as was the case with the NIPAM monomer dosimeters. The enhancement at the edges of the image or phantom seen earlier is also clearly visible in Fig. 7.7 (b). This is

possibly due to significant refraction artifacts near the edges of the container from the optical CT images [141]. In fact, the optical CT-derived dose maps or images showed an enhancement at the edges of the phantom images unlike the MR-derived dose maps.

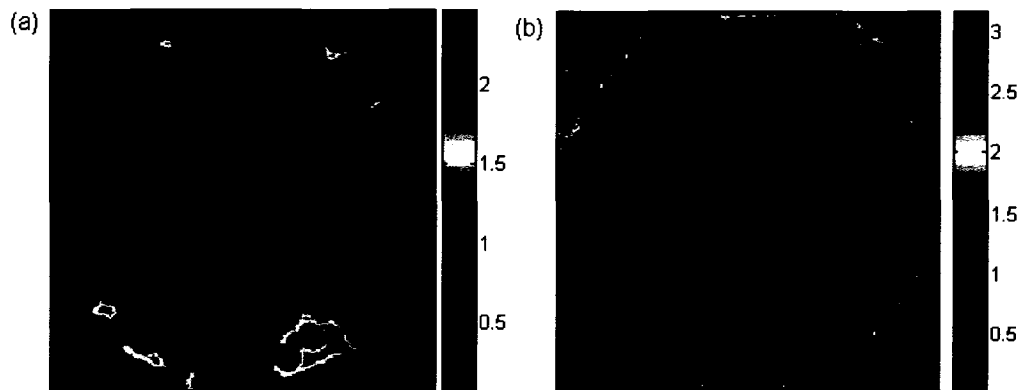


Fig. 7.7: γ -index map for (a) MRI vs TPS and (b) MR vs optical CT dose maps (200cGy maximum) for the DAAM monomer gel dosimeter.

The comparison between the MR and the optical CT derived dose maps doesn't seem to conform very well with each other as compared to the comparison between the treatment plan map and the MRI dose map. This is observed especially for the dosimeter phantoms containing the NIPAM monomer. This might come from slight misalignment of the pair of images, scattering in the dosimeter when the optical CT images were being acquired amongst others. Other artifacts common with optical CT images which could have had an influence on the performance shown in the γ -index map between MR and optical CT dose map could be: strong refraction artifacts associated with refraction of the laser near the edge of the container(mentioned earlier), geometrical distortion (which has been observed for images acquired using this optical CT scanner), refraction and/or absorption in the gel due to the clarity of the gel for optical CT not being high enough,

and other possible imaging artifacts. Also MR artifacts that could have had an influence on MR dose images are RF-inhomogeneities, and spatial distortions in the R_2 images (although gradient fields and RF-inhomogeneities were actually corrected for as shown in Chapter 5 and Chapter 6).

Despite the relatively low percentage of pixels that meet the acceptance criteria when the MRI and optical CT dose maps (as opposed to MR vs TPS) are compared in this study, a better performance can be obtained if some of the suggested reasons for the low comparative performance between these two systems were addressed. Despite these possible sources of errors influencing the comparative performance of the MR and optical CT dose maps, optical CT provides some advantages over MR in that high spatial resolution and low noise can be achieved because of the high sensitivity of photodiode light detection technology used. Optical CT gel dosimetry can provide a low cost alternative to MR gel dosimetry where the phantoms being imaged doesn't contain opaque objects or the phantoms are of arbitrary shapes which may cause significant artifacts through reflection, refraction and/or high absorbance.

7.4 Conclusion

In this chapter, R_2 maps derived from MR acquired baseline signal images were converted to dose images using a triangular irradiation calibration pattern within the same gel dosimeter phantoms. This was done to limit problems that might affect the estimated R_2 maps from using calibration vials with different geometry and/or having a different thermal history for MR scans done separately. These MRI dose maps were then used to verify the treatment planned dose distribution via γ -index maps which had preset clinical

acceptance criteria. These γ -index maps were also calculated for the comparative performance of the optical CT dose maps against the MRI dose maps.

From the results obtained via the γ -maps, MRI measured gel dose distributions agree well with the calculated (TPS) dose distributions. Given this good correlation, one may assume that these two new low toxicity polymer gel dosimeters successfully verified the calculated dose distribution and that the tomotherapy machine delivery of these planned dose distribution is accurate within $\sim 97\%$. Despite the fact that the correlation (in terms of γ -index maps) between the MR dose maps and the optical CT maps weren't as good as that between the MR and the calculated dose distribution plans, the correlation obtained was still reasonable, indicating that these two dosimeters have some promise as to their use for clinical dose verification using MR and optical CT gel dosimetry.

Chapter 8

Summary and Future Work

8.1 Summary

The eventual complete acceptance and application of gel dosimetry as a clinical dose verification tool in radiotherapy treatment planning will require the continuous development, investigation and research of existing and new gel dosimeters which can meet the target figure of accuracy in high precision radiotherapy (2-3 % of the maximum dose in the regions of uniform dose and a spatial error of less than 2-3 mm in regions of high dose). These gel dosimeters do not only have to come close enough to the target accuracy but also have to offer convenient and easy use.

The most common gel dosimeters are the polymer gel dosimeters which are based on the radiation-induced polymerization of the monomers. The other popular type of gel dosimeter which has slightly lost the attention of most gel dosimetry researchers is the T_1 -based Fricke gel dosimeters. This is mostly because of the: (i) the problem of diffusion of radiation-induced ferric ions thereby destroying or blurring out the desired spatial information, and (ii) the need of an MRI method fast enough such that the loss of spatial information is reduced. A solution to these problems faced by Fricke gel dosimeters could renew interest in these gels as an attractive alternative to the polymer-based gel dosimeters since these polymer gel dosimeters have undesirable characteristics (toxicity, require preparation in oxygen free conditions etc) which have impeded their

wide acceptance as a clinical dose verification tool. Thus, the ability and possibility of the Look-Locker MR imaging sequence as a probing tool for Fricke gel dosimeters was investigated in this work. A brief summary of this investigation is given below in section 8.1.1.

Due to the toxicity faced by most polymer gel dosimeters, research groups have investigated gels with reduced toxicity. Two of these potential gel dosimeters used were investigated in this work and a summary of the results is presented below in section 8.1.4. The gels were irradiated with a desired dose distribution pattern were probed using MRI and optical CT. The ability to probe or read them with optical CT provides an attractive alternative to the more expensive MR imaging method due to its low cost and ready availability.

While developing these gels, other processes involved in the gel dosimetry process need particular attention as well, as these could act as a further hindrance to its wide clinical application or acceptance. One of the defining parameters or quality factor for the performance of a gel dosimeter is referred to as the *dose resolution*. This is defined as the minimal separation between two absorbed doses such that they may be distinguished with a given level of confidence. This parameter includes not only the sensitivity (or dose response) of the gel dosimeter but also includes the performance of the imaging tool be it x-ray, optical CT or MRI. This means factors which could limit or influence the accuracy and/or precision of this tool must not be ignored and correction strategies must be adopted using either existing correction methods or developing new and more convenient techniques. In this thesis work, two potential problems which might affect the performance of the MR imaging schemes were identified: non-linear gradient

field and B_1 field inhomogeneity. Maps of these inhomogeneities were made and correction schemes applied. A summary of the mapping and correction scheme is provided in sections 8.1.2 and 8.1.3.

8.1.1 3-D Look-Locker Imaging Method

A previously proposed 3-D Look-Locker imaging method for T_1 estimation has been modified. This modified imaging sequence was able to accommodate larger tip angle (as large as 20°) and was demonstrated to give proper T_1 estimates compared to IR. The larger tip angles improved the SNR and hence the accuracy and precision when compared to the conventional 3-D Look-Locker (which could only accommodate tip angles upto 5°). To use larger tip angles, an intermediate recovery time was introduced between the acquisition of each segment (of k-space) of a given inversion time image and that of the next inversion time image. This permitted more recovery of the magnetization towards its recovery path which would be driven too fast to its steady state without this recovery time. A fast and early steady state attainment brings about poor and unreliable estimates of the estimated T_1 parameter. This method provided estimation of T_1 within a 3% accuracy with only a marginal increase ($\sim 15\%$) in the acquisition time compared to the conventional 3-D Look-Locker method.

In the second part of the 3-D Look-Locker study, four different methods of acquiring (or filling out) the k-space were investigated and an optimized method was suggested which provided the best accuracy in T_1 estimation and minimized spatial blurring and the loss of spatial resolution due to the point spread function effect resulting from the fact that more than one line of k-space is acquired per recovery curve. The

results suggest that interleaving the k-space coverage from either ends of the k-space towards the opposite ends provided the best results in terms of minimal spatial resolution loss and accuracy in T_1 . A loss in spatial resolution of about 30 % which gives spatial resolution of ~ 1.3 mm was observed. Lastly the possible resultant dose resolution of a PVA-Fricke hydrogel using the proposed 3-D Look-Locker imaging scheme was discussed.

8.1.2 B_1 Inhomogeneity Field Mapping and Correction

Mapping of the RF or B_1 field within the imaging volume of the magnet provided correction factors which were then used to correct the estimated R_2 ($=1/T_2$) values obtained from baseline multiple spin-echo images. The degree of spin magnetization nutation (equivalent to flip angle) is determined partly by the magnitude of the B_1 field, and the calibration of this flip angle is usually done for a single slice at the isocentre where it is assumed this calibration holds true for the other (non-isocentric) slices. Unfortunately, this is not always the case leading to non-uniformity in the flip angle along the axial (or z-axis) direction

The axial B_1 inhomogeneity mapping was done using the method of *Barker et al* [124]. This method employed a spin-echo sequence to acquire 2mm slice profiles along the longitudinal (or z-axis) of the magnet. The spin-echo sequence was modified from a multi-slice multiple spin (MEMS) sequence that was used in Chapter 7 to acquire baseline images for the estimation of R_2 maps. This entailed acquiring the profiles for different power settings or transmitter attenuation for different transverse slices along the z-axis. The signal for the different power settings was fitted to calculate B_1 field scaling

factors along the z-direction. A spatial dependence of the transmitted B_1 field in the z-direction was observed, requiring different calibration factors for the non-isocentric slices in order to obtain the same flip angle nutation of spin magnetization. These calibration factors were then programmed into the imaging sequence to provide automatic modulation of the power settings for the tip angle depending on the slice in question.

Since the method *by Barker et al*[124] for transverse (i.e. x,y) B_1 field inhomogeneity is dependent on sample properties, a method according to *Akoka et al* [108], which has no such dependence was employed. This method allowed the acquisition of a flip angle map for every MEMS slice acquired. This then allowed a pixel-by-pixel correction of the R_2 images based on a pre-established R_2 -scale factor - β (flip angle) calibration curve. This method was relatively fast since it has little or no dependence on the T_1 of the material. This method of correction of B_1 inhomogeneity by generating a calibration curve for the MEMS sequence was compared to the PHAPS method which eliminates these B_1 effects in the acquired slice. The former provided a better performance in terms of SNR and precision and was therefore adopted in our subsequence measurements of R_2 maps.

8.1.3 Non Linear Gradient Field Mapping and Correction

The correction of the effects of non-linear gradient fields which manifest themselves as geometrical distortions in MR images involved a 2-step process: The mapping distortions measured with a simple grid phantom, and the correction of these distortions. This phantom consisted of smaller cuboid gel-filled phantoms of known dimensions which enclosed the spatial region in which the gel phantoms were to be

imaged in the MR imaging system. The gels in these phantoms had similar gelatin composition as polymer gel dosimeters. This was done to eliminate any possible distortion dependence from any material dependent field inhomogeneities. The maps generated from this phantom enabled a fit to the data to continuous functions which were then used to correct any image distortions due to the static field inhomogeneity and non-linear gradient fields. Very little or no change was observed on the estimated R_2 maps as a result of these non-linear magnetic field gradients.

8.1.4 Dose Verification using Polymer gel dosimeters with reduced toxicity

In Chapter 7, the results of preliminary investigations of two prospective polymer gel dosimeters for radiotherapy treatment planning with reduced toxicity are reported. These gel dosimeters were put in cylindrical phantoms and irradiated using a treatment plan delivered by a cobalt-60 tomotherapy machine. Each of these two polymer gel dosimeter types was irradiated to a maximum dose of 200 cGy and 500 cGy in the distribution pattern in two different phantoms. These phantoms were then imaged by both optical CT and MR imaging. The MR baseline images were acquired using a multiple spin-echo sequence which were then converted to a dose map via the fitted R_2 map.

Dose verification of the treatment plan distribution was done via γ -index maps, which is a clinical quality factor for the verification of planned dose distributions based on preset acceptance criteria for the dose differences and distance-to-agreement between two dose maps (measured and calculated). These two gel dosimeters produced results which largely fulfilled the set acceptance criteria of a 3% dose difference and a distance-to-agreement of 3 mm. This was especially the case for the comparison between the

treatment plan and MR measured dose distributions. A comparison between the dose distribution made from the optical CT derived images and MR images was also made via these γ -maps. In general, the optical CT-MR comparison produced satisfactory results fulfilling the set acceptance criteria, though to a lesser extent compared to the results between the treatment plan distribution and the MR derived dose maps. Therefore, on the basis of the γ -index maps obtained for these two polymer gel dosimeters, the MR method appeared superior to the optical CT method.

8.2 Future Work

The 3-D Look-Locker imaging method proposed in this thesis, allowing usage of larger tip angles with marginal increase in acquisition time, can be used as an imaging tool for T_1 -based Fricke gel dosimetry. The next investigative step towards its possible eventual use as a clinical tool would be to image a Fricke-gel phantom irradiated with a simplistic treatment plan dose distribution. From the calculated R_1 ($=1/T_1$) maps, dose distribution maps can be computed and used to compare with or verify the treatment plan dose distribution. This would have to be done in conjunction with another dosimetry method or tool such as film, TLD, ion chambers amongst others. If this produces results that satisfactorily meet the set criteria and the effect of diffusion is minimized to a negligible level, it can then be used to verify a more complex dose distribution treatment planned irradiation.

As for the two polymer gel dosimeters used for dose distribution verification in this thesis, further work will need to be done to investigate their viability as clinical dose verification tools. One factor that needs to be investigated is the problem of edge

enhancement prevalent in most polymer gel dosimeters. Within the time scale of three days between irradiation and MR imaging, no such effect was noticed. This normally involves the diffusion of the smaller unpolymerized monomers from a region of high monomer concentration (having received little or no irradiation) to a low monomer region (having been irradiated and most of the monomers converted to polymers) where these diffusing monomers polymerize with the increasing polymer chain. This additional polymerization brought about by these diffusing polymers enhances the dose information in these areas thereby giving erroneous dose values. The investigation of this problem is necessary to give a time scale between irradiation and imaging of the gel phantom so as to obtain optimal results and reduce or eliminate any edge enhancement effect. These effects if not eliminated or reduced would influence the comparisons between MRI-derived dose maps and the treatment plan distribution or any other dose map derived from other methods.

As for the comparison between the optical CT and the MRI measured dose distributions shown in Chapter 7, further work needs to be done to improve on the agreement or correlation. This might range from factors such as the correction of possible geometrical distortions to simply obtaining a better alignment between images obtained from both methods. This study was a first step forward to using these gels in the clinic for dose verification. Given that a cylindrical phantom was used for this study, the next logical step would be to mould phantoms, fill them with these gel dosimeters and use them along with the commonly used clinical methods to verify the treatment plan dose distributions for a given cancer tumour in a patient. Good and consistent agreement between these other methods and the treatment plan calculated distributions for a number

of trials would then be required before being used (if possible solely) as a dose verification tool in a clinical set up.

Another area worth investigating is the effects of inhomogeneities (e.g. bone/air) in these gel dosimeters. Since a lot of clinical dose distribution treatment planning requires accounting for the effects of these inhomogeneities in the radiation pathways, it would be of valuable interest to study these effects on these gel dosimeters. As earlier mentioned, this would eliminate the use of optical CT and leave mostly a modality such as MRI for dose verification for such irradiations with inhomogeneities insets such as bone.

In this thesis, the MR-derived dose maps were compared to optical CT as an alternative dose measuring tool for dose verification. Comparisons of MRI or optical CT dose maps with another well established and trusted clinical dose measuring method such as film dosimetry with dose measurements done at certain predefined positions will be another reasonable step to take towards validating these gel dosimeters.

References

- [1] C.S. Chui, S. Spirou and T. LoSasso, “Dose calculation for photon beams with intensity modulation generated by dynamic jaw of multileaf collimators”, *Med. Phys.* **21**, 1237-1224 (1994).
- [2] ICRU Report #50, Prescribing, recording and reporting photon beam therapy. *International commission of Radiation Units and Measurements* (1991).
- [3] L.J. Schreiner, “ Gel dosimetry: Motivation and Historical foundation”, In Proc. 1st International Workshop on Radiation Therapy Gel Dosimetry, 1-8 (1999).
- [4] M.E. Matterson, G. Barest, C.S. Chui et al, “Interinstitutional experience in verification of external photon dose calculations”, *J. Radiat. Oncol.Biol. Phys.* **21**, 37-58 (1991).
- [5] H. Fricke and E.J. Hart, *Chemical dosimetry in Radiation Dosimetry*, vol.2, F.H. Attix and W.C. Roesch (Eds), (Academic Press, New york) (1966).
- [6] C. Audet. NMR-Dose response studies of the gels used for 3-D radiation dosimetry by magnetic resonance imaging. *Ph.D Thesis*, (1995).
- [7] C. De Wagter, “The ideal dosimeter for intensity modulated radiation therapy (IMRT): What is required?,” *J. Phys.: Conf. Ser.* **3**, 4-8 (2004)
- [8] ICRU Report # 23, *Measurement of Absorbed dose in a phantom irradiated by a single beam of X or gamma rays*, International commission of Radiation Units and Measurements (1973).
- [9] S.T. Chui-Tsao, de la Zerda, J. Lin, J.H. Kim, “High sensitivity of Gaf chromic film dosimetry for ^{252}Cf seed”, *Med. Phys.* **21**, 651-657 (1994).

- [10] P. Keall and C. Baldock, "A theoretical study of the radiological properties and water equivalence of Fricke and polymer gels used for radiation dosimetry", *Australasian Physical & Engineering Sciences in Medicine* **22** (3), 85-91 (1999).
- [11] I. Rousselle, D. Gibon, B. Coche-Dequeant, B. Castelain, X. Marchandise, J. Rousseau, "Tissue-equivalence of dosimeter gels: Case of brain phantoms irradiated with photons", In *Proc. 1st International Workshop on Radiation Therapy Gel Dosimetry* 124-126 (1999).
- [12] M.F. Chan and K. Ayyangar, "Verification of water equivalence of FeMRI using Monte Carlo simulation", *Med. Phys.* **20**, 90 (1993).
- [13] T. Kron, P. Metcalfe, J. M. Pope, "Investigation of tissue equivalence of gels used for NMR dosimetry", *Phys. Med. Biol.* **38**, 139-150 (1993).
- [14] K.C. Chu, K. J. Jordan, J. J. Battista, J. Van Dyk, B. K. Rutt, "A Novel Fricke Dosimeter using PVA Cryogel", In *Proc. 1st International Workshop on Radiation Therapy Gel Dosimetry* 118-120 (1999).
- [15] K.C. Chu, K. J. Jordan, J.J. Batista, J. Van Dyk, B.K. Rutt, "Polyvinyl alcohol-Fricke hydrogel and cryogel: two new gel dosimetry systems with low Fe^{3+} diffusion", *Phys. Med. Biol.* **45**, 955-969 (2000).
- [16] Y. De Deene, K. Vergote, C. Claeys, C. De Wagter, "The fundamental radiation properties of normoxic polymer gel dosimeters: a comparison between a methacrylic acid based gel and acrylamide based gels", *Phys Med. Biol.* **51**, 653-673 (2006).
- [17] Y. Watanabe and R. Mooj, "Heterogeneity phantoms for visualizations of 3D dose distributions by MRI-based polymer gel dosimetry", *Med. Phys.* **31**(5) 975-984.

- [18] L. E. Olsson, S. Petersson, L. Ahlgren and S. Mattsson, "Ferrous sulphate gels for determination of absorbed dose using MRI technique: basic studies", *Phys. Med. Biol.* **34**, 43-52 (1989).
- [19] A. Appleby, E.A. Christian and A. Leghrouz, "Radiation chemical and magnetic resonance studies of aqueous agarose gels containing ferrous ions", *Rad. Res.* **52**, 241-244 (1987).
- [20] R.J. Schulz, A.F. deGuzman, D.B. Nguten, J.C. Gore, "Dose response curves for Fricke-infused agarose gels as obtained by nuclear magnetic resonance", *Phys. Med. Biol.* **35**, 1611-1622 (1990).
- [21] Y. De Deene, "Essential characteristics of polymer gel dosimeters. Third International Conference on Radiotherapy Gel Dosimetry," *J.Phys: Conf. Ser.* **3**, 34-57 (2004).
- [22] M.J. Maryanski, G.S. Ibbott, P. Eastman, R.J. Schulz, J.C. Gore, "Radiation therapy dosimetry using magnetic resonance imaging of polymer gels", *Med. Phys.* **23**(5), 699-705 (1996).
- [23] M.J. Maryanski, "Radiation-Sensitive Polymer gels: properties and manufacturing," In Proc. 1st International Workshop on radiation Therapy Gel Dosimetry. 160-162 (1999).
- [24] A.R. Farajollahi, D.E Bonnett, R.J Aukett, A.J Radcliffe, "The advantages and limitations of polymer gel dosimetry in brachytherapy", *J. Int. Fed. Med. Biol. Eng.* **35** 1012 (1997).

- [25] P. Kipouros, E. Pappas, P. Baras, D. Hatzipanayoti, P. Karaiskos, L. Sakelliou, P. Sandilos, I. Seimenis, “Wide dynamic dose range of VIPAR polymer gel dosimetry”, *Phys. Med. Biol.* **46**, 2143-2159 (2001).
- [26] J.C. Gore, Y.S. Kang and R.J Schulz, “Measurement of radiation dose distributions by nuclear magnetic resonance (NMR) imaging”, *Phys. Med. Biol.* **29**, 1189-1197 (1984).
- [27] I. Solomon, “Relaxation processes in a system of two spins”, *Phys. Rev.* **99**, 559-65 (1955).
- [28] A. Abragam, *Principles of Nuclear Magnetism* (Oxford: Clarendon) (1961).
- [29] A. Appleby, E. A. Christian and A. Leghrouz, “Imaging of spatial dose distribution in agarose using magnetic resonance”, *Med. Phys.* **14**, 382-384 (1987a).
- [30] L.E. Olsson, A. Fransson, and S. Mattsson, “MR imaging of absorbed dose distributions for radiotherapy using ferrous sulphate gels”, *Phys. Med. Biol.* **35**, 4623-4632 (1990).
- [31] R.J. Schulz, A. F. deGuzman, D. B. Nguyen and J. C. Gore, “Dose response curves for Fricke-infused gels as obtained by nuclear magnetic resonance”, *Phys. Med. Biol.* **35**, 1611-1622 (1990).
- [32] C. Audet and L.J. Schreiner, “Multiple-site fast exchange model for spin-lattice relaxation in the Fricke-Gelatin dosimeter”, *Med. Phys.* **24**, 201-209 (1997).
- [33] T. Hiraoka, N. Fukuda, H. Ikehira, K. Hoshinao, k. Nakazawa, Y. Tatena, K. Kawashima, “Digital imaging of dose distributions by magnetic resonance”, *Nippon Acta Radiologica.* **46**, 503-505 (1986).

- [34] T. Hiraoka, K. Hoshino, K. Kawashima, H. Kato, Y. Tateno, "A new gel using super absorbent polymer for mapping the spatial dose distribution of electron beams by MR imager", *Med. Dos.* **18**, 73-79 (1993).
- [35] M.J. Maryanski, R. J. Schulz, G. S. Ibbott et al, "Magnetic resonance imaging of radiation dose distributions using Polymer-gel dosimeter", *Phys. Med. Biol.* **39**, 1437-1455 (1994).
- [36] M.J. Maryanski, J.C. Gore, R.P. Kennan and R. J. Schulz, "NMR relaxation enhancement in gels polymerized and cross-linked by ionizing radiations: a new approach to 3-D dosimetry by MRI", *Magn. Reson. Imaging* **11**, 253-258 (1993).
- [37] M.J. Maryanski, R.J. Schulz, G.S. Ibbott, J.C. Gatenby, J. Xie, D. Horton, J.C. Gore, "Magnetic resonance imaging of radiation dose distributions using a polymer gel dosimeter", *Phys. Med. Biol.* **39**, 1437-1455 (1994).
- [38] M.J. Maryanski, Y.Z. Zastavker, and J.C. Gore, "Radiation dose distributions in three dimensions from tomographic optical density scanning of polymer gels II: Optical properties of the BANG polymer gel", *Phys. Med. Biol.* **41**, 2705-2717 (1996).
- [39] M.J. Maryanski, J.C. Gore, R.J. Schulz, M. Ranade, "Three dimensional dose distributions from optical scanning of polymer gels", *Med. Phys.* **23**(6), 1069 (1996).
- [40] M.J. Maryanski and M.J. Barry, "New supersensitive polymer dosimeter," *Med. Phys.* **25**(7), A178 (1998).

- [41] J.C. Gore, M. Ranade, M.J. Maryanski, R.J. Schulz, "Radiation dose distributions in three dimensions from tomographic optical density scanning of polymer gels: I. Development of an optical scanner", *Phys. Med. Biol.* **41**, 2695-2704 (1996).
- [42] M. Lepage, P.M. Jayasakera, S.A.J. Back, C. Baldock, "Dose resolution optimization of polymer gel dosimeter using different monomers", *Phys. Med. Biol.* **46**, 2665-2680 (2001).
- [43] H. Gustavsson, S.A.J. Back, M. Lepage, L. Rintoul, C. Baldock, "Development and optimization of a 2-hydroxyethylacrylate MRI polymer gel dosimeter", *Phys. Med. Biol.* **49**, 227-241(2004).
- [44] A.J. Venning, B. Hill, S. Brindha, B.J. Healy, C. Baldock, "Investigation of the PAGAT polymer gel dosimeter using magnetic resonance imaging", *Phys. Med. Biol.* **50** 3875-3888 (2005).
- [45] P.M. Fong, D.C. Keil, M.D. Does and J.C. Gore, "Polymer gels for magnetic resonance imaging of radiation dose distributions at normal room atmosphere", *Phys Med. Biol.* **46**, 3105-3113 (2001)
- [46] Y. De Deene, C. Hurley, A. Venning, K. Vergote, M. Mather, B. Healy, C. Baldock, "A basic study of some normoxic gel dosimeters", *Phys. Med. Biol.* **47**, 3441-3463 (2002).
- [47] P. Baras, I. Seimenis, P. Sandilos, L. Vlahos, T. Bieganski, E. Georgiou, E. Pantelis, P. Papagiannis, L. Sakelliou, "An evaluation of the TSE MR sequence for time efficient data acquisition in polymer gel dosimetry of applications involving high doses and steep dose gradients", *Med Phys* **32**(11), 3339-3345 (2005).

- [48] S. Mori, M. Endo, S. Furukawa, M. Sunaoka, H. Nonaka, T. Ishii and H. Ikehira, “Development of high-radiation sensitive polymer gel for magnetic resonance imaging in three-dimensional dosimetry”, *Magn. Res. Imaging.* **23**, 691-694 (2005).
- [49] P. Haraldsson, A. Karlsson, E. Wieslander, H. Gustavsson, S.A.J. Back, “Dose response evaluation of a low-density polymer gel dosimeter using MRI”, *Phys. Med. Biol.* **51**, 919-928 (2006).
- [50] M. Lepage, P.M. Jayasakera, S.A.J. Back, C. Baldock. “Dose response optimization of polymer gel dosimeters using different monomers”, *Phys. Med. Biol.* **46**, 2665-2680 (2001).
- [51] C. Baldock, M. Lepage, S.A.J. Back, P.M. Murry, P.M. Jayasekera, D. Porter and T. Kron, “Dose resolution in radiotherapy polymer gel dosimetry: effect of echo spacing in MRI pulse sequence”, *Phys. Med. Biol.* **46**, 449-460 (2001).
- [52] ICRU 1987 ICRU report No 42: Use of computers in external beam of radiotherapy procedures of with high energy photons and electrons (Bethesda, MD:ICRU)
- [53] Y. De Deene, C. De Wagter, W. De Neve, E. Achten, “Artefacts in multi-echo T2 imaging for high-precision gel dosimetry: I. Analysis and compensation of eddy currents”, *Phys. Med. Biol.* **45**, 1807-1823 (2000)
- [54] Y. De Deene, C. De Wagter, W. De Neve, E. Achten, “Artefacts in multi-echo T2 imaging for high-precision gel dosimetry: II. Analysis of B1-field inhomogeneity”, *Phys Med Biol.* **45** 1825-1839 (2000).

- [55] C. Hurley, Y. De Deene, R. Meder, J.M. Pope and C. Baldock, "The effect of water molecular self-diffusion on quantitatively high-resolution MRI polymer gel dosimetry", *Phys. Med. Biol.* **48**, 3043-3058 (2003).
- [56] Y. De Deene, C. Baldock, "Optimization of multiple spin-echo sequences for 3D polymer gel dosimetry", *Phys. Med. Biol.* **47**, 3117-3141 (2002).
- [57] V. Spevacek, P. Novotny, J. Vymazal, T. Cechak, "Temperature dependence of polymer-gel dosimeter nuclear magnetic resonance response", *Med. Phys.* **28**(11), 2370-2378 (2001).
- [58] M.J. Maryanski, C. Audet, J.C. Gore, "Effects of cross-linking and temperature on the dose response of a BANG polymer gel dosimeter", *Phys. Med. Biol.* **42**, 303-311 (1997).
- [59] A. Bankamp, L.R. Schad, "Comparison of TSE, TGSE, and CPMG measurement techniques for MR polymer gel dosimetry", *Magn. Reson. Imaging* **21**, 929-939 (2003).
- [60] Y. Watanabe, "Variable transformation of calibration equations for radiation dosimetry", *Phys. Med Biol.* **50**, 1221-1234 (2005).
- [61] M. Hilts, C. Duzenli, "Image filtering for improved dose resolution in CT polymer gel dosimetry", *Med. Phys.* **31** (1) 39-49 (2004).
- [62] M. Mcjurry, P.D. Tapper, V.P. Cosgrove, P.S. Murphy, S. Griffin, M.O. Leach et al, "Experimental 3D dosimetry around a high dose-rate clinical ¹⁹²Ir source using polyacrylamide gel (PAG) dosimeter", *Phys. Med. Biol.* **44**, 2431-2444 (1999).
- [63] C. Audet, C. Duzenli, W. Kwa, V. Tsang, A. Mackay, "An example of MRI polymer dosimetry applied to 3D conformal therapy", *Med Phys.* **23**, 803 (1996).

- [64] Y. Deene, N. Reynaert, C. De Wagter, "On the accuracy of monomer/polymer gel dosimetry in the proximity of a high dose-rate ^{192}Ir source", *Phys. Med. Biol.* **46** 2801-2825 (2001).
- [65] E. Pantelis, G. Lympelopoulou, P. Papagiannis, L. Sakelliou, E. Stiliaris, P. Sandilos, I. Seimenis, M. Kozicki, J.M. Rosiak, "Polymer gel dosimetry close to an ^{125}Ir interstitial brachytherapy source", *Phys. Med. Biol.* **50**, 4371-4384 (2005).
- [66] K. Vergote, Y. De Deene, W. Duthoy, W. De Gersem, W. De Neve, E. Achten, C. De Wagter, "Validation and application of polymer gel dosimetry for the dose verification of an intensity-modulated arc therapy (IMAT) treatment," *Phys. Med. Biol.* **49**, 287-305 (2004).
- [67] Y. De Deene, C. De Wagter, B. Van Duyse, S. Derycke, W. De Neve and E. Achten, "Three dimensional dosimetry using polymer gel and magnetic resonance imaging applied to the verification of conformal radiation therapy in head-and-neck cancer", *Radiother Oncol* **48**, 283-291 (1998).
- [68] J.V. Trapp, M. Partridge, V.N. Hansen, P. Childs, J. Bedford, A.P. Warrington, M.O. Leach and S. Webb, "The use of gel dosimetry for verification of electron and photon treatment plans in carcinoma of the scalp", *Phys. Med. Biol.* **49**, 1625-1635 (2004).
- [69] K. Vergote, Y. De Deene, F. Claus, W. De Gersem, B. Van Duyse, L. Paelinck, E. Achten, W. De Neve and C. De Wagter, "Application of monomer/polymer gel dosimetry to study the effects of tissue inhomogeneities on intensity-modulated radiation therapy (IMRT) dose distributions", *Radioth. Oncol.* **67**, 119-128 (2003).

- [70] P.A. Love, P.M. Evans, M.O. Leach and S. Webb, "Polymer gel measurement of dose homogeneity in the breast: comparing MLC intensity modulation with standard wedged delivery", *Phys. Med. Biol.* **48**, 1065-1074 (2003).
- [71] W. De Neve, W. De Gersem, S. Derycke, G. De Meerleer, M. Moerman, M.T. Bate et al, "Clinical delivery of intensity modulated conformal radiotherapy for relapsed or second-primary head and neck cancer using a multileaf collimator with dynamic control", *Radiat Oncol.* **50**, 301-314 (1999).
- [72] P. Karaiskos, I. Petrokokkinos, E. Tatsis, A. Angelopoulos, P. Baras, M. Kozicki, P. Papagiannis, J.M. Rosiak, L. Sakelliou, P. Sandilos and L. Vlachos, "Dose verification of single shot gamma knife applications using VIPAR polymer gel and MRI," *Phys. Med. Biol.* **50**, 1235-1250 (2005).
- [73] Y. Watanabe, T. Akimitsu, Y. Hirokawa, R.B. Mooij and G.M. Perera, "Evaluation of dose delivery accuracy of Gamma knife by polymer gel dosimetry", *Jr. Appl. Clin. Med. Phys.* **6**(3), 133-142 (2005).
- [74] Y. Watanabe, G.M. Perera and R.B. Mooij, "Image distortion in MRI-based polymer gel dosimetry of Gamma knife stereotactic radiosurgery systems", *Med. Phys.* **29**(5), 797-802 (2002).
- [75] V.P. Cosgrove, P.S. Murphy, M. McJurry, E.J. Adams, A.P. Warrington, M.O. Leach and S. Webb "The reproducibility of polyacrylamide gel dosimetry applied to stereotactic conformal radiotherapy", *Phys. Med. Biol.* **45**, 1195-1210 (2000).
- [76] G.S. Ibbott, F.J. Bova, M.J. Maryanski, Y. Zhang, S. Holcomb, R.G. Avison et al, "Use of BANG polymer gel dosimeter to evaluate repeat fixation stereotactic radiation therapy", *Med. Phys.* **23**, 1070 (1996).

- [77] G.S. Ibbott, M.J. Maryanski, P. Eastman, S.D. Holcomb, Y. Zhang, R.G. Avison et al, "Three dimensional visualization and measurement of conformal dose distributions using magnetic resonance imaging of BANG gel dosimeters", *Int. J Radiat Oncol. Phys.* **38**, 1097-1103 (1997).
- [78] S.A. Back, Implementation of MRI gel dosimetry in radiation therapy. PhD Thesis, Department of Radiation Physics, Malmo Lund University, Sweden,(1998).
- [79] J. Heufelder, S. Stiefel, M. Pfaender, L. Ludermann, G. Grebe, J. Heese, "Use of BANG polymer gel for dose measurements in a 69 MeV proton beam", *Med. Phys.* **30**(6), 1235-1240 (2003).
- [80] Y. De Deene, R. Van de Walle, E. Achten and C. De Wagter, "Mathematical analysis and experimental investigation of noise in quantitative magnetic resonance imaging applied in polymer gel dosimetry", *Signal Processing* **70**, 85-101 (1998).
- [81] M. Bengtsson, T. Furre, J. Rodal, A. Skretting and D.R. Olsen, "Measurement of dynamic wedge angles and beam profiles by means of MRI ferrous sulphate gel dosimetry", *Phys. Med. Biol.* **41**, 269-271 (1996).
- [82] S.A. Johansson, P. Magnusson, A. Fransson, L.E. Olsson, J.O. Christoffersson, A. Montelius, S. Mattsson, "Dosimeter Gel and MR imaging for Verification of Calculated Dose Distribution in Clinical Radiation Therapy", *Acta Oncol.* **36**(3), 283-290 (1997)
- [83] B.H. Knutsen, A. Skretting, T.P. Hellebust, D.R. Olsen,"Determination of 3D distribution from intracavitary brachytherapy of cervical cancer by MRI of irradiated ferrous sulphate gel", *Radiol. Oncol.* **43**, 219-227 (1997).

- [84] J. Rousseau, D. Gibon, T. Sarrazin, N. Doukhan, X. Marchandise, "Magnetic Resonance Imaging of agarose gel phantom for assessment of 3D dose distribution in linac radiosurgery", *Br. J. Radiol.* **67**, 646-648 (1994).
- [85] K.B. McAuley, "The chemistry and physics of polyacrylamide gel dosimeters: why they do and don't work", *J. Phys.: Conf. Ser.* **3**, 29-33(2004).
- [86] A.M. Fuxman, K.B. McAuley and L.J. Schreiner, "Modeling of free-radical cross-linking co-polymerization of acrylamide and *N,N'*-methylenebis(acrylamide) for radiation dosimetry", *Macromol. Theory Simul.* **12**, 647-662 (2003)
- [87] L.J. Schreiner, M. Rogers, R. Senden, K. McAuley and J. Miller, "Conformal dose verification using cone beam optical computed tomography and polymer gel dosimeters: A feasibility study," 51st Annual Meeting of COMP and CCPM symposium. Hamilton, ON, Canada (2005).
- [88] M. McJurry, M. Oldham, V.P. Cosgrove, P.S. Murphy, S. Doran, M.O. Leach and S. Webb, "Radiation dosimetry using polymer gels: methods and applications", *Br. J. Radiol.* **73** 919-929 (2000)
- [89] T.C. Farrar and E.D. Becker, *Pulse and Fourier Transform NMR*. Academic Press, New York and London (1971).
- [90] N. Bloembergen, E. Purcell, R. V. Pound "Relaxation effects in nuclear magnetic resonance", *Phys. Rev.* **73**, 679-712 (1948).
- [91] D.G. Nishimura, "Principles of Magnetic Resonance Imaging" (Stanford University Press, 1996)
- [92] F. Bloch, "Nuclear induction," *Phys. Rev.* **70**, 460-474 (1946).

- [93] D.I. Hoult and R.E. Richards, "The signal-to-noise ratio of the nuclear magnetic resonance experiment", *J. Magn. Reson.* **24**, 71-85 (1976).
- [94] J. R. Zimmerman and W. E. Brittin, "Nuclear magnetic resonance studies in multiple phase systems: lifetime of water molecule in an adsorbing phase on silica gel", *Phys Rev.* **61**, 1328-1333 (1957).
- [95] A. Abragam and R.V. Pound, "Influence of electric and magnetic fields on angular correlations", *Phys. Rev.* **92**, 943-962 (1953).
- [96] F. H. Attix, *Introduction to radiological physics and radiation dosimetry*. John Wiley & Sons. New York, NY (1986).
- [97] Y. De Deene, "Essential characteristics of polymer gel dosimeters. Third International Conference on Radiotherapy Gel Dosimetry," *J. Phy.: Conf. Ser.* **3**, 34-57(2004).
- [98] M. Lepage, A.K. Whittaker, L. Rintoul, S.A. Back, C. Baldock, "Modelling of Post-irradiation events in polymer gel dosimeters", *Phys. Med. Biol.* **46**, 2827-2839(2001).
- [99] C. Audet, "The NMR relaxometry of radiotherapy gel dosimeters," *Proceedings of the 1st International Workshop on Radiation Therapy Gel Dosimetry*. Lexington, Kentucky (1999).
- [100] D.C. Look, D.R. Locker, "Time saving in measurement of NMR and EPR relaxation times", *Rev. Sci. Instrum.* **41**, 250-251(1970)
- [101] G. Brix, L.R.Schad, M. Deimling, W.J. Lorentz, "Fast and precise T_1 imaging using a TOMROP sequence", *Magn. Reson. Imag* **8**, 351-356(1990).

- [102] A.P. Crawley, R.M. Henkelman, "A comparison of one shot and recovery methods in T_1 imaging", *Magn. Reson. Med.* **7**, 23-34(1988).
- [103] I. Kay and R.M. Henkelman, "Practical Implementation and Optimization of one-shot T_1 imaging", *Magn. Reson. Med.* **22**, 414-424(1991).
- [104] E. Henderson, G. Mckinnon, T.Y. Lee and B.K. Rutt, "A fast 3-D Look-Locker method for volumetric T_1 mapping", *Magn. Reson. Imag.* **17**, 1163-1171(1999).
- [105] S.C.L. Deoni, B.K. Rutt and T.M. Peters, "Rapid combined T_1 and T_2 mapping using gradient acquisition in the steady state", *Magn. Reson. Med* **49**, 515-526(2003).
- [106] K. Nkongchu and G. Santyr, "An improved 3D Look-Locker imaging method for T_1 parameter estimation", *Magn. Reson. Imaging* **7**, 801-807(2005).
- [107] C.J. Hardy, W.A. Edelstein and D.J. Vatis, "Efficient adiabatic fast passage for NMR population inversion in the presence of radiofrequency inhomogeneity and frequency offsets", *J. Magn. Reson.* **66**, 470-482(1986).
- [108] S. Akoka, F. Franconi, F. Seguin and A. Le Pape, "Radiofrequency map of an NMR coil by imaging", *Magn. Reson. Imaging* **11**, 437-441(1993).
- [109] M. Karlsson and B. Nordell, "Phantom and in vivo study of the Look-Locker method for T_1 mapping", *Magn. Reson. Imaging.* **17**, 1481-1488(1999).
- [110] A.J. Freeman, P.A. Gowland and P. Mansfield, "Optimization of the ultrafast Look-Locker echo-planar imaging T_1 mapping sequence", *Magn. Reson. Imaging* **16**, 762-772(1998).
- [111] R.T. Constable and J. Gore, "The loss of small objects in variable TE imaging: Implications for FSE, RARE, and EPI", *Magn. Reson. Med.* **28** 9-24(1992).

- [112] C.K. Jones, "Quantitative Multi-Component T_2 Analysis using Fast Spin-Echo MRI," Thesis (M.Sc)-University of British Columbia, Vancouver-Canada (1997)
- [113] P.T. Callaghan, "Principles of NMR microscopy" (Oxford University Press, Oxford, 1991)" 189-206(1991).
- [114] K. Nkongchu, "PVA-Fricke Hydrogels for radiotherapy dosimetry using magnetic resonance imaging", Thesis (M.Sc.)-Carleton University, Ottawa-Canada. (2001).
- [115] Brahme A, "Dosimetric precision requirements in radiation therapy", *Acta Radiol. Oncol.* **23**, 379-391(1984).
- [116] G. Gambarini, S. Arrigoni, M.C. Cantone, N . Molho, L . Fachielli and A.E. Sichirollo, "Dose-response curve slope reproducibility of ferrous sulphate doped gels analysed by NMR imaging", *Phys. Med. Biol.* **39**, 703-717(1994).
- [117] F. Chan., J. Pauly and A. Macovski, "Effects of RF amplifier distortion on selective excitation and their correction by prewarping," *Magn. Reson. Med.* **23**, 224-238(1992).
- [118] J. Slotboom., J.N.N. Creyghton., D. Korbee, A.F. Mehlkopf and W.M. Bovee, "Spatially selective RF pulses and the effects of digitization on their performance", *Magn. Reson. Med.* **30**, 732-740(1993).
- [119] C.M. Collins, S. Li, Q.X. Yang, M.B. Smith, "A method for accurate calculation of B1 fields in three dimensions: Effects of shield geometry on field strength and homogeneity in the birdcage coil", *J. Magn. Reson.* **25**, 233-241(1997).
- [120] S. Li, Q.S. Yang and M.B. Smith, "RF coil optimization: Evaluation of B1 field homogeneity using field histograms and finite element calculations", *Magn. Reson. Imaging.* **12**, 1079-1087(1994).

- [121] G.C. Scott, M.L. Joy, R.L. Armstrong and R.M. Henkelmann, "RF current density imaging in homogeneous media" *Magn. Reson. Med.* **28**, 186-201(1992).
- [122] P.A. Bottomley and E.R. Andrew, "RF magnetic field penetration, phase shift and power dissipation in biological tissue: implications for NMR imaging", *Phys. Med. Biol.* **23**, 630-43(1978).
- [123] R. Graumann, A. Oppelt and R. Setter, "Multiple-spin-echo imaging with a 2D Fourier method", *Magn. Reson. Med.* **3**, 707-721(1986).
- [124] G.J. Barker, A. Simmons, S.R. Arridge and P.S. Tofts, "A simple method for investigating the effects of non-uniformity of radiofrequency transmission and radiofrequency reception in MRI", *Br. Jr. Radiol.* **71**, 59-67(1998).
- [125] M. Alecci, C.M. Collins, M.B. Smith and P. Jezzard, "Radio frequency magnetic field mapping of a 3 Tesla birdcage coil: Experimental and theoretical dependence on sample properties", *Magn. Reson. Med.* **46**, 379-385(2001).
- [126] S. Clare, M. Alleci and P. Jezzard, "Compensating for B1 Inhomogeneity using Active transmit power modulation", *Magn. Reson. Imaging* **19**, 1349-1352(2001).
- [127] H. Chang and J.M. Fitzpatrick, "A technique for accurate magnetic resonance imaging in the presence of field inhomogeneities", *IEEE Trans. Med. Imag.* **11**(3), 319-329 (1992).
- [128] A. Kawanaka and M. Takagi, "Estimation of static magnetic field and gradient fields from NMR image", *J. Phys. E: Sci. Instrum.* **19**, 871-875 (1986).
- [129] C.J. Bakker, M. Moerland, R. Bhagwandien and R. Beersma, "Analysis of machine-dependent and object-induced geometric distortion in 2DFT MR imaging", *Magn. Reson. Imaging.* **10**, 597-608 (1992).

- [130] M.A. Moerland, R. Beersma, R. Bhagwandien, H.K. Wijrdeman and C.J. Bakker, "Analysis and correction of geometric distortions in 1.5 T magnetic resonance images for use in radiotherapy treatment planning", *Phys. Med. Biol.* **40**, 1651-1664 (1995).
- [131] T.S. Sumanaweera, G.H. Glover, P.F. Hemler, P.A. Vandenelson, D. Martin, J.R. Adler and S. Napel, "MR geometric distortion correction for improved frame-based stereotactic target localization accuracy", *Magn. Reson. Med.* **34**, 106-113(1995).
- [132] S.J. Doran, L. Charles-Edwards, S.A. Reinsberg and M.O. Leach, "A complete distortion for MR images: I. Gradient warp correction", *Phys. Med. Biol.* **50**, 1343-1361(2005).
- [133] S. Langlois, M. Desvignes, J.M. Constans and M. Revenu, "MRI Geometric Distortion: A Simple Approach to Correcting the Effects of Non-Linear Gradient Fields", *J. Magn. Reson. Imag.* **9**, 821-831 (1999).
- [134] Y. De Deene, "Fundamentals of MRI measurements for gel dosimetry," *J. Phys.: Conf. Ser.* **3**, 87-114 (2004).
- [135] C. Hurley, Y. De Deene, R. Meder, J.M. Pope and C. Baldock, "The effect of water molecule self-diffusion on quantitative high resolution MRI polymer gel dosimetry", *Phys. Med. Biol.* **48**, 3043-3058(2003).
- [136] R.J. Senden, P. De Jean, K.B. McAuley and L.J. Schreiner, "Polymer gel dosimeters with reduced toxicity: a preliminary investigation of the NMR and optical dose response using different monomers", *Phys. Med. Biol.* **51**, 1-14 (2006).

- [137] G.J. Salomons Y.S. park, K.B. McAuley and L.J. Schreiner, "Temperature increases associated with polymerization of irradiated PAG dosimeters," *Phys. Med. Biol.* **47**, 1435-1448 (2002).
- [138] Y. De Deene, P. Hanselaer and C. De Wagter, "An investigation of the chemical stability of a monomer/polymer gel dosimeter", *Phys Med Biol.* **45**, 859-878 (2000).
- [139] D.A. Low, W.B. Harms, S. Mutic and J.A. Purdy, "A technique for the quantitative evaluation of dose distributions", *Med. Phys.* **25**(5), 656-661 (1998).
- [140] V. Spevacek, J. Novotny, P. Dvorak, J. Vymazal and T. Cechak, "Temperature dependence of polymer-gel dosimeter nuclear magnetic resonance response", *Med. Phys.* **28**(11), 2370-2378 (2001).
- [141] M. Oldham, "Optical-CT scanning of polymer gels," *J. Phys; Conf. Series* **3**, 122-135 (2004).
- [142] MSDS 2005 Material Safety Data Sheet acrylamide, version 1.10 updated 06/17/2005, Sigma-Aldrich Canada, Ltd (<http://sigma-aldrich.ca/>)
- [143] M. Lepage, A.K. Whittaker, L Rintoul, S.A.J. Back and C. Baldock, "Modelling of post-irradiation events in polymer gel dosimeters", *Phys. Med. Biol.* **46**, 2827-2839 (2001).

Appendix A

Table A.1: The estimated coefficients of the three variable polynomial from the distortion data acquired using the gel-filled grid phantom.

| $\Delta x(x,y,z)$ coefficients | $\Delta y(x,y,z)$ coefficients | $\Delta z(x,y,z)$ coefficients | Coeff. Units | Polynomial terms |
|-----------------------------------|-----------------------------------|-----------------------------------|------------------|-------------------------------|
| 7.77e-2 | 9.41e-2 | 9.36e-2 | mm | constant |
| 1.38e-2 | -2.91e-3 | -6.20e-3 | mm ⁰ | x |
| 2.34e-4 | 6.10e-5 | -6.27e-4 | mm ⁻¹ | x ² |
| 1.98e-2 | 1.46e-2 | -3.36e-3 | mm ⁰ | y |
| -3.47e-5 | 2.93e-5 | 1.12e-4 | mm ⁻¹ | xy |
| -1.21e-4 | 2.66e-4 | -6.67e-4 | mm ⁻¹ | y ² |
| -3.76e-2 | 1.31e-2 | -2.95e-2 | mm ⁰ | z |
| 8.02e-4 | -8.90e-5 | -8.19e-4 | mm ⁻¹ | zx |
| 1.33e-3 | -1.56e-4 | 1.06e-3 | mm ⁻¹ | zy |
| -1.02e-3 | -1.96e-4 | -2.41e-3 | mm ⁻¹ | z ² |
| -3.89e-6 | 1.08e-6 | 1.56e-6 | mm ⁻² | x ³ |
| -7.35e-6 | -1.43e-5 | 1.32e-5 | mm ⁻² | yx ² |
| -1.19e-5 | 1.41e-6 | -5.15e-6 | mm ⁻² | xy ² |
| -4.36e-6 | -8.07e-6 | 9.48e-6 | mm ⁻² | y ³ |
| -2.73e-5 | -5.69e-7 | 4.60e-5 | mm ⁻² | zx ³ |
| 3.55e-6 | 2.64e-6 | -1.92e-7 | mm ⁻² | zxy |
| -8.32e-6 | -6.34e-7 | 2.03e-5 | mm ⁻² | zy ² |
| -8.36e-6 | 2.67e-7 | 1.45e-6 | mm ⁻² | xz ² |
| -4.48e-5 | 1.09e-5 | -2.66e-5 | mm ⁻² | yz ² |
| 1.84e-5 | -9.97e-6 | -1.29e-5 | mm ⁻² | z ³ |
| 4.51e-8 | 9.65e-8 | 6.25e-8 | mm ⁻³ | yx ³ |
| -2.66e-7 | -2.05e-8 | 5.86e-7 | mm ⁻³ | yx ³ |
| 2.71e-8 | -4.87e-9 | -8.76e-8 | mm ⁻³ | x ² y ² |
| 2.08e-7 | 1.97e-8 | -1.27e-7 | mm ⁻³ | zx ³ |
| -2.89e-7 | 4.81e-9 | -2.66e-7 | mm ⁻³ | zyx ² |
| -2.15e-7 | 1.06e-8 | 2.18e-8 | mm ⁻³ | zxy ² |
| -2.43e-7 | 6.67e-8 | -4.42e-7 | mm ⁻³ | zy ³ |
| 9.39e-7 | -2.20e-8 | 1.69e-6 | mm ⁻³ | z ² x ² |
| 3.45e-8 | -1.21e-7 | 4.04e-8 | mm ⁻³ | z ² xy |
| 1.26e-6 | -1.94e-7 | 1.47e-6 | mm ⁻³ | z ² y ² |
| -6.30e-7 | 1.85e-8 | 4.57e-7 | mm ⁻³ | z ³ x |
| -4.02e-7 | 6.06e-8 | -2.63e-7 | mm ⁻³ | z ³ y |
| -2.47e-7 | -6.81e-9 | 2.07e-7 | mm ⁻³ | x ⁴ |
| -1.73e-7 | -5.84e-8 | 2.23e-7 | mm ⁻³ | y ⁴ |
| 5.15e-7 | 2.25e-8 | 5.62e-7 | mm ⁻³ | z ⁴ |
| 35.8 | 31.1 | 6.52 | Residuals | |